Exploring the 3D structure of defects and electron-beam induced dynamics in graphene

Dissertation

der Mathematisch-Naturwissenschaftlichen Fakultät

der Eberhard Karls Universität Tübingen

zur Erlangung des Grades eines

Doktors der Naturwissenschaften

(Dr. rer. nat.)

vorgelegt von

Mag. Christoph Hofer

Wiener Neustadt/Österreich

Tübingen

2019

Abstract

When an electron's propagation direction in a material is restricted in one or multiple dimensions, the material's properties deviate heavily from its bulk counterpart. These properties were intensively studied theoretically decades before the experimental synthesis of these "low-dimensional" materials was realized. Carbon is one of the major elements in organic chemistry and can form a large variety of allotropes in different dimensions. Graphene, an atomically thin single layer of carbon, is the 2D component of the carbon allotropes and can be regarded as the building block for most of the other allotropes. It is the thinnest material in the world and the first 2D material to be successfully isolated. Stacking graphene layers results in graphite, which is the 3D crystalline carbon allotrope besides diamond. Rolling up a graphene sheet can form a carbon nanotube, which can have different phases and therefore can have different properties. The nanotubes are regarded as 1D materials and were described in 1991 by Sumio Iijima. Fullerenes, where 60 carbon atoms build the smallest soccer balls in the world, are regarded as a 0D material and were successfully synthesized already in 1985.

Graphene has been successfully isolated in 2003, recently after the development of aberration correctors in transmission electron microscopes which enabled resolving single atoms in very beam-sensitive materials. This coincidence made it possible to intensively study graphene as well as the dynamics of single atoms. This enormous effort is not only justified by its unique properties which are very interesting for industrial applications, but also for the possibility of a fundamental understanding low-dimensional physics experimentally at the atomic scale. Despite the huge attention paid to graphene, there is still limited information about its actual 3D structure, especially at defect sites. This knowledge gap is due to the limited information in 2D using aberration corrected transmission electron microscopy techniques, because their images are essentially projections of an object. This cumulative thesis focuses on filling this missing knowledge gap and delivers a relevant contribution for the understanding of the (3D) structural properties of defects in graphene.

The cumulative dissertation is based on 3 peer-reviewed first-author publications and one relevant peer-reviewed non-first-author publication, which present a new method of reconstructing atomically-thin structures using only 2 atomically resolved images. They reveal insights into the 3D structure of grain boundaries, heteroatom impurities and van-der-Waals heterostructures. Not just static properties, but also out-of-plane dynamics induced by the electron beam are studied. In addition, scanning transmission electron microscopy is used to unambiguously identify single oxygen and nitrogen atoms in defective graphene. The data set allows statistical assessment of all the bonding configurations and comparison of oxygen with nitrogen configurations. Remarkably, graphitic oxygen substitutions with three carbon neighbors are observed.

This cumulative thesis is clustered in 4 different chapters. Chapter 1 presents an introduction on the studied material and a motivation of this work. Chapter 2 summarizes the experimental

methods and introduces their principles and basic physics. Chapter 3 discusses the novel reconstruction method in detail. Chapter 4 briefly summarizes the papers and the author's contributions. Each summary follows the corresponding original publication.

Zusammenfassung

Wenn die Propagationsrichtung eines Elektrons in einem Material in einer oder mehreren Dimensionen beschränkt wird, verändern sich die Eigenschaften des Materials gravierend. Diese Eigenschaften wurden bereits Jahrzehnte vor der experimentellen Synthese dieser sogenannten "niedrig-dimensionalen" Materialien theoretisch untersucht. Kohlenstoff ist eines der bedeutendsten Elemente in der organischen Chemie und kann eine Vielzahl an Allotropen in verschiedenen Dimensionen bilden. Graphen, eine atomar dünne Schicht aus Kohlenstoffatome, ist ein zweidimensionales Kohlenstoff Allotrop und kann als Baustein der meisten anderen Allotropen angesehen werden. Es ist das dünnste Material der Welt und das erste 2D Material das erfolgreich isoliert wurde. Eine Stapelung von Graphen ergibt Graphit, welches neben Diamant ein 3D kristallines Kohlenstoff Allotrop ist. Aufgerolltes Graphen ergibt ein Kohlenstoff Nanoröhrchen, welche unterschiedliche strukturelle Phasen und daher auch unterschiedliche Eigenschaften besitzt. Nanoröhrchen gelten als 1D Materialien und wurden 1991 von Sumio Iijima beschrieben. Fullerene sind die kleinsten Fußballmoleküle der Welt, bestehend aus 60 Kohlenstoff Atomen und werden als 0D Materialien angesehen, welche bereits 1985 erfolgreich synthetisiert wurden.

Graphen wurde 2003 erfolgreich isoliert kurz nach der Realisierung von Aberrationskorrektoren für Transmissionselektronenmikroskope, welche das Auflösen einzelner Atome in sehr bestrahlungsempflinglichen Materialien ermöglichten. Das Zusammentreffen dieser Umstände machte es möglich, sowohl Graphen, als auch die Dynamiken individueller Atome intensiv zu studieren. Dieser enorme Aufwand ist nicht nur durch die einzigartigen Eigenschaften von Graphen gerechtfertigt, welche sich als höchstinteressant für industrielle Anwendungen herausstellen, sondern auch durch die Möglichkeit, ein fundamentales Verständnis für niedrigdimensionale Physik experimentell auf atomarer Skala zu entwickeln. Obwohl Graphen enorme Aufmerksamkeit gewidmet wird, gibt es nur ein sehr beschränktes Wissen über dessen eigentliche 3D Struktur, besonders an Defekten. Diese Wissenslücke resultiert daraus, dass atomar aufgelöste Bilder von aberrationskorrigierten Transmissionselektronenmikroskopen in 2D beschränkt sind, da sie nur Projektionen eines Objekts abbilden. Diese kumulative Doktorarbeit fokussiert sich auf die Schließung dieser Wissenslücke und liefert einen relevanten Beitrag für das Verständnis von (3D) Strukureigenschaften von Defekten in Graphen.

Die Dissertation basiert auf drei begutachteten Erstautor Publikationen und einer relevanten begutachteten Nebenautor Publikation, welche eine neuartige Methode präsentiert, atomar dünne Materialien durch Verwendung von nur zwei atomar-aufgelösten Bildern aus unterschiedlichen Blickrichtungen zu rekonstruieren. Damit enthüllt diese Arbeit Erkenntnisse über die 3D Struktur von Korngrenzen, Fremdatomen und van-der-Waals Heterostrukturen. Abgesehen von statischen Strukureigenschaften werden Dynamiken senkrecht zum Kristallgitter, die vom Elektronenstrahl induziert werden, studiert. Desweiteren wird Rastertransmissionselektronenmikroskopie verwendet um Sauerstoff- und Stickstoffatome in defektreichem Graphen eindeutig zu identifizieren.

Die Daten erlauben eine statistische Beschreibung der auftretenden Bindungskonfigurationen und einen Vergleich zwischen Stickstoff und Sauerstoff Bindungen. Als besonders interessante Beobachtung erweisen sich graphitische Sauerstoff Substitutionen, die sich mit drei Kohlenstoffnachbarn binden.

Diese kumulative Doktorarbeit ist in vier Kapitel eingeteilt. Kapitel 1 präsentiert eine Einleitung zu dem studierten Material und gibt einen Einblick in die Relevanz dieser Arbeit. Kapitel 2 fasst die experimentellen Methoden zusammen und liefert eine Einleitung in deren Prinzipien und der grundlegenden Physik. Kapitel 3 diskutiert die neuartige Rekonstruktionsmethode im Detail. Kapitel 4 fasst die Publikationen und die Beiträge des Autors kurz zusammen. Nach jeder Zusammenfassung folgt die zugehörige Originalpublikation.

Danksagung

Contents

List of publications

The presented cumulative thesis is based on the following publications, which are published to international peer-reviewed journals:

1. **Revealing the 3D structure of graphene defects**

   Christoph Hofer, Christian Kramberger, Mohammad R.A. Monazam, Clemens Mangler, Andreas Mittelberger, Giacomo Argentero, Jani Kotakoski and Jannik C. Meyer

   2D materials, 5, 045029 (2018)

   Author contributions: Specified in chapter 4.1.

2. **Direct visualization of the 3D structure of silicon impurities in graphene**

   Christoph Hofer, Viera Skakalova, Mohammad R. A. Monazam, Clemens Mangler, Jani Kotakoski, Toma Susi and Jannik C. Meyer

   Applied Physics Letters, 114, 053102 (2019)

   Author contributions: Specified in chapter 4.2.

3. **Direct imaging of light-element impurities in graphene reveals triple-coordinated oxygen**

   Christoph Hofer, Viera Skakalova, Tobias Görlich, Mukesh Tripathi, Andreas Mittelberger, Clemens Mangler, Mohammad R.A. Monazam, Toma Susi, Jani Kotakoski and Jannik C. Meyer

   Nature Communications, 10, 4570 (2019)

   Author contributions: Specified in chapter 4.3.

4. **Atomic-Scale Deformations at the Interface of a Mixed-Dimensional van der Waals Heterostructure**

   Kimmo Mustonen, Aqeel Hussain, **Christoph Hofer**, Mohammad R. A. Monazam, Rasim Mirzayev, Kenan Elibol, Patrik Laiho, Clemens Mangler, Hua Jiang, Toma Susi, Esko I. Kauppinen, Jani Kotakoski and Jannik C. Meyer

   ACS Nano, 12(8) 8512-8519 (2018)

Author contributions: The author of this thesis participated in the STEM experiments and applied the three-dimensional reconstruction. The other authors conducted the rest of the study.

Furthermore, the presented PhD research herein has contributed to the following publications:

5. **Engineering single-atom dynamics with electron irradiation**

   Cong Su, Mukesh Tripathi, Qing-Bo Yan, Zegao Wang, Zihan Zhang, **Christoph Hofer**, Haozhe Wang, Leonardo Basile, Gang Su, Mingdong Dong, Jannik C. Meyer, Jani Kotakoski, Jing Kong, Juan-Carlos Idrobo, Toma Susi and Ju Li

   Science Advances, 5, 5, (2019)

   Author contributions: The author of this thesis performed the STEM experiment of the silicon impurity in graphene. The other authors conducted the rest of the study.

6. **Analysis of Point Defects in Graphene Using Low Dose Scanning Transmission Electron Microscopy Imaging and Maximum Likelihood Reconstruction**

   Christian Kramberger, Andreas Mittelberger, **Christoph Hofer** and Jannik C. Meyer

   physica status solidi (b), 254(11), 1770257 (2017)

   Author contributions: The author of this thesis participated in the STEM experiment. The other authors conducted the rest of the study.

7. **Automated Image Acquisition for Low-Dose STEM at Atomic Resolution**

   Andreas Mittelberger, Christian Kramberger, **Christoph Hofer** and Jannik C. Meyer

   Microscopy and Microanalysis, 23(04), 1-9 (2017)

   Author contributions: The author of this thesis participated in the STEM experiment. The other authors conducted the rest of the study.

1

Introduction

1.1 Graphene

In science, trial and error is sometimes the only way to make experimental progresses. And sometimes, it does not even require extensive equipment to conduct these experiments. Andre Geim and Konstantin Novoselov, two physicists from the University of Manchester, were curious enough to spend a tiny part of their lab work for experiments which "probably won't pan out at all, but if they do, it would be really surprising" [1]. In 2003, they attempted to prepare the thinnest material in the world – namely graphene. And this achievement was definitely very surprising this time. Graphene is a one atomic-layer thin material and was already theoretically studied after the second world war [2, 3]. Although graphene was predicted to have very fascinating properties and therefore the potential to be integrated into many industrial applications, it was presumed not to exist due to thermodynamic instabilities [4, 5, 6]. Therefore, the majority of the scientific community regarded graphene as just a theoretical object. However, Geim and Novoselov iteratively peeled off layer-by-layer of graphite using a simple adhesive tape and managed to isolate graphene and proved that 2D materials – which are only one unit-cell thick – can indeed exist [7]. Since that discovery, graphene and other 2D materials have attracted a huge attention resulting in an enormous amount of publications and have ignited a revolution in science and technology. Therefore, it was not surprising that they were awarded the Nobel Prize in Physics in 2010 "for groundbreaking experiments regarding the two-dimensional material graphene" [8]. The stability of suspended graphene could be explained in 2007, when it was proven that graphene is not perfectly flat, but exhibits an intrinsic roughness [9].

The rise of graphene and the massive investment in its research is justified by its exciting electronic properties (e.g. high electron mobility and high conductivity [10, 11]), optical properties (e.g. high transparency [12]), mechanical properties (e.g. high elastic modulus [13]), chemical properties (e.g. chemical inertness and impermeability to gases) and other unusual quantum-mechanical properties [14]. These properties arise from the simple hexagonal arrangement of carbon atoms where three valence electrons form sp^2-hybridized orbitals, resulting in strong in-plane bonds with an inter-atomic distance of $d = 142\,\mathrm{pm}$ and one delocalized electron in the remaining orthogonal $2p$-orbital, which determines its electronic properties. Due to graphene's unique properties, years of development were specifically spent on graphene-based electronic devices (e.g. high-frequency field-effect transistors [15], batteries [16], highly-efficient solar

cells [17]). The various properties are the key for the countless numbers of potential applications beyond electronic devices. In the electron microscopy community, graphene is the ideal substrate for the observation of particles and molecules due to its very weak scattering cross-section. For example, a monolayer of hexadecachlorocopperphtalocyanine ($CuPcCl_{16}$) molecules could be imaged on graphene [18]. Furthermore, graphene can also be used as a protection layer by embedding the material of interest between two sheets of graphene. With this method, fullerenes could be stabilized and imaged [19].

The lattice constant of the hexagonal lattice of graphene is $a = 246\,\text{pm}$ (Fig. 1.1a). Repeating the two-atom unit cell forms the characteristic honeycomb lattice. When using four basis vectors, as commonly used in hexagonal systems, the primary six-fold lattice spacings are indexed by $10\bar{1}0$ (corresponding to the first reciprocal vector) and $11\bar{2}0$ (corresponding to the second reciprocal vector) and are shown in Fig. 1.1b. This concept is crucial for diffraction analysis where the positions of the Bragg diffraction peaks are given by the reciprocal vectors while the intensities are given by the structure factors. In the case of monolayer graphene, it turns out that the first two orders of the Bragg diffraction spots have theoretically the same intensity while the intensity ratio is significantly changed already for an AB stacked bilayer. As one example, the reciprocal vector $G_{10\bar{1}0} = b_1 - b_3$ is shown in Fig. 1.1c.

After the initial excitement of graphene (reaching over 10.000 publications per year), also other 2D materials – most importantly single unit cell thick transition metal dichalcogenides – and their stacking [20] became more relevant. These artificial materials might compensate for graphene's weaknesses such as the lack of an electronic band gap [21, 22].

It can be seen as a fortunate coincidence that in the era of graphene as well as the development of aberration-correction in (scanning) transmission electron microscopes (S/TEM) reached a practical milestone that makes it possible to reach atomic resolution at energies close to the damage threshold of these one-atomic layer thick materials (ca. $80\,\text{kV}$ for graphene). This enabled not only the study of structural properties, but also interesting electron-beam induced dynamics and controlled manipulation of the structure. For a detailed description of the principle of S/TEM, see chapter 2.1.

a

b

c
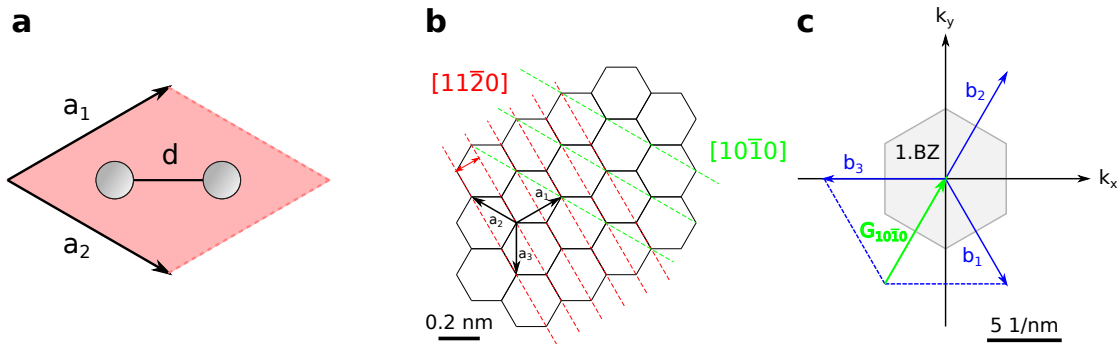
Figure 1.1: **Structural properties of graphene.** (a) The two-atomic hexagonal unit cell of graphene with a lattice constant of $|\vec{a}_1| = |\vec{a}_2| = 2.46\,\text{Å}$ and an interatomic distance of $d = 1.42\,\text{Å}$. (b) Graphene honeycomb lattice with two representative lattice spacing groups. (c) Reciprocal lattice of graphene with the first Brillouin zone. According to Ref. [23]

1.2 Defects and deformations in graphene

Although the intrinsic properties of graphene and other 2D materials open many possible applications, the properties are often only valid for a perfect crystal. Deviations from the perfect periodic atomic lattice can significantly modify their properties and a comprehensive understanding of the possible configurations, their stabilities, and their effects is thus of critical importance. The 2D nature of graphene enables strain relaxation – for example induced by defects – in the third dimension. Since the discovery of fullerenes [24], it has been known that non-hexagonal rings induce local curvatures in a graphene sheet. Therefore, it is also expected that embedded defects within the graphene lattice might induce significant out-of-plane deformations due to the "freedom" provided by the third dimension [25, 26, 27]. These distortions of the sheets have to be taken into account when characterizing their properties. Structural relaxation by energy minimization is a common computational method to retrieve the 3D structure as e.g. shown in paper 1 (section 4.1.) of this thesis, but it requires approximations, periodic boundary conditions and is usually limited to a relatively small number of atoms. Moreover, a broad variety of parameters often requires experimental confirmation of the computational output.

A very common group of defects in graphene are point defects, which can be created by bond rotations (e.g. a Stone-Wales transform), vacancies or substitutions. An enormous amount of effort has been taken to model their properties [28] and control their formation [29, 30]. Foreign atoms which replace the original element are often referred to as dopants or impurities and have been intensively studied due to the significant modification of the electronic structure. A lot of effort has been taken to tune the band structure by incorporating foreign atoms in the graphene lattice and systematically manipulate them within the structure [31, 32, 33]. A local distortion of the lattice can already be intuitively explained by the different atomic radii. The out-of-plane buckling of impurity atoms on the substitutional site has been experimentally confirmed by analyzing the fine structure in the electron energy loss spectrum (EELS) [34, 35, 36, 37].

An often unavoidable structural defect in graphene is a grain boundary (GB) which is formed in graphene during its synthesis by chemical vapor deposition (CVD) due to nucleation and

connection of individual graphene grains [38]. On the one hand, they are known to e.g. degrade the electronic properties due to the modification of the $2p$ orbital and scattering of the electron waves [39]. On the other hand, it has been reported that GBs can enhance the mechanical strength [40]. The out-of-plane characteristics in line defects such as GBs are still not clearly understood due to the challenges in modeling these structures. Furthermore, because the misorientation between the individual grains can exhibit an arbitrary angle, each grain boundary is individual and can have different sequences of non-hexagonal rings, so it can be straight or serpentine-like and can migrate within the lattice [41]. Calculations reveal – despite being limited to straight GBs – interesting buckling trends depending on the misorientation angle: while GBs with large misorientation angles ($30°$) tend to be flat, small angles (close to $0°$) tend to have sharper kinks [25, 26]. A part of my results (see section 4.1) confirms this trend experimentally. GBs with large misorientations can form a chain of non-hexagonal configurations which compensate for the strain induced by the lattice orientation mismatch while two grains with a small orientation mismatch are only rarely able to connect via non-hexagonal polygons, so they compensate the strain by buckling in the third dimension.

Defects in the structure not only result from the sample preparation procedure, but can be also induced by the interaction of the atoms with the electrons in a TEM. In semi-conductors and insulators, ionization damage (radiolysis) due to the excitation of an electron breaks the bond, leading to atomic ejections. In conductors (such as graphene), knock-on damage dominates. Here, the incident electron elastically scatters from the potential of an atomic nucleus, transferring a certain amount of energy. An ejection of the atom occurs if the transferred energy is larger than the atom's displacement threshold energy. This displacement mechanism is quantitatively well understood in the case of pristine graphene when atomic vibrations are taken into account [42, 43]. In the case of sp^2-hybridized carbon atoms, the threshold energy of atomic ejection is approx. 21 eV whereas the activation energy for bond rotations is in the range of 4–10 eV [29]. Because the maximum transferred energy is smaller for incident electrons energies below 80 keV, atomic displacements rarely occur using accelerating voltages below 80 kV. Monovacancies and edges are significantly less stable because double-coordinated carbon atoms have a much lower threshold energy for ejection (approx. 14 eV).

Fig. 1.2 shows different defect configurations revealed by atomic-resolution STEM. Panel a-c shows three different stable divacancy configurations which can be transformed into each other by bond rotations induced by the electron beam. Remarkably, the bond rotations can also easily occur at GBs. Fig. 1.2d shows a typical graphene grain boundary with a characteristic sequence of polygonal rings. Fig. 1.2e shows the same location after another scan. Clearly, the configuration (characteristic sequence) has changed. Fig. 1.2f–h shows different Si dopant configurations revealed by the Z-contrast of STEM.
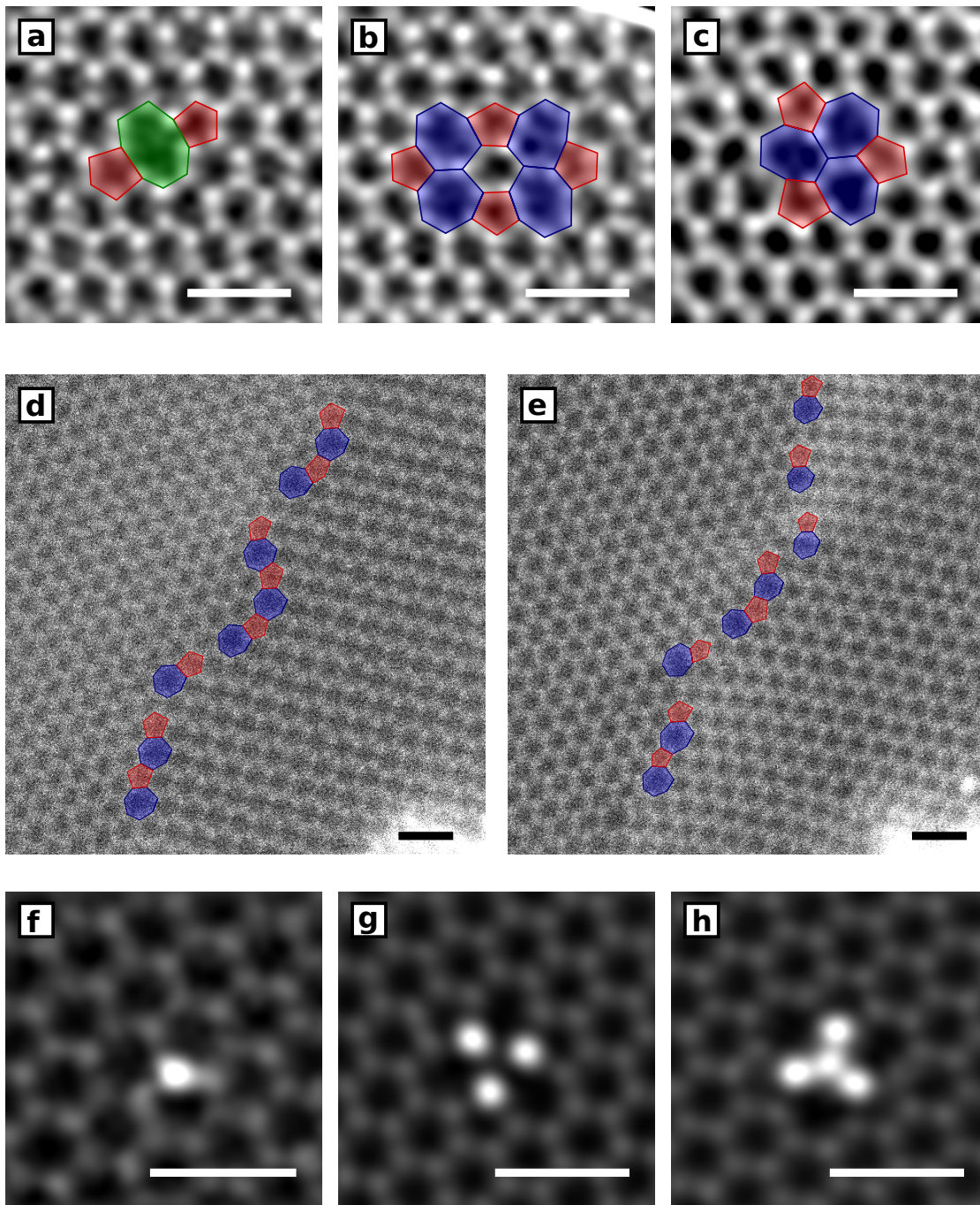
Figure 1.2: **STEM images of point and line defects in graphene.** (a) 585-divacancy. (b) 5555-6-7777 divacancy (butterfly defect). (c) 555777 divacancy. (d,e) Graphene grain boundaries at two consecutive scans. Red, blue and green overlays correspond to pentagons, heptagons and octagons, respectively. (f-h) Si substitution, Si-trimer and Si-tetramer in graphene. Scale bar is 0.5 nm.

1.3 The road to atomic resolution

Already in the late 19th century, the theory of optical microscopy and its resolving power, which is ultimately limited by the wavelength of light, was sufficiently understood. The first magnified image using electrons instead of light was demonstrated in 1931 by Ruska and Knoll, although they initially did not know about de Broglies postulation of the wave nature of electrons in 1924. By the end of Ruska's thesis in 1933, he built a TEM which surpassed the light microscope in resolving power [44]. Despite this significant breakthrough in advanced characterization techniques providing the base for the optimistic prediction that "sooner or later the ultramicroscopy technique will be able to reveal single atoms" (von Ardenne, 1939), it took until 1986 that E. Ruska was awarded the Nobel Prize in Physics, 2 years before his death [45]. Already in 1938, the first STEM was designed and constructed by M. von Ardenne reaching a resolution down to 10 nm, but the images where dominated by noise [46]. The next breakthrough in STEM was achieved in 1966 by A. Crewe, who successfully incorporated a cold field-emission gun (CFEG) [47, 48]. Four years later he invented the annular dark field detector (ADF) and published images of single heavy atoms [49, 50]. Otto Scherzer showed theoretically in 1936 that static, rotationally symmetric, space-charge-free electron lenses always have a positive spherical aberration coefficient that cannot be eliminated by a lens design as can be done for optical lenses [51]. In practice, the resolution before the era of aberration correction was limited to the order of 50-100 wavelengths instead of being of the same order as in the case of photons. It was again Scherzer who suggested breaking the rotational symmetry using quadrupole and octopole lenses in order to correct the spherical aberration. Huge efforts were made in the 1950s to implement such a system, but the technical complexity and the challenge for a proper alignment and adjustment requested a different design. Hawkes showed in 1963 that a set of hexapoles can create a negative spherical aberration coefficient that could compensate for the problems of round objective lenses, but they still did not result in an actual resolution improvement due to the presence of other aberrations [52]. With the development of more stable power supplies, faster computers and the possibility to automatize aberration measurements and corrections, the first full spherical aberration corrected microscopes were created almost 40 years later by Haider, Rose et al. for TEM [53] and Krivanek et al. for STEM [54]. This allows atomic resolution at electron energies down to 60 keV which is crucial for probing light elements and beam-sensitive materials. On the downside, the influence of chromatic aberrations becomes more relevant. Recent projects worked successfully on chromatic aberration correction in a TEM [55] or monochromation of the electron source in a STEM, which has the – probably more important – side effect of increasing the energy resolution to approx. 5 meV in electron energy loss spectroscopy [56, 57]. This allows to reach sub-Å resolution at 20–30 keV electrons corresponding to a resolution of 15 times the wavelength [55].

1.4 Motivation and Outline

The breakthrough of achieving atomic resolution with moderate beam energies resulted in a huge scientific output of S/TEM research of beam sensitive materials such as graphene and other low-dimensional materials. The community of atomic-resolution S/TEM is constantly

increasing due to the opportunity for imaging and manipulating individual atoms, understanding the interaction of electrons with a single atom, observing chemical reactions, analyzing electronic configurations and much more. Despite the power and elegance of these instruments, the 3D structure of 2D materials – especially at defect sites – has not been revealed yet. This is mainly because a single image only provides a projection of the 3D object. As a theoretical approach, large unit cells of embedded defects are usually relaxed by energy minimization. This approach, however, requires periodic boundary conditions of the model. Moreover, there is always a need for experimental confirmation. Conventional reconstruction methods are not easily applicable on 2D materials, as I will describe in the following section.

The goal of this thesis has been to develop a new reconstruction approach to reveal new insights into the 3D structure of defects in 2D materials and to apply it to experimental STEM data from state-of-the-art instruments. In particular, my work shows that defects are far from being flat, but rather lead to significant out of plane deformations. For example, graphene GBs show a very interesting buckling behaviour, depending on the misorientation angle of the grains. Specifically, extended defects with ad-dimers lead to a strong bump while a circular GB remains flat. Beside intrinsic structural characteristics, my work also reveals insights into electron-beam induced dynamics. For example, this work not only directly visualizes the 3D geometry of a Si impurity in graphene, but also reveals its flipping between up- and down- configurations with respect to the graphene plane. Similar behavior is shown for more complex Si defects, such as Si tri- and tetramers. Also, the expected deformation of mixed-dimensional heterostructures – as shown for nanotubes on graphene – is experimentally confirmed in this thesis. In total, this thesis provides key information about the basic physics and structural properties generally and graphene specifically.

Experimental and computational methods

2.1 (Scanning) transmission electron microscopy

Although the goals of high-resolution STEM and TEM are very similar - identifying the position of individual atoms – the image formation mechanisms are quite different. In conventional high-resolution TEM, the sample is illuminated by a coherent parallel beam and the image is mainly formed by coherent interference stemming from the beam-specimen interaction where the contrast and resolution is given by the contrast transfer function (CTF). High-resolution TEM interpretation is often difficult due to the CTF's sensitivity to residual aberrations and focus values. In order to directly interpret the image in terms of projected structure, the CTF has to have a maximized passband from zero up to the microscope's information limit. This requires optimal conditions which might drift over time. However, high-resolution TEM's phase-contrast based image formation technique requires significantly less dose than STEM, which is based on incoherent scattering. In STEM, the incident electron beam is focused to an Ångstrom sized probe and scanned across the sample. The electron beam interacts with the specimen generating a broad variety of signals down to the atomic scale. Fig. 2.1 summarizes the relevant signals, which can be extracted when an electron interacts with a material.

For STEM, the image formation from medium to heavy elements, the electrons that were elastically scattered to high angles are collected by an annular detector, which consists of a scintillator, a photomultiplier and additional electronic amplifiers. The elastic scattering of a charged particle with the potential of an atomic nucleus was already observed in the beginning of the 20th century by Ernst Rutherford and is therefore referred to as Rutherford scattering. The resulting contrast is strongly dependent on the atomic number as Z [58], allowing much easier interpretation of the obtained image. For graphene, it turns out that enabling good contrast is obtainable when using a medium-angle annular dark field (MAADF) detector, which usually covers the range from 58–200 mrad. This detector configuration, however, also includes partially coherent electrons detected due to the Bragg scattering. In order to minimize the partial phase contrast, one has to use higher inner detector angles (e.g. 80 mrad) which is then referred to as high-angle annular dark field (HAADF) STEM. Unfortunately, the detection of only high angle scattered electrons reduces the image signal, especially for light elements like carbon.

Secondly, inelastically scattered electrons, which are usually scattered to very low angles, go through the central hole of the ADF detector and can be used to perform electron energy loss

spectroscopy (EELS). EELS is usually used for elemental identification, analysis of chemical bonds, plasmons and even phonons. For the first two cases, the energy-loss of the electrons arises typically from core ionization events, in which the incident electron excites an electron from its ground state in the specific shell to the vacuum level. Depending on the shell from which the ionization occurs, the corresponding EELS edge is referred as the K, L, M... -edge. Since binding electrons have relatively large energies, the energy losses due to these processes typically start at about 100 eV. The fine structure of the core-edge depends on the exact electronic state and therefore on the local chemical bonding. This technique is advantageous for low atomic numbers due to the higher scattering cross-section of low energy losses.

Because the interaction of electrons with a specimen emits also X-rays with characteristic energies, energy-dispersive X-ray spectroscopy (EDX) measurements are also possible with the spatial resolution given by the probe size. It is closely related to EELS because the characteristic photons are emitted by electrons which are relaxed from the outer shells to the hole in the core shell (see Fig. 2.1 right). This technique is more sensitive to higher energy losses.

All of these signals can be extracted as a function of probe position resulting in a 3D dataset in the case of EELS and EDX. This data cube can be reduced again into a 2D image, usually by extracting the signal of an energy window around a certain peak. This leads to a map which e.g. shows the location of a specific element and can be correlated with the simultaneously recorded ADF image.

Due to the high required accuracy of the electron probe, which defines the spatial resolution in STEM, very stable conditions are required for this method. Usually these microscopes are in a separate room, decoupled from the ground and have μ metal shielding to avoid mechanical vibrations and external electromagnetic fields. As already mentioned, state-of-the-art aberration correctors achieve sub-Ångström probes at relatively low acceleration volages down to 60 keV and even 20 keV when the microscope is equipped with a chromatic aberration corrector. On the spectroscopic side, the EELS resolution is primarily limited by the energy spread of the incident electrons, which can be monochromated by dedicated energy filters.

The experiments in this thesis were conducted with a Nion UltraSTEM100, which is equipped with a CFEG providing an electron beam with high brightness and an energy width of ca. 0.3 eV. Its aberration correctors are quadrupole-octopole (QO) lenses which correct all geometric aberrations up to 5th order providing a probe size of ca. 1.3 Å at 60 keV [54]. The – very simplified – principle of the correction QO lens system is as follows: The quadrupole lenses focus the beam along one transverse axis and defocus the beam along the perpendicular axis. This creates an elliptic beam which is called a line focus. The octopole has a negative third-order spherical aberration which directly compensates for the third-order aberrations. Another set of QO lenses repeats the correction to the beam along the perpendicular axis and a final quadrupole produces a round beam again. Residual four-fold aberrations are further corrected by another octopole lens. The instrument's excellent ultra-high vacuum (UHV) has a typical pressure of 10^{-11} mbar at the gun and 10^{-9} mbar at the sample. This is crucial for minimizing the contamination on the sample as well as for higher performance and lifetime on the gun. Additionally, UHV reduces the interaction of the sample with residual ionized gas molecules which would lead to chemical etching. The specimen stage's design minimizes drifts. A MAADF, a HAADF and a bright-field detector are included in the detection system as well as a CCD
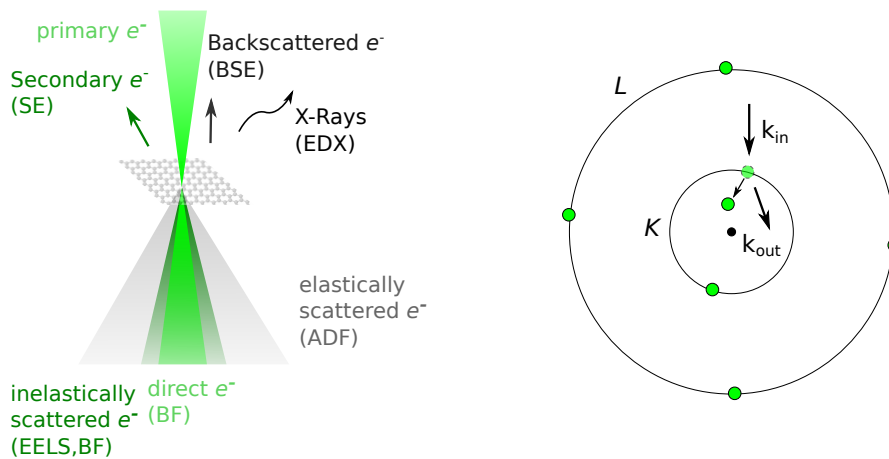
Figure 2.1: **Signals obtained when an electron interacts with a material.** (a) Schematics of the possibilities of interactions and signal detection method. Only the most relevant for (S)TEM are shown. (b) Schematics of the inelastic scattering of an incoming electron.

camera for tuning and aligning the electron beam. For spectroscopy, it is further equipped with a Gatan EEL spectrometer.

2.2 STEM simulations

2.2.1 Multislice algorithm

Although the interpretation of STEM signals is easier than in TEM, quantitative analysis of the experimental output often requires comparison with simulations. The number of open-source softwares for quantitative image simulations containing TEM, STEM, CBED (converged-beam electron diffraction) and other techniques are increasing and almost all of them are based on the multislice or the Bloch-wave algorithm. The multislice algorithm requires lower mathematical computations and is therefore preferred and briefly summarized in the following paragraph. In the multi-slice approach, the specimen is divided into many thin slices (ideally one slice per atomic plane perpendicular to the optical axis) and the atomic potential is projected within the slices [59]. In STEM, the initial converged and optionally aberrated electron beam, represented by the wavefunction $\psi_p(x)$, is propagating through the specimen's potential. In the weak-phase object approximation (which assumes thin specimens that induce minimal phase shifts), each slice causes a position-dependent phase shift that is represented by the specimen transmission function $t(x) = exp(-i\sigma v_z(x))$ where $v_z(x)$ is the projected potential in a specific slice and $\sigma = 2\pi me\lambda h^{-2}$ the interaction parameter. The sample potential can be rapidly modeled by a superposition of isolated atom potentials, which have been calculated for every element of the periodic table. However, if modifications of the electronic states (e.g. due to chemical bonding) are not negligible, density functional theory (DFT) calculations can reveal the electronic charge density and therefore provide more realistic specimen potentials. The exit-wave function is iteratively calculated and then finally incoherently integrated over the detector geometry $D(k)$ to
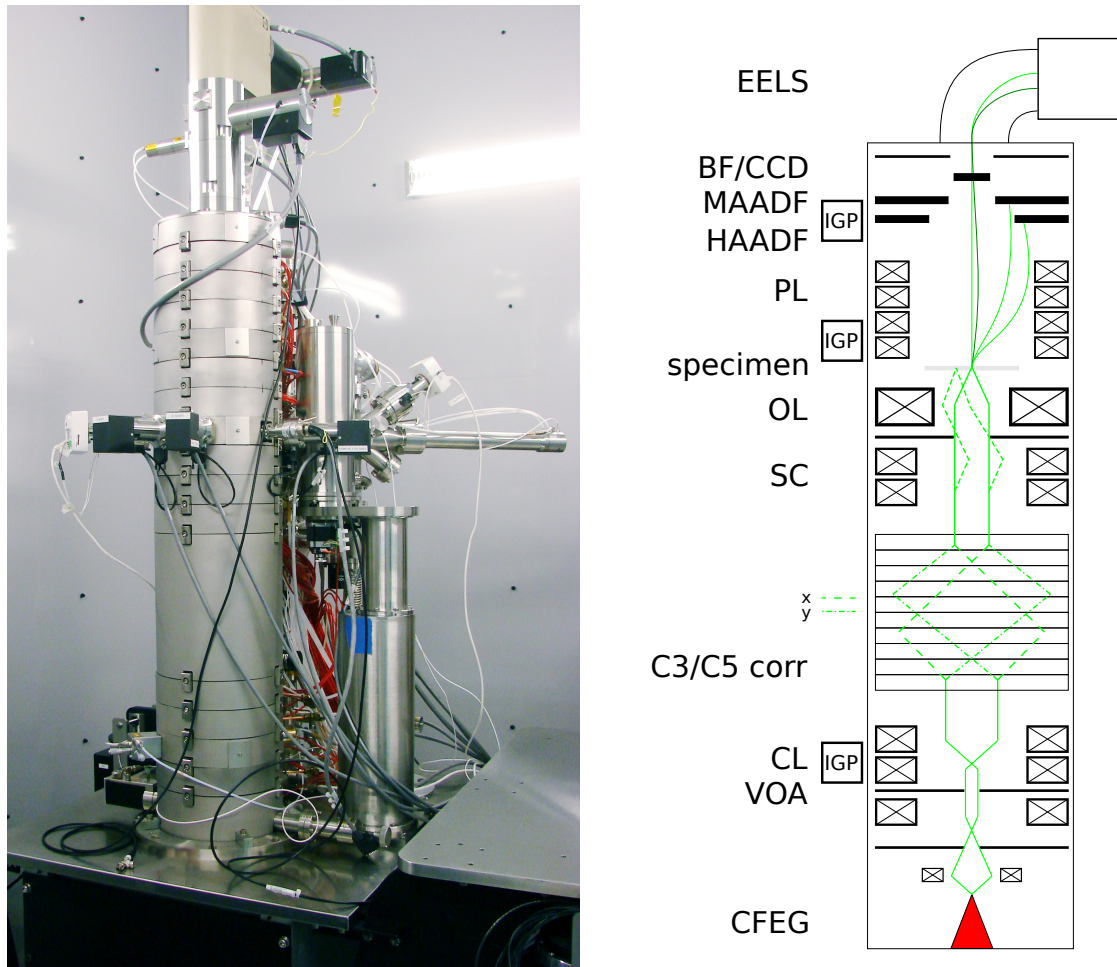
Figure 2.2: **Picture (left) and schematic diagram (right) of a Nion UltraSTEM100 in Vienna. The simplified ray path of the electrons is labeled in green, from bottom to top.** Abbreviations from bottom to top: cold-field electron gun (CFEG), virtual objective aperture (VOA), ion-getter pump (IGP), condenser lenses (CL), third-order and fifth order aberration correctors (C3/C5 corr), scan coils (SC), projector lenses (PL), high-angle annular dark-field (HAADF), medium-angle annular dark-field (MAADF), bright-field/charged coupled device (BF/CCD) and electron-energy loss spectroscope (EELS).

form the final signal g as a function of probe position x_p:

$$g(x_p) = \int |FT(\psi_{ex}(x,x_p))|^2 \cdot D(k)\, dk$$

The signal has to be calculated for every pixel in the image and is therefore a very computationally expensive task.

Due to the reciprocity of TEM and STEM, the formulas underlying TEM simulations remain the same, but have to be applied in a different order. Here, the initial wave function is a (non-aberrated) plane wave propagating through the specimen. The aberrations of the objective lens are then included in the exit wave by a convolution with the CTF. The intensity is then the resulting wave function squared. TEM simulations are significantly faster due to the parallel acquisition of a single plane wave.

2.2.2 Convolution method

The task of STEM simulation can be simplified in the case of 2D materials, where each individual atom represents an isolated potential in the image. The resulting image contrast is given by a convolution of a 2D delta function δ_{xy} representing the atomic potential with a point spread function (PSF) representing the (aberrated) electron beam. The coefficient of the delta function is directly related to the intensity of the atoms. In detail, the phase of the aberrated wave front at a polar angle θ and azimuthal angle ϕ is modeled as

$$
\begin{aligned}
\psi(\theta_x, \theta_y) = (2\pi/\lambda) \cdot (&C_1\, (\theta_x^2 + \theta_y^2)/2 \\
&+ C_{1,2a}\, (\theta_x^2 - \theta_y^2)/2 + C_{1,2b}\, \theta_x\, \theta_y \\
&+ C_{2,1a}\, \theta_x\, (\theta_x^2 - \theta_y^2)/3 + C_{2,1b}\, \theta_y(\theta_x^2 - \theta_y^2)/3 \\
&+ C_{2,3a}\, \theta_x\, (\theta_x^2 - 3\,\theta_y^2)/3 + C_{2,3b}\, \theta_y(3\,\theta_x^2 - \theta_y^2)/3)
\end{aligned}
\tag{2.1}
$$

where $\theta_x = \theta \cdot cos(\phi)$, $\theta_y = \theta \cdot sin(\phi)$, C_1 is the aberration coefficient of the defocus, $C_{1,2a}$ and $C_{1,2b}$ are the aberration coefficients of the two-fold astigmatism, $C_{2,1a}$ and $C_{2,1b}$ are the aberration coefficients of the coma and $C_{2,3a}$ and $C_{2,3b}$ are the aberration coefficients of the three-fold astigmatism [59]. λ is the wavelength of the incident electrons. After multiplying the resulting wave function with an aperture function A_θ (which gives the convergence angle), the PSF is given by the squared modulus of the inverse Fourier transform:

$$PSF(x,y) = \left| F^{-1}(\psi(\theta_x, \theta_y) \cdot A_\theta) \right|^2$$

Finally, the PSF is convoluted with the delta lattice of the model to obtain the signal $g(x,y)$:

$$g(x,y) = PSF * \delta_{xy}$$

To take the broadening effect of the finite electron source size into account, the result is further convoluted by a Gaussian function.

Fig. 2.3e and g shows the simulation using the simplified convolution method where the model

in panel d is convolved with the aberrated electron probe (panel c) before and after Gaussian blurring, respectively. A comparison with a quantitative simulation with the same parameters using QSTEM [60], presented in Fig. 2.3f and g, shows very good agreement between these two methods.

The main advantage of this convolution simulation method is the much faster computational time. This might be important (e.g. for the work presented in this thesis) for numerical optimization processes, where STEM simulations are required for each iteration. In addition, a modified intensity analysis can be used using this simulation method, when the atomic intensities are fitted to the experimental data. This has the advantage that aberrations can be taken into account which are often neglected in conventional analysis methods [58].

2.3 Raman spectroscopy

Although S/TEM can identify the position of each atom and is therefore a very powerful tool for structural characterization of 2D materials, it has several drawbacks. Firstly, it requires suspended samples and therefore requires the prepared sample to be transferred to a conventional TEM grid. Usually it is necessary to specify the quality, the number of layers, the density of defects etc. of the material before the transfer procedure. In addition, S/TEM is not a convenient tool to characterize the structural properties on a micrometer scale – except for diffraction analysis. To address this, this work also used Raman spectroscopy. It can be a very reliable tool for identifying the number of layers, quantifying the density of defects and distinguishing different isotopes of materials without needing additional post sample preparation or UHV. The Raman spectrum arises from inelastic scattering of photons by atomic vibrations (phonons). In a conventional Raman setup, a monochromated laser beam illuminates the sample and gets reflected. The majority of the photons are elastically scattered and do not contain information about the sample; however, a tiny fraction of the incident photons are interacting with the phonon modes and therefore lose energy when a phonon is created (Stokes scattering) or gain energy when a phonon is absorbed (anti-Stokes scattering). The quantized phonon states and therefore the transferred energy is characteristic for the material, including its intrinsic properties such as temperature, doping level and strain. Although a complete understanding of the phonon band structure at high symmetry directions and their phonon-photon scattering processes is essential for the complete interpretation of Raman spectra, a detailed description of the rather complex physics of Raman scattering is beyond the scope of this thesis. This section is intended to give a brief introduction into the main Raman peaks and related phonon modes used for characterizing graphene.

A main characteristic peak for graphitic sp^2 carbon bonds is the G-peak with an energy corresponding to $1580\,\mathrm{cm}^{-1}$. It arises from the doubly degenerate (longitudinal optical (LO) and in-plane transverse optical (TO)) phonon mode at the Brillouin zone center Γ ($k = 0$) (see Fig. 2.4a,b). Because there is no momentum transfer, the G-peak is therefore independent of the initial photon energy. A very characteristic Raman peak of graphene is located at approx. $2700\,\mathrm{cm}^{-1}$ arising from a phonon close to the K point (at the Dirac cone). This phonon mode is called "breathing" mode (cf. Fig. 2.4a, bottom). The mechanism includes a double resonance process that links the phonon wave vectors to the electronic band structure. Figure 2.4c shows a schematic of the process. Here, the incident photon induces an electron-hole excitation. The

a

$$\psi_p(x, x_p)$$

$$\psi_1(x, x_p) = \psi_p(x, x_p) \cdot t_1(x)$$
$$\psi_2(x, x_p) = \psi_1(x, x_p) \cdot t_2(x)$$
$$\psi_3(x, x_p) = \psi_2(x, x_p) \cdot t_1(x)$$
$$\psi_t(x, x_p) = \psi_3(x, x_p) \cdot t_2(x)$$
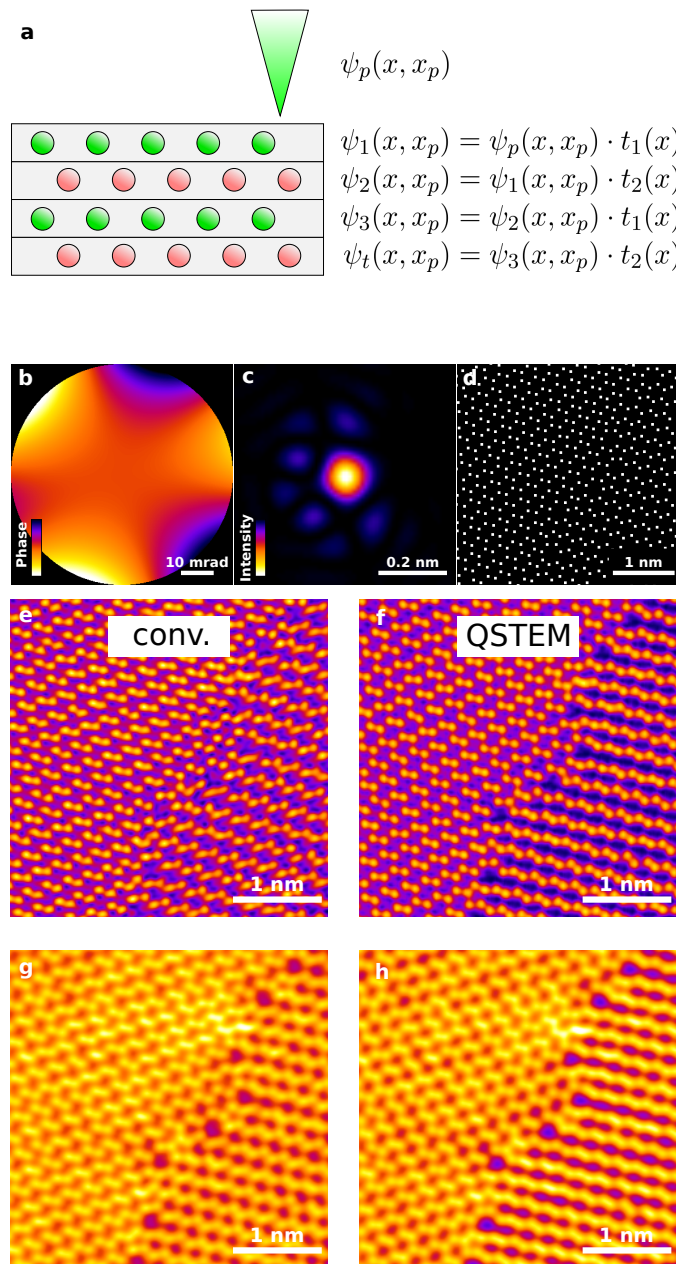
Figure 2.3: **Principle of STEM simulations using the multislice method and the convolution method.** (a) Schematic of the multislice algorithm, where the atomic planes are classified in different slices. Each slice represents a projection potential translated into a transmission function $t(x)$. (b) Calculated phase of the electron probe. (c) Calculated intensity probe profile. (d) Delta potential representing the atomic positions of a GB. (e,f) STEM simulations using the convolution method and QSTEM, respectively. (g,h) STEM simulations of panel e and f with a Gaussian blur, respectively.

excited electron scatters first with a phonon with wavevector k_D exchanging its momentum. Then, electron-hole recombination occurs emitting a photon with different energy before the electron scatters with another phonon with wavevector $-k_D$. The resulting 2D Raman peak frequency is twice that of the wave number of the scattered phonon $k_D = 1350\,\text{cm}^{-1}$, which is in the highest optical branch at the K-point. Since these zone-boundary phonons do not satisfy the Raman fundamental selection rule, they are not seen in first order Raman spectra of defect-free graphite [61]. Therefore, the resulting D peak only occurs when the lattice symmetry is broken (e.g. at defects). The D as well as the 2D peak are dependent on the excitation wavelength. Figure 2.4d shows a typical Raman spectrum of graphene on a copper substrate with a wavelength of 488 nm (blue light), showing the main peaks of graphene. The exponential-like background corresponds to photoluminescence from the copper substrate. This phenomenon involves the relaxation of excited electrons from the d-states to the conduction band. The first indication that the spectrum arises from a monolayer is the ratio between the 2D and the G peak intensity, which is about 3:1. For a bilayer, the ratio decreases to 1 and further decreases with increasing number of layers. The second fingerprint of graphene is the full width at half maximum (FWHM) of the 2D peak, which is about $20\,\text{cm}^{-1}$ for monolayer and significantly larger for bilayer due to the split of the peak into 4 components [61]. Because the D peak is related to the defect density in the sample, the barely visible peak in the corresponding specimen indicates the absence of a significant number of defects.

2.4 Sample preparation

2.4.1 Chemical vapor deposition

Mechanical exfoliation of single layer graphene by peeling off graphite layer-by-layer is still regarded as a reliable tool to prepare high quality graphene samples. The main drawback is obviously the limited grain size. As an alternative, chemical vapor deposition (CVD) is one of the commonly used synthesis techniques for the fabrication of graphene. A schematics of a typical CVD setup and its reaction steps is presented in Fig. 2.5. In brief, a carbonaceous gas (e.g. methane) is inserted into a quartz tube (i) where the gas decomposes in the presence of a catalyst (e.g. copper) at high temperatures (ca. 1000 °C) (ii). The same catalyst also acts as a substrate for the migration (iii) and nucleation (iv) of the carbon atoms. The decomposed carbon atoms migrate at the copper substrate and form the graphene lattice. The process is usually run in an Ar/H$_2$ atmosphere. While the argon acts as a protection gas, the hydrogen reacts with incompletely dehydrogenated molecules that are attached to the graphene grain and can desorb these unwanted molecules. This is crucial for obtaining high quality graphene samples. An optical image of individual graphene grains on the copper substrate is presented in Fig. 2.5b. To obtain the pronounced contrast between the graphene and the copper, the substrate was annealed in air at about 80 °C for 2 min. While the copper substrate oxidizes under these conditions, the graphene protects the copper beneath it from oxidation, resulting in a visible contrast. The image also shows two copper grains highlighted by the dashed lines, where the graphene grain sizes are significantly smaller due to the higher probability of carbon nucleation at the defect sites. Although the grain size can be controlled by smoothing the substrate surface and optimizing the

a

(i)

LO/TO

G band

(ii)

LO/LA

D/2D band

b

Phonon energy (eV)

0.20 LO
(i) TO

0.15 (ii)

LA

0.10 ZO

0.05

TA

0.00 ZA

Γ   M   K   Γ

c

E   E

E_{in} K E_{out} K
      k   k

E

E_{in} K E_{out}
            k

d

counts [a.u]

$E_{in} = 2.54$ eV   2D

G

D

1000   2000   3000
Raman shift [1/cm]

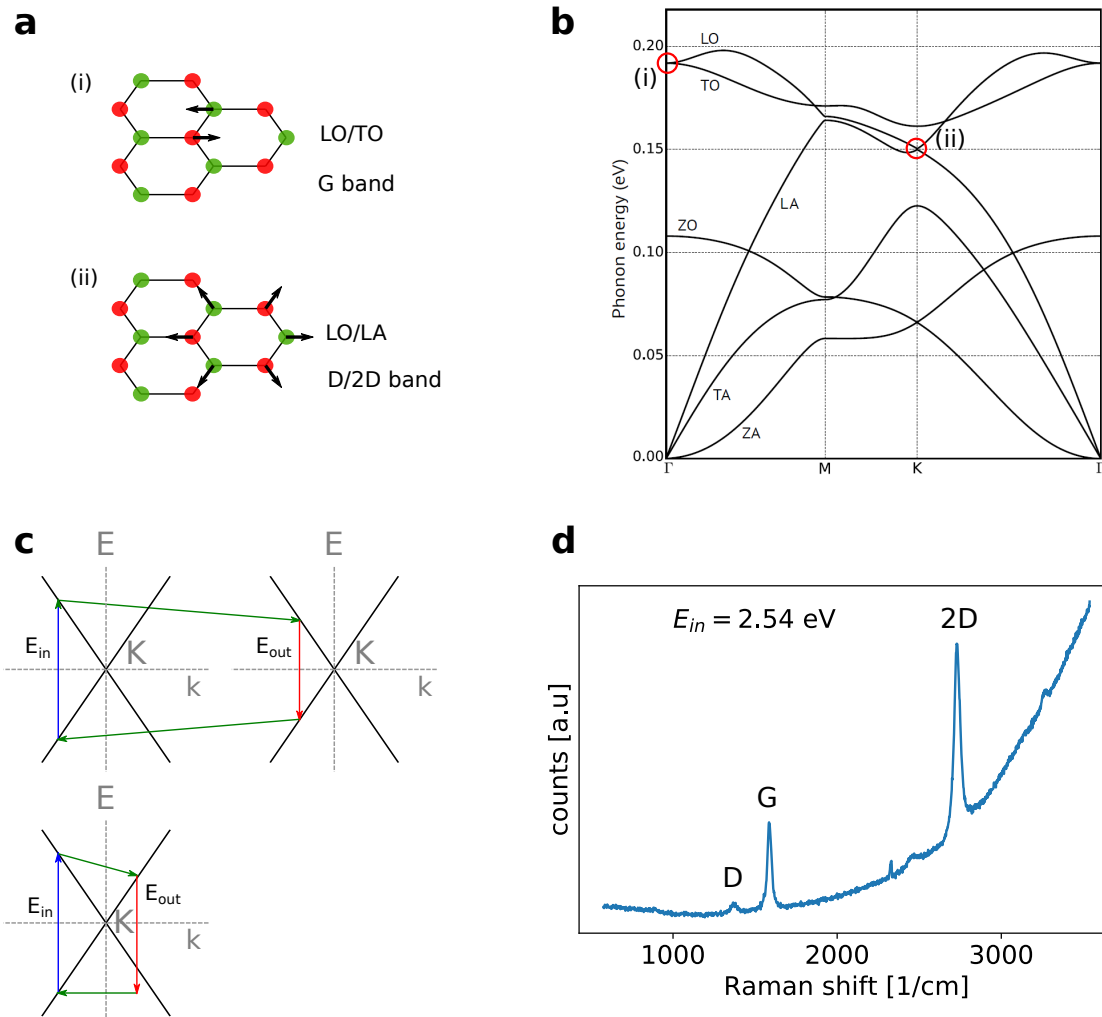Figure 2.4: **Raman spectroscopy of graphene.** (a) Schematics of the lattice vibrations causing the G, D and 2D peak in the Raman spectrum. (b) Phonon dispersion along high symmetry directions of graphene (Ref. from [43]). (c) Schematics of the double resonant scattering process for the 2D peak (top) and the D peak (bottom), following Ref. [62]. (d) Typical Raman spectrum of monolayer graphene.

growth parameters, the presence of grain boundaries can never be fully avoided, and these alter the graphene's properties. Because the main goal of this work is to study defects of graphene, I will briefly discuss the parameters used in this work to get a very polycrystalline graphene sample. In principle, a sample with very small grain sizes can be obtained by increasing the nucleation density of graphene. Defects of the copper substrate, for example, act as nucleation site for the atoms. Firstly, any pre-cleaning step, especially chemical polishing, has been skipped. This preserves the roughness of the copper foil caused by the fabrication process. Because long annealing of the copper substrate close to its melting point increases its grain size and smooths its surface, the graphene growth was started as soon as the desired temperature has been reached. The growth temperature was set to 960 °C which is relatively low compared to conventional growth conditions. As precursor, ethane was used which has a higher carbon-hydrogen ratio than methane resulting in faster growth and therefore increased the chance for nucleation at copper defects. The Ar/H_2 ratio was 0.95 which is higher than values reported in the literature [63]. The significantly reduced concentration of hydrogen decreases the desorption rate which also lowers the "quality" of the sample. Finally, to further increase the growth speed and therefore the nucleation density, the flow rate of the ethane precursor was set to a high value (approx. 200 sccm) resulting in a total growth time of only 1–2 min. We pre-characterized the concentration of defects qualitatively by Raman spectroscopy. The relation between the G and 2D peak of the Raman spectrum in Fig. 2.6 is characteristic for monolayer graphene. The 2D/G ratio is slightly smaller than for a perfect monolayer (see Fig 2.4d) indicating also the presence of bilayer graphene. This might be due to the accelerated growth when using ethane as the precursor. More importantly, the presence of a significant D peak is a promising indication for the presence of a significant amount of defects.

2.4.2 Transfer to TEM grids

In order to study the fabricated 2D materials by high resolution S/TEM, a transfer to a suspended state is necessary. Any substrate would significantly disturb the signal of the transmitted electrons. Standard TEM grids (3 mm in diameter, 200 mesh gold grids), which are coated with a perforated amorphous carbon foil (hole diameter approx. 1.6 μm), are usually used and commercially available. A standard transfer method of graphene on the copper substrate to a TEM grid is illustrated in Fig. 2.5c. The grid is attached to the sample while the holey carbon foil is facing the graphene sheet by using a drop of isopropanol (IPA). After the IPA evaporated and the grid is adhered to the sample, the substrate/graphene/grid sandwich is released on the surface of a 10% $FeCl_3$ solution which etches the copper substrate. Optionally, the (unwanted) graphene sheet on the bottom side of the Cu foil can be removed, for example by oxygen plasma. After several hours, the Cu is completely removed and the remaining graphene on the grid is rinsed in deionized water and IPA.
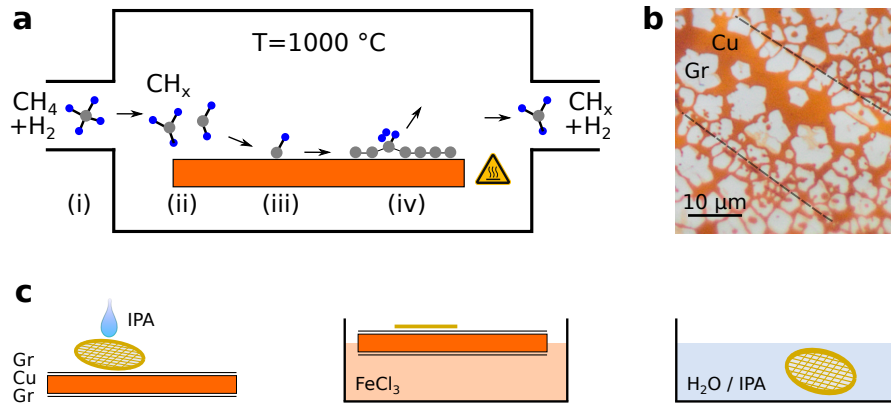
Figure 2.5: **CVD synthesis of graphene and its transfer to TEM grids.** (a) Schematics of the CVD process. (b) Optical images of graphene on an oxidized Cu foil. (c) Schematics of the transfer of graphene on Cu to a TEM grid.
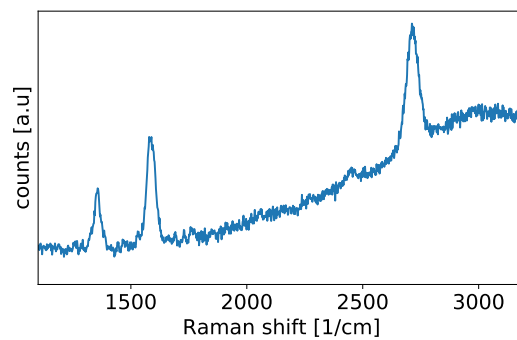

Figure 2.6: **Raman spectrum of defect-rich graphene.**

Method development for 3D reconstruction of one-atomic layer materials

This chapter is dedicated to the methods we have developed for the extraction of the 3D positions of each atom. Although the principle of the method is already published in the first paper of chapter 4, this chapter provides a closer look at the details and implementation of the method. A step-by-step guide through the reconstruction method used with the published code is given in the appendix. In this chapter, I will firstly briefly review conventional reconstruction methods and their limitations. Then, I will describe details of the reconstruction method which requires two atomically resolved STEM images that are tilted relatively to each other.

3.1 Electron tomography as conventional 3D reconstruction method

Although state-of-the-art aberration corrected (S)TEMs already reach resolutions below 1 Å and therefore easily resolve all interatomic distances, they only provides a single projection and therefore does not enable retrieving information about the specimen along the electron beam direction. The need for determining 3D TEM specimen structure justifies the ongoing effort into the rapid development of reconstruction methods. In order to retrieve the 3D structure of a thin sample in a (S)TEM, electron tomography (ET) has emerged as a generally reliable method. ET was introduced in 1968 and has been primarily used to determine the 3D structure of biological samples [64]. To perform ET, the sample is tilted over a large range of tilt angles. After alignment of the set of projections a Fourier-based iterative algorithm such as SIRT (Simultaneous Iterative Reconstruction Technique) combines the dataset into a 3D structure [65]. Although this method was successfully developed and applied down to atomic-resolution [66, 67], it suffers from several drawbacks which makes this approach suboptimal for beam-sensitive materials such as 2D materials and their defects. One main issue is the amount of dose required for the whole tomographic series which makes defects frequently change their configuration even at moderate TEM acceleration voltages. There have been several studies of the experimental reconstruction of using a limited amount of dose. For example, on the basis of a defocus-series, the structure of defect-free graphene has been revealed (Focal series reconstruction) [68]. A statistical analysis of the scattering cross-sections was successfully implemented to recover the 3D structure of nanoparticles in STEM [69]. Another reconstruction approach extracted the

structure of clustered divacancies from atom contrast variations in the TEM [70]. However, this approach requires that the intensity of each atom can be measured without being affected in any way by the intensity of the neighboring atoms, which is difficult to avoid in presence of residual aberrations, finite resolution, and very short projected distances in non-flat structures. Any kind of polynomial fit relaxes that requirement, but then the reconstruction does not reveal the position of individual atoms, but only averaged local heights. Due to recent advances in the correction of chromatic aberrations, the depth-sensitivity can be increased to reveal the buckling of dislocations, but the relatively large noise in the resulting 3D model requires smoothing of the out-of-plane coordinates [71]. Despite the large effort to develop methods to retrieve the 3D structure of defects in 2D materials such as graphene GBs, they remain experimentally unquantified. The following section describes the new method used in this work.

3.2 3D reconstruction from two atomically resolved STEM images

From a single atomically-resolved STEM image, the 2D coordinate (i.e. x-y coordinate) of each atom (in case of a one-atomic layer material) can be accurately determined. In order to extract the out-of-plane coordinate (i.e. z-coordinate), the atom has to be measured from a different perspective. This can be realized by tilting the sample, which leads to a translation of the atom in the projection. The magnitude of the displacement is directly dependent on the z-coordinate. This simple geometric view of atoms should demonstrate, that already two views of a single atom are sufficient to determine the x-y-z position. The relative displacement of an atom in the (tilted) projection plane caused by a height difference is schematically shown in Fig. 3.1. If an atom (labeled in gray) is displaced by Δz orthogonal to the projection plane (labeled in transparent gray with dashed circle), there is no shift in the projection plane when it is viewed from the orthogonal direction (View 1). When the configuration is observed from a different angle (View 2), the displaced atom is also shifted by Δx in the projection.

The reconstruction method is based on this simple geometric relation between the pair of projections and the 3D coordinate. Consequently, for a set of atomically resolved STEM images, two prerequisites are required for the reconstruction: (1) Each atom has to be visible individually in the projections, and (2) the connectivity matrix can be obtained and shows unambiguously which atom is which in the comparison of the views. For a single atomic layer material, such as graphene and hBN, both requirements can be fulfilled. For this work, graphene is preferred over hBN mainly because of the higher stability under the electron beam. In contrast to graphene, hBN is an insulator and therefore suffers more from ionization damage. This makes it even more difficult to obtain two projections with the same atomic configuration.

The reconstruction method is based on an iterative optimization process where the projected atomic positions of a model in both views are compared to the atomic positions of the experimental images. The method includes the following steps:

I. Obtaining the experimental data, namely two relatively tilted atomically resolved STEM images

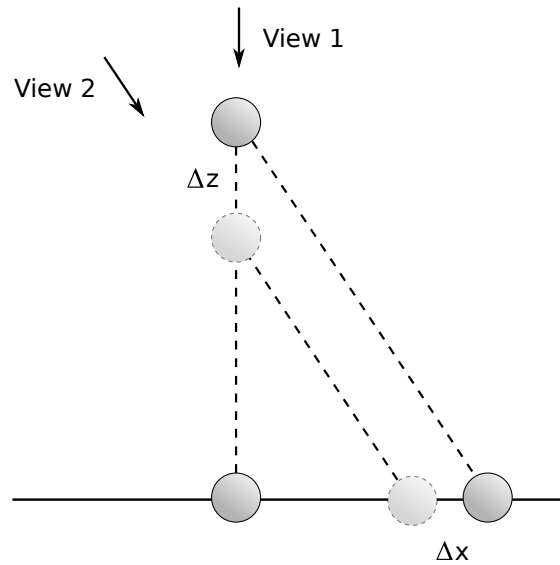II. Extract the atomic positions of all projections

Figure 3.1: **Schematic diagram showing that changing an atom's height results in a different projected position when the atom is viewed from a non-orthogonal direction.**

III. Assign the identical atoms in the projections

IV. Initialize a 3D model and minimize the error function

Points II-IV are the computational tasks. More details of the reconstruction steps are discussed in the following subsections.

3.2.1 Obtaining the experimental data

First, an area of interest has to be found manually. Even this task can be time consuming when defects are analyzed because irregularities in the periodic lattice usually act as charge traps and therefore attract contamination. An ideal sample has minimal contamination and a high defect density. When the region of interest is found (e.g. a large graphene grain boundary), we acquired an image with a decent signal-to-noise ratio (corresponding to an electron dose of approx. $5 \times 10^5 \, e^- \, \text{Å}^{-2}$). Then, because tilting the specimen induces a strong defocus change and lateral translation, we first zoomed out of the area of interest and recorded reference images at several magnifications. Then we tilted the sample while re-adjusting the focus and x-y position of the stage. When the desired angle was reached, we zoomed in again, using the contamination patterns in previously recorded images as reference. We re-focused at an area close to our region of interest in order to minimize the dose applied to the grain boundary. Then we quickly moved to the grain boundary again and acquired the second image. In this approach, the atomic structure usually changes between exposures. However, occasionally a pair of images could be obtained where the atomic network is identical – notably, for every single carbon atom in the region of interest. Fig. 3.2 shows one image sequence of a graphene GB at different magnifications for two
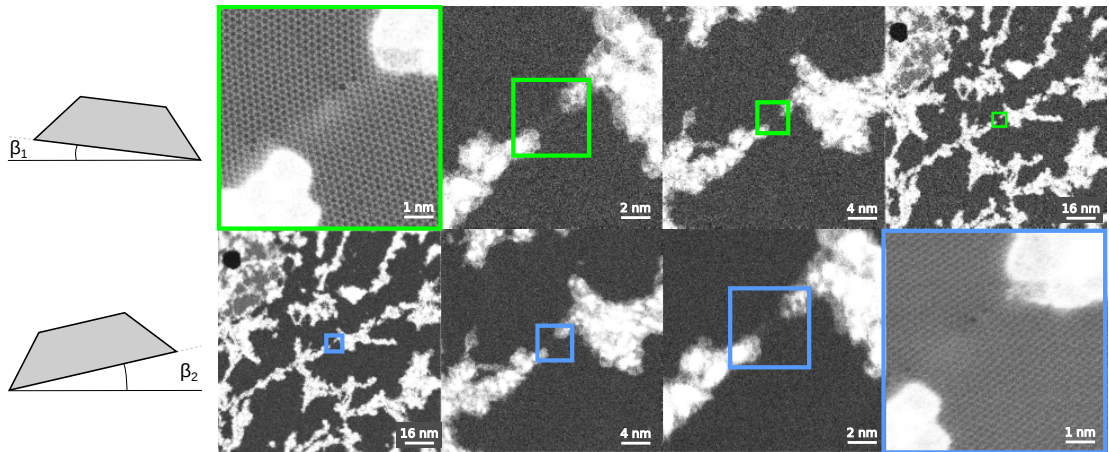
Figure 3.2: **STEM images of a graphene grain boundary at different magnifications with different tilt angles in top and bottom.**

perspective views. The top sequence demonstrates a zoomed out GB, the bottom line zooms into the GB after tilting and re-centering the specimen.

In this case, the two high-resolution STEM images have a specimen tilt of $0°$ and $20°$, respectively. A specimen tilt of $20°$ is at the edge of what is possible with state-of-the-art STEM for atomic resolution due to several reasons. First, the geometric constraints of the sample holder in the column usually do not allow to tilt to a much larger angle. Even if it would be possible to go for higher tilt angles, obtaining atomic resolution becomes more and more problematic. Firstly, the atomic distances are shrinking in the projection with higher sample tilt resulting in intensity overlaps between neighboring carbon atoms. As a consequence, identifying the atomic positions becomes more challenging and less accurate. More importantly, atomic vibrations perpendicular to the graphene plane result in a smearing of the intensities along the tilt direction and therefore reduce the resolution. Although this effect can be reduced by image processing, a too large tilt angle can impede the identification of single atoms.

3.2.2 Automatic extraction of the atomic positions in 2D

To determine the 2D atomistic model, the chosen projections are processed in order to filter out low-frequency variations caused by the tail of the electron beam. A slight Gaussian smoothing helps the algorithm detect the atoms. The contamination is then masked out reducing irrelevant information. For each experimental projection, a model is iteratively modified in order to minimize the error between its simulation and the experimental image. Mathematically speaking, the following error function has to be minimized for each projection:

$$\sigma = \sum_{i=1}^{N} (g(x,y)_i - V_i)^2 ... min$$

where $g(x,y)$ is the STEM simulation (with a list of x and y coordinates corresponding to

the atomic 2D positions) and V is the experimental data, running over all N pixels. We have automated this process in a brute-force approach where the following parameters are iteratively changed.

atom placement Adding an atom at a quasi-random position (higher probability at a position where the error is higher) is obviously the most frequent choice of parameters in the beginning of the reconstruction. In order to avoid accidentally placing two atoms too close to each other, the closest atom is removed when its distance is within a certain threshold distance. The threshold distance can be set manually and depends on the type of defects and the tilt angle, but it turned out that a value of approx. 1 Å is a good compromise between atomic placement and removal. The intensity of the atoms can be optionally fitted, which enables compensating for errors due to random intensity variations or the presence of other elements.

atom shift The precise position of a single atom can be optimized by shifting the atom with sub-pixel accuracy. Also here, the intensity can be optionally fitted. This fine tune of the atomic network becomes more crucial in the later steps of the optimization.

beam parameters Parameters of the simulated electron probe such as aberrations and Gaussian smoothing are also changed in order to improve the match between simulation and experiment. This is effective when the correct number of atoms have already been identified in the process and the fine tuning of the atomic network begins. Modification of the aberrations in the optimization procedure is a crucial step not only for an improved match, but also for improved accuracy of the atomic positions and therefore for the 3D reconstruction. The presence of certain residual aberrations in an atomically resolved STEM image is usually also easily detectable by eye. For example, astigmatism leads to a distortion of the rotational symmetry of the atom intensity. In the corresponding Fourier transform, it results in different intensities of the graphene spots. A residual three-fold astigmatism can lead to different intensities of the atoms in the different sublattice sites of the hexagonal lattice.

field of view The field of view scales the width of the electron probe in pixels and can also be included in the optimization process.

In each step, all of the parameters are only changed by a small amount, keeping the change if the error between the simulation and the experiment is lowered. This optimization approach requires a huge number of iterations, but the simulation results in an excellent match to the experimental image. Fig. 3.3a shows an example of a raw graphene GB, a processed GB where the contamination is masked, a simulation of the final model and the GB with the overlaid 2D model (in purple). Fig. 3.3b shows the simulation (top row) and its pixel-by-pixel squared error (bottom row) at different iteration steps. Initially, the model is empty (i) while atoms are appearing in (ii)–(iv) lowering the error relative to the experimental image. At step (iv), all the atoms are found (the intensities are fitted to the experimental image) and the fine tuning starts by shifting the atoms and changing the aberration coefficients. The corresponding error is minimized and dominated by noise at the final stage of the process (v). In Fig. 3.3 c, the plot of the error is demonstrated. The steps in the plot (in red) are due to adjustment of the simulation parameters (e.g. aberrations, field of view).
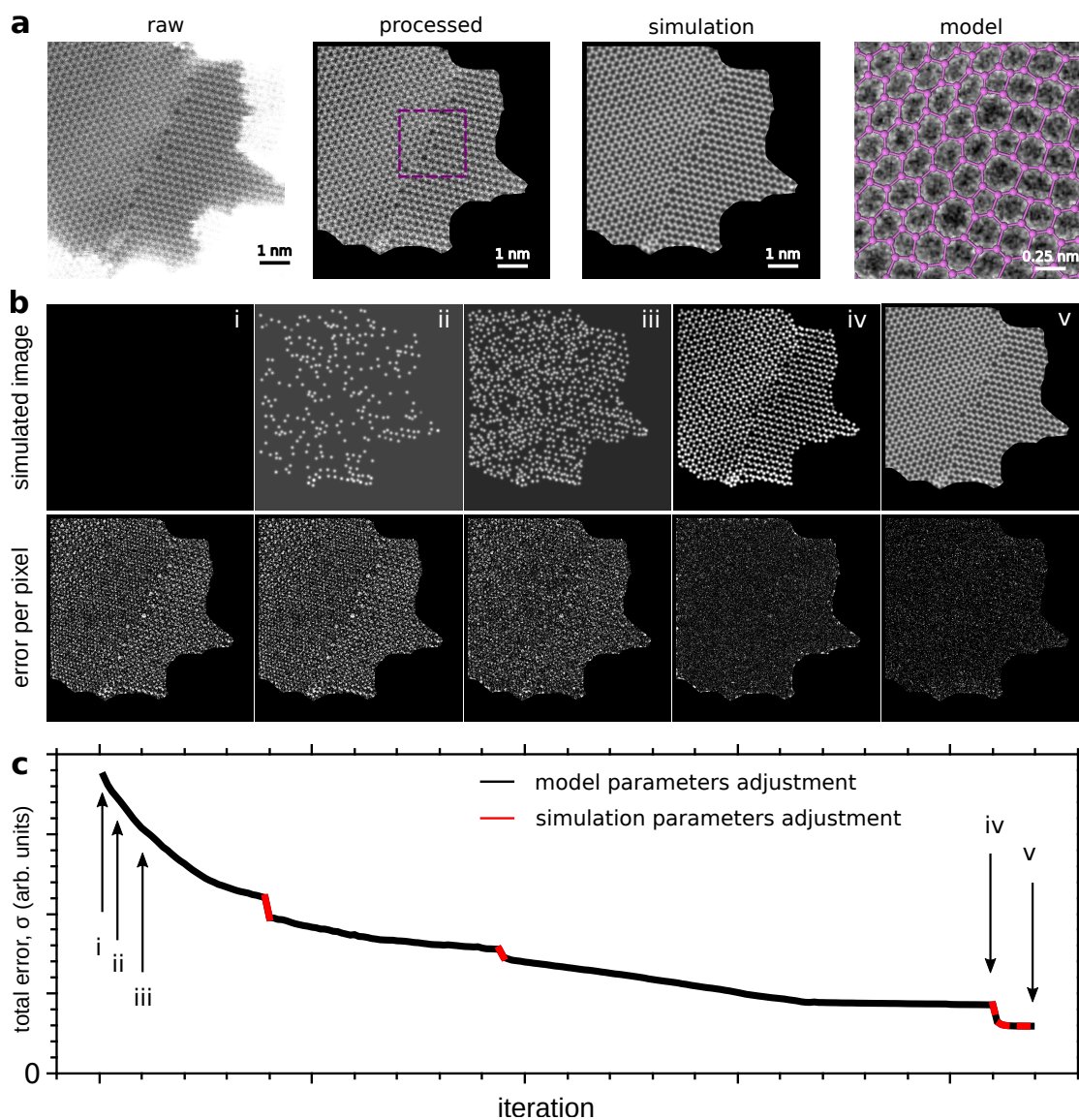
Figure 3.3: **Automatic extraction of the 2D positions of a STEM image** (a) From left to right: Raw image of a graphene GB. Masked and low-frequency bandpass filtered image. STEM simulation of the 2D optimized model. Overlay of the 2D model and the experimental image. (b) Top row: STEM simulation of a model at different stages of the optimization process. The number indicates the iteration step of (c). Bottom row: Pixel-by-pixel squared difference between the experiment and the simulation. (c) Total error as function of iteration.

While there exist hundreds of approaches to identify atomic positions, the improvement from (iv) to (v) in Fig 3.3 is new and results in a very precise assignment of the atomic positions from experimental data. We assume to get a global minimum of the error function when the difference image is dominated by noise.

3.2.3 Automatic assignment of identical atoms in all projections

The heart of the 3D reconstruction is the correct assignment of the same projected (2D) atoms in all views. For this purpose, we first determine the topology of the structure (e.g. bonds and rings) in both atomistic models. Drawing the atomic network by hand is possible but rather tedious, so we developed an automatic assignment routine that appears to work well for sp^2-bonded carbon networks. Simply defining bonds to all neighbors within a certain distance becomes problematic in a projection with a tilted sample and irregular atomic distances (e.g. within defects). However, we found that a useful topology assignment can be made automatically if we require that each atom has no more than three bonds (optionally four) to nearest neighbors and we exclude the formation of triangles in the bonding network. This assumption agrees very well with the observations of the sp^2-bonded 2D structures presented in this work. A bond between two atoms is only created when both atoms are within the three closest neighbors (double-check criterion). If not, the next neighbor will be chosen as candidate and will be double-checked in the same way. Fig. 3.4 shows the network of the example data set (two views of a grain boundary) in the second column. Once all bonds are identified, the topological assignment continues with the identification of the rings created by the bonds. This is obtained by iterating through all neighbors of each atom. A polygon with n edges is found after $n-1$ iterations. The constraint of n is set depending of the maximum number of atoms within the largest ring, but it usually does not exceed $n = 9$ in graphene defects. The third column of Fig. 3.4 shows that every ring has been identified in the example data set. When all the rings are identified in both views, the algorithm continues with the assignment of the same rings in both views. This task starts with a characteristic atom sitting at the touching point of a pentagon, a heptagon and a hexagon in the first view. Then, the computer goes through the neighboring atoms via an outwards spiraling path that will cover all surrounding rings until the edge is hit. The same process is done for the second view, but the identical assignment (corresponding to the first view) is only achieved when the first characteristic atoms are the same. Therefore, the computer repeats the algorithm with all possible starting atoms and the longest match between the respective characteristic sequences of the polygons in the two views identifies the same starting atom. The connected rings and therefore the full information of the topology is shown in the last column of Fig. 3.4. When the assignment of the identical rings has been successful, the identification of the same atoms in the views is not difficult anymore. They are then iteratively identified by matching up all the touching polygons and already matched up neighbors. The identification of the same initial atom can only work automatically in the presence of a non-periodic feature in the lattice. If this is not the case, the starting atom has to be chosen manually.
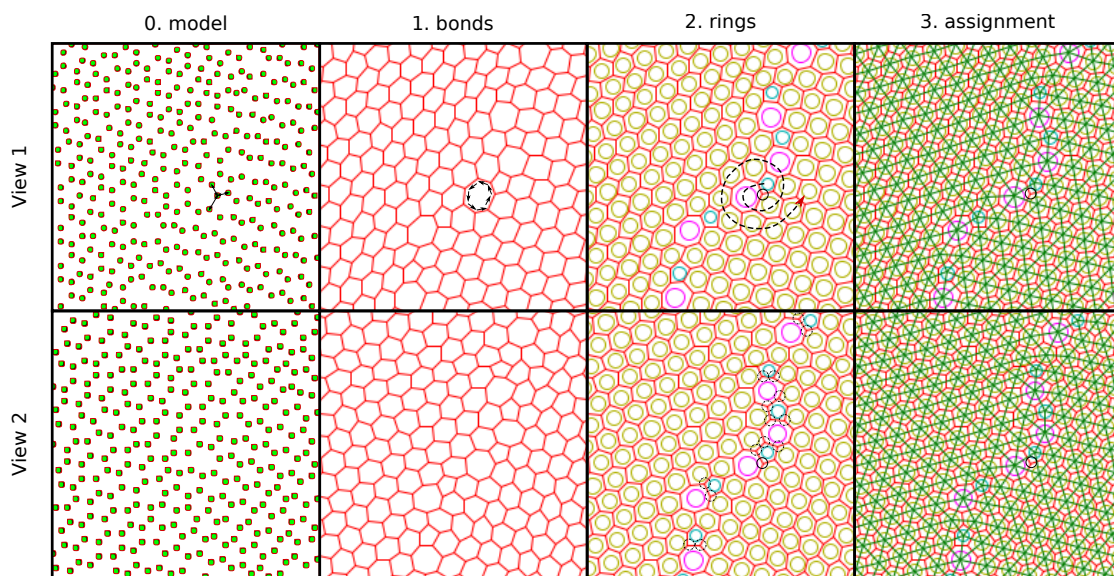
Figure 3.4: **Automatic assignment of the topology and identical atoms of the projections.** From left to right: 2D models of both views. By checking the nearest neighbors, the bonds can be identified resulting in the network of bonds. The path along the bonds can identify the rings. Starting at a characteristic atom, the rings can be assigned using a spiral path along the network. The same characteristic sequence defines the same starting atom. The right pictures show the connected rings with the same starting atom, where the identification of the same atom is trivial.

3.2.4 Determination of the 3D model

Last, but not least, we finish the reconstruction by extracting the 3D coordinates of all relevant atoms. First, we initialize a 3D model by including the atoms that exist in both projections and that are not at the edges of the 2D structures. For this purpose, we choose one of the 2D models (as obtained from one of the projections), and use it as the starting configuration with the third coordinate (z) initialized at zero. The projected positions $r_{calc}(x,y)_{p,i}$ of each 3D atom i can be calculated in each projection p. The 3D positions can now be optimized by minimizing the error function

$$\sigma_{3D} = \sum_p \sum_i (r_{calc}(x,y)_{p,i} - r_{2D}(x,y)_{p,i})^2 \tag{3.1}$$

where $r_{2D}(x,y)_{p,i}$ is the extracted 2D position of atom i in projection p. This means that each atom is shifted to the (x,y,z) coordinate where its projections are observed in the experiment. The optimization usually starts with matching the projection parameters (azimuth angle, scale) and shifting the atoms in z-direction alternately. This step drastically improves the match in the second view. Geometric smoothing at particular iterations helps to match a more realistic model to the projection parameters. Because the exact positions in the second view cannot be reached by only shifting the atoms in z-direction, a fine tune of the atomic positions by moving in all 3 dimensions finally converges the error function. It is to mention that this error function usually will not reach zero even after the fine tune due to the finite accuracy of the 2D models. Because a shift of the spatial coordinates always leads to shifts in both projection, there exists only a "best" solution (corresponding to the smallest error) for the coordinates of each atom.

Remarkably, the above function is sufficient when each atom is clearly identified in both projections. This holds for one atomic layer materials like graphene, as demonstrated in this thesis. If the condition of a fixed position in the projection has to be relaxed (e.g. when the extraction of the 2D positions is not possible), there is a slightly alternative approach the reconstruction can take: First, an initial model has to be defined (e.g. by computational analysis) as input. Then, the 3D structure is given by minimizing the difference between the simulated images and the experimental images. The approach is similar to the 2D reconstruction described in sec. 3.2.2, but now considering all views simultaneously. The error function is given by

$$\sigma_{3D} = \sum_p \sum_i (g(\mathbf{r})_{p,i} - V_{p,i})^2 \tag{3.2}$$

where $g(\mathbf{r})_{i,p}$ is the simulation of the model in projection p and $V_{p,i}$ is the pixel value of the i-th pixel of the experimental image of projection p. Fig. 3.5 shows the 3D model at different stages of the algorithm. Initially, the error is significantly higher in the second view than in the first view. This is expected because the first view was taken as initial x-y coordinates (and $z = 0$ for the initialized 3D model (i)). Note that there would be also a perfect match in the second view if the true structure would be flat. During optimization, the error decreases also in the second view (ii). The final structure is obtained when the error is negligible in both views (iii).
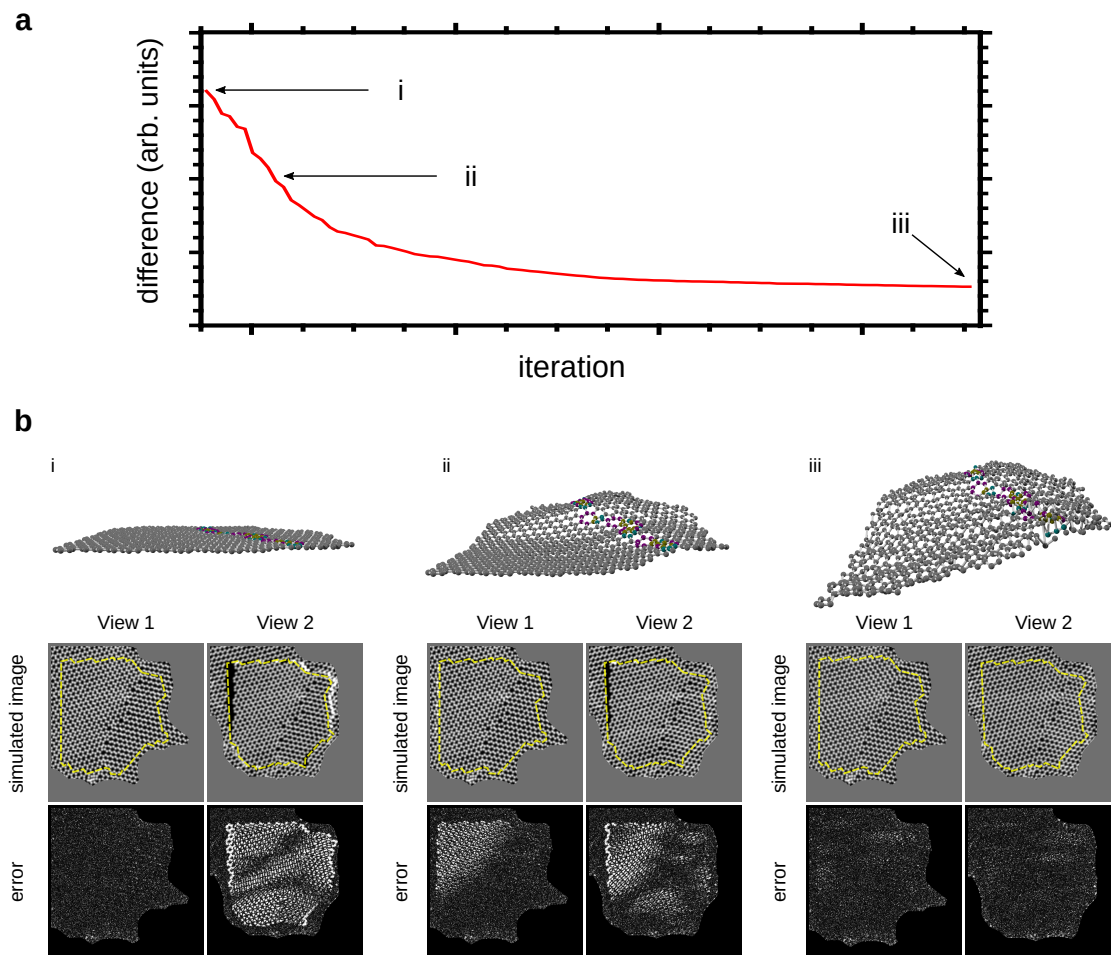
Figure 3.5: **3D reconstruction of a graphene grain boundary.** (a) Total error (see equation 3.1) as a function of iteration. (b) Perspective view (top), simulations (middle) and pixel by-pixel error (bottom) in both views in different iteration steps.

3.3 Source of errors

Several parameters define the error bars of the reconstruction. In this section, the accuracy of the 2D positions, the error caused by the limited tilt angle and the influence of the quality of the experimental data are discussed.

3.3.1 Accuracy of the 2D positions

The error in the determination of the 2D coordinates directly affects the noise in the 3D structure. To quantify how this affects the accuracy of the reconstruction, we have chosen a flat part of the test structure and calculated the standard deviation of the distribution of the bond lengths. This approach slightly overestimates the error because the region is not perfectly flat. For a typical electron dose used to obtain an atomically resolved image, we obtain a standard deviation of $\sigma = 5 \, \text{pm}$ (cf. Fig. 3.6a). The value depends mainly on the signal-to-noise ratio of the experimental images.

3.3.2 Tilt angle

The error in out-of-plane direction is magnified by a factor of $1/tan(\alpha)$, where α is the relative tilt angle between the projections. The trend of the error as a function of tilt angle is shown in Fig. 3.6b. With the measured in-plane error of 5 pm, the corresponding out-of-plane error is estimated to be 0.14 Å . Although a higher tilt angle increases the accuracy, several challenges have to be encountered: Firstly, the tilting range of the microscope goniometer is limited by geometrical constraints due to the short distance between the pole piece of the objective lens and the specimen stage. Secondly, the signal-to-noise ratio decreases with higher tilt angle as a result of out-of-plane vibrations of the individual atoms. The frequency of the vibrations is orders of magnitude higher than the time required for one scan resulting in a smearing orthogonal to the tilting direction. Last, but not least, the projected distances are also reduced which might inhibit resolving two neighboring atoms and therefore the identification of each individual atom. The precision of the mechanical tilt is 0.5 mrad [72] which also contributes to the limited accuracy of the reconstruction.

3.3.3 Quality of the experimental images

Obviously, the noise level of the reconstruction is directly related to the quality (e.g. signal-to-noise ratio, aberrations, disturbances) of the experimental data. While the influence of the signal-to-noise ratio is already discussed and aberrations are taken into account in the reconstruction algorithm, disturbances such as scan distortions or sample drift can lead to artifacts in the reconstruction. Although state-of-the-art specimen stages minimize the stage drift, a linear stage drift corresponds to a rhombohedral (instead of a rectangular) scan pattern. This artifact can be corrected using a matrix that corrects the distortion in the corresponding view. Unfortunately, distortions resulting in line-by-line variations are more challenging to correct as shown in Fig. 3.6c, highlighted by the yellow dashed box. The line-by-line variations origins are from disturbances with a timescale corresponding to the slow scan direction (red arrow), which is in the millisecond

region. This distortion results in an artifact which can be identified by small (non-physical) elongations in the reconstruction along the slow scan direction. As a consequence, it is important to orient the scan pattern so that the fast scan direction probes the height variation of interest, in this case the grain boundary.

3.4 Analysis of electron-driven dynamics

Tilting the specimen does not only reveal the 3D structure of the object of interest, but also allows to study out-of-plane dynamics by capturing a sequence of STEM images. In order to visualize different configurations of (multiple) metastable states, the energy barriers have to be relatively close to the maximum transferred energy. If the energy barrier is too large, the structure modification cannot be triggered. In the case of a too small energy barrier between the states, the timescales of the changes are orders of magnitude faster than the time of an acquisition resulting in a superposition of multiple configurations in the final STEM image. For example, pyramidal inversions of Si in graphene are observed as described in Paper 2. The energy barrier can be experimentally estimated by analyzing the dose (electrons per area) until the corresponding event happens. The dose is estimated by

$$dose = \frac{I}{e} \cdot \frac{t}{A}$$

,where I is the beam current at the sample, e is the elementary charge, t is the time for one scan and A is the area of the field of view. The statistical distribution of the events is usually underlying a Poisson distribution. Thus, the probability to find k events in a given time interval follows

$$f_\lambda(k) = \frac{\lambda^k}{k!}e^{-\lambda}$$

where the fitted parameter λ is the expectation value of the process. The cross section of the event can be then estimated and compared with the theoretical cross section.
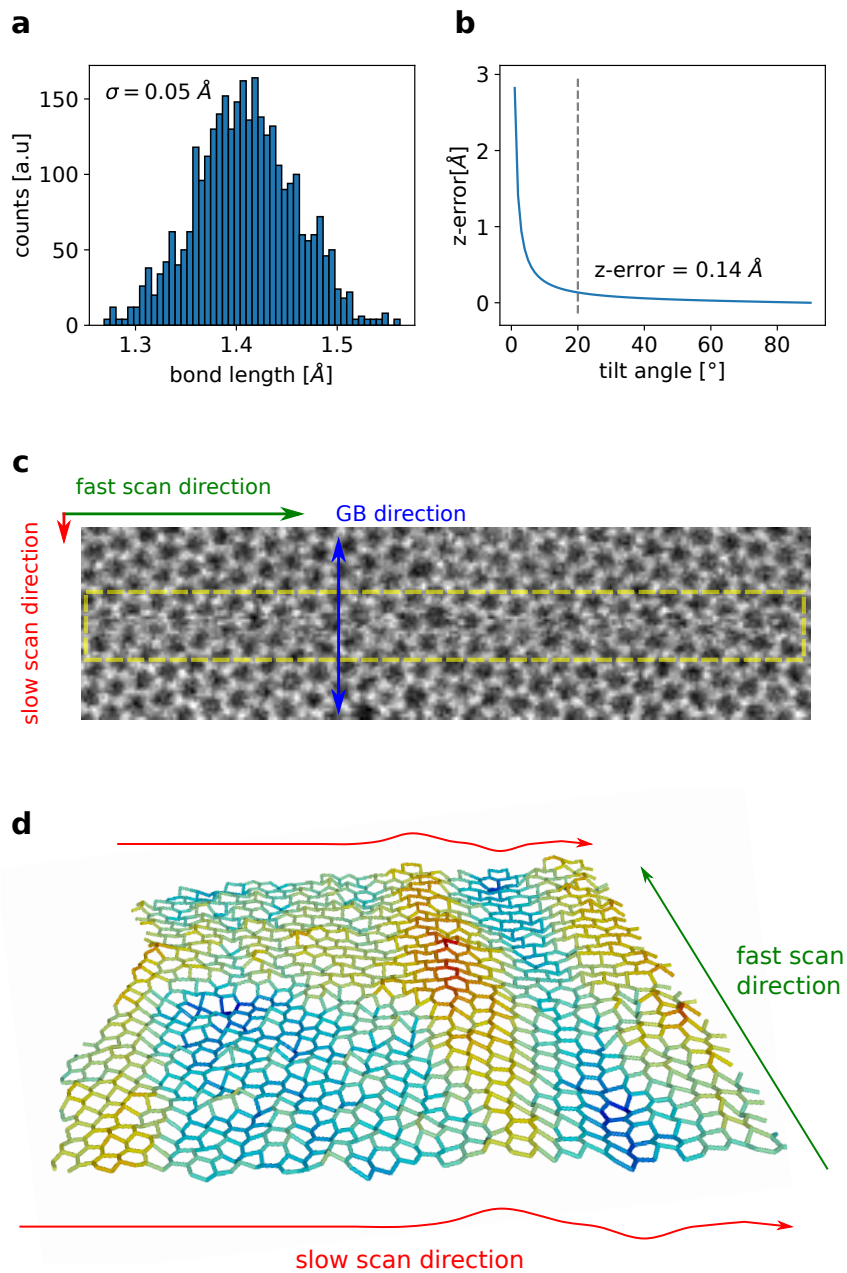
a

b

c

d

Figure 3.6: **Analysis of the errors.** (a) Distribution of bond lengths of the optimized GB. (b) Expected error as function of tilt angle. (c) STEM image of a graphene GB with a scan distortion between the two dashed yellow lines. (d) Perspective view of the reconstruction of the same GB showing the elongations due to the scan distortion.

<div style="text-align: right; font-size: 3em; color: #cccccc;">**4**</div>

Results

4.1 Paper I

Paper I is the core of this thesis: Here, the authors present the novel method also presented in detail in chapter 3 of this thesis. It analyzes the reliability and errors of the method by comparing the reconstruction with a computationally obtained structure. Applying the reconstruction to a set of graphene GBs reveals – for the first time – very interesting deformation tendencies along the line defect which are correlated with the misorientation angles. In fact, the trend of deformations along the grain boundaries as discussed in chapter 2.2 is observed. The results of this paper give new insights into the 3D structure of defects in graphene.

Author contributions

The author of this thesis developed the reconstruction algorithm, performed the sample preparation, STEM measurements, applied the reconstruction, analyzed the structures and drafted the figures and the manuscript. C.K. participated in the development of the algorithm. M.R.A.M. performed the MD simulations. C.M. prepared alignments for the STEM instrument and supported the experiments. A.M. participated in the development of the algorithm. G.A. participated in the STEM experiments and sample preparation. J.K. and J.C.M conceived and supervised the study.

PAPER • OPEN ACCESS

Revealing the 3D structure of graphene defects

View the article online for updates and enhancements.

2D Materials

PAPER

Revealing the 3D structure of graphene defects

Christoph Hofer [iD], Christian Kramberger [iD], Mohammad Reza Ahmadpour Monazam, Clemens Mangler, Andreas Mittelberger [iD], Giacomo Argentero, Jani Kotakoski [iD] and Jannik C Meyer[1] [iD]

Faculty of Physics, University of Vienna, Boltzmanngasse 5, A-1090, Vienna, Austria
[1] Author to whom any correspondence should be addressed.

E-mail: christoph.hofer@univie.ac.at and jannik.meyer@uni-tuebingen.de

Abstract

We demonstrate insights into the three-dimensional (3D) structure of defects in graphene, in particular grain boundaries, obtained via a new approach using two transmission electron microscopy images recorded at different angles. The structure is revealed through an optimization process where both the atomic positions as well as the simulated imaging parameters are iteratively changed until the best possible match to the experimental images is found. We first demonstrate that this method works using an embedded defect in graphene that allows direct comparison to the computationally predicted 3D shape. We then apply the method to a set of grain boundary structures with misorientation angles spanning nearly the whole available range (2.6°–29.8°). The measured height variations at the boundaries reveal a strong correlation with the misorientation angle with lower angles resulting in stronger corrugation and larger kink angles. Our results allow for the first time a direct comparison to theoretical predictions for the corrugation at grain boundaries, revealing the measured kink angles are significantly smaller than the largest predicted ones.

Identifying the position of every atom in a sample is the ultimate goal of structural characterization. Although transmission electron microscopy (TEM) has already reached the spatial resolution to allow resolving all atomic distances [1, 2], it only provides two-dimensional (2D) projections of the sample regardless of its actual three-dimensional (3D) shape. While computer tomography can retrieve the 3D structure from a set of 2D projections, down to atomic resolution [3–7], it requires high electron doses which is problematic for structures susceptible to electron-beam-induced structural changes. This is because in absence of any additional information, the number of projections required to obtain a uniform resolution in all dimensions is approximately the sample size divided by the resolution [8], which reaches typically tens or hundreds of projections for bulk samples.

Defects in graphene, the 2D allotrope of carbon, are expected to corrugate the structure. Such corrugations have been studied previously through simulations [9–12] and their existence has also been indirectly inferred from high-resolution TEM images [13, 14]. However, since graphene defects frequently change their configuration under electron irradiation even at moderate acceleration voltages [15–20], recording an entire tomographic series to image the 3D structure of graphene defects at atomic resolution would be very challenging. The 3D structure of defect free graphene has been analyzed on the basis of a defocus series [21] and the structure of clustered divacancies has been extracted from atom contrast variations in a single image [22]. However, this approach requires that the intensity of each atom can be measured without being affected in any way by the intensity of the neighboring atoms, which is difficult to avoid in presence of residual aberrations, finite resolution, and very short projected distances in non-flat structures. The polynomial fit of the atom positions as done in [22], relaxes this requirement, but then it also does not reveal the position of individual atoms, but only averages of local height. In this way, it is not suited for the analysis of structures with sharp kinks or significant height differences between neighboring atoms, as revealed in this work. Our approach does not introduce such geometrical constraints and the results show that indeed the 3D configurations are more complex than the smooth height variations around defects that could be revealed previously.

Here, we show that it is possible to obtain the 3D shape of defected graphene directly already from two experimental images obtained at different tilt angles.

We first demonstrate our approach with an embedded graphene defect, for which the corrugated structure obtained from the experimental data can be directly compared with the one obtained computationally through energy optimization. Then, we move on to study the corrugations caused by grain boundaries in polycrystalline graphene. Importantly, both grain boundaries themselves as well as corrugations even in the absence of defects have been shown to significantly influence the properties of graphene [23, 24], making this an important subject to study.

We start our experiment by looking for a defect in graphene grown via chemical vapor deposition (CVD; see Methods for details) using scanning transmission electron microscopy (STEM) medium-angle annular dark field (MAADF) imaging. In order to avoid electron irradiation-induced changes in the atomic structure [25], the electron dose at the defect is minimized by recording as few atomic-resolution images as possible of the area of interest. After a defect is found and one atomic resolution image is acquired, we record a few images of the surrounding area at larger fields of view in order to find the same location after the sample has been tilted. While tilting, we track the sample to stay in the vicinity of the defect, and when the necessary tilt angle has been reached, we zoom in again and record the second atomic-resolution exposure. Even with this approach, the atomic structure at the defect often changes between the two recorded atomic-resolution images. However, it is also possible to obtain pairs of images of defect structures where the atomic structure remained unchanged. Areas covered by contamination in each image have been masked in order not to confuse the reconstruction algorithm and the images have been high-pass filtered. An example is shown in figure 1.

The first task for our reconstruction algorithm is the identification of individual atoms within each of the experimental images. This is achieved through an iterative process, where a model structure is compared at each step with the experimental image through image simulation (see Methods). Initially, the model contains no atoms. At each step, an atom is either added, its position is adjusted, or it is removed from the model. This is carried out by selecting a random position and either adding an atom at this position, or if there is an atom within a distance of $r_{cut} \leqslant 0.5$ Å moving it to this position. If two atoms end up being too close to each other (within $r_{nbr} \leqslant 1$ Å), the atom pair is replaced by just one atom. After each adjustment, a simulated STEM-MAADF image is created based on the model, and the difference between the simulated image and the experimental image is calculated as $\sigma = \sum_{i=1}^{N} (I_i^{exp} - I_i^{sim})^2$, where the sum runs over all N pixels in the image, and I_i^{exp} and I_i^{sim} are the intensities of pixel i in the experimental and the simulated image, respectively. At each step, the change in the structure is only accepted if it results in reducing σ from the previous step. Since the match between the

experimental and the simulated images depends not only on the exact atomic structure but also on the exact electron aberrations during the experiment (which can change between two images and need to be used as input parameters for the image simulation), they are also adjusted with a similar stochastic process. An image sequence showing one optimization process is presented in the supplemental material (video 1) and the evolution of σ as a function of the number of steps is shown in figure 2. At the end of the optimization process, σ approaches a value close to zero and the difference image is dominated by noise.

Next, the topology needs to be established in order to allow identifying the same atom in each of the model structures. In our approach, this process is automated through the implementation of the following rules. Firstly, two neighboring atoms need to be close enough (within 2 Å) to allow bonding. Secondly, no more than three neighbours are allowed for each individual atom. Finally, the formation of three-membered carbon rings is prohibited. These rules are based on the observation of previous atomic-resolution studies of the structure of sp^2-bonded defective carbon networks [15, 26] and appear to work extremely well. The agreement is easily confirmed visually by comparing the experimental image to the established network (see figure 2(c)). Subsequently, identifying the same atoms in each of the images is possible based on their location in the network.

After the atoms have been identified, those that appear in both images (excluding image edges) are used as the basis for a new model which will be further optimized, now including also the third dimension. One of the 2D models is chosen arbitrarily for the initial positions of the atoms, and the optimization is continued considering both experimental views simultaneously (taking into account the tilt between the models). During this phase atoms are no longer added or removed. Initially, the optimization takes only into account the model structures, minimizing the difference between the projected positions of the new 3D model and those of the 2D models developed during the previous optimization phase. After this process has converged (see figure 3(a)), the optimization is continued based on the error in simulated STEM-MAADF images as compared to the experimental ones. The convergence behavior of this optimization phase is shown in figure 3(b). The model structures, simulated STEM-MAADF images and the error with respect to the experimental images are shown at three different stages of the process in figure 3(c). The yellow dashed line shows the area which is included in the model (edge atoms are excluded, but retained as background in the simulated image so that no discontinuity appears at the edge). As expected, the simulation of the first (untilted) model (View 1 in figure 3(c)) fits perfectly to the corresponding experimental image (this was the starting configuration), but there is a high discrepancy between the experimental image and the simulation of the second (tilted)
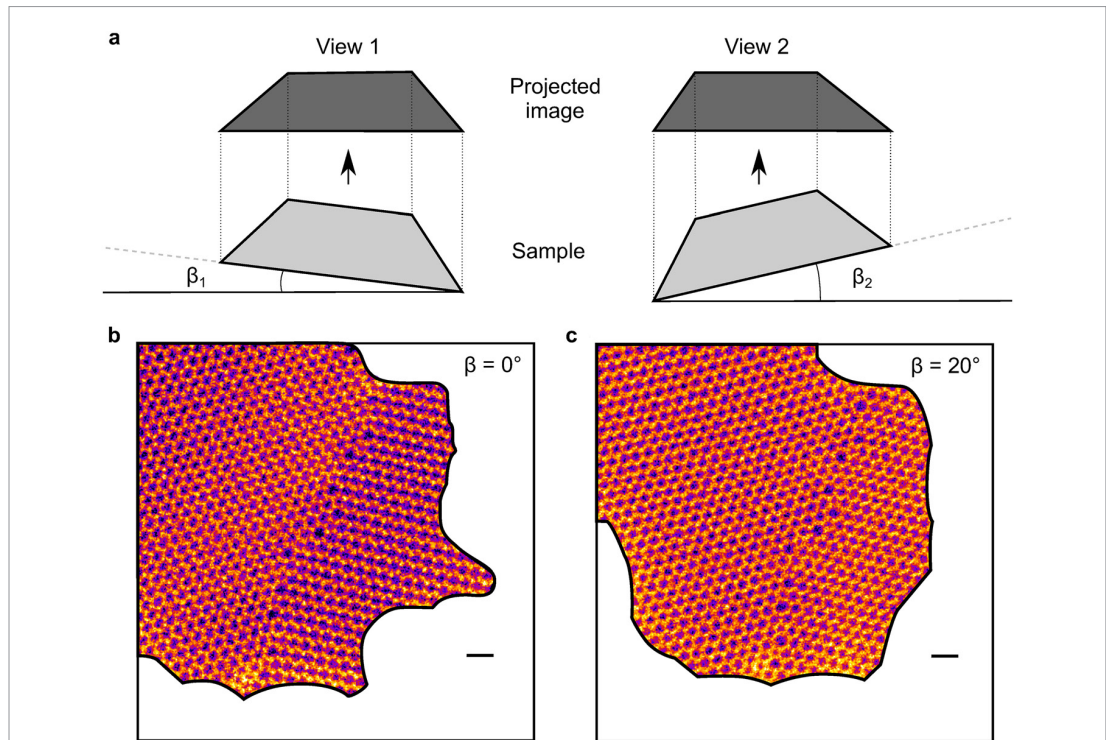
Figure 1. (a) Schematic illustration showing the sample at two different tilts (β_1 and β_2) that result in two different views of the sample (View 1 and View 2). (b) Filtered STEM-MAADF image of a graphene grain boundary at nominally zero sample tilt ($\beta = 0°$). (c) STEM-MAADF image of the same grain boundary at a nominal tilt of ca. $\beta = 20°$. The white areas correspond to contaminated areas that have been cut out from the images. Scale bars are 0.5 nm. The experimental images have been processed with a high pass filter to remove long-range intensity variations. Raw images are shown in the supplementary information (stacks. iop.org/TDM/5/045029/mmedia).
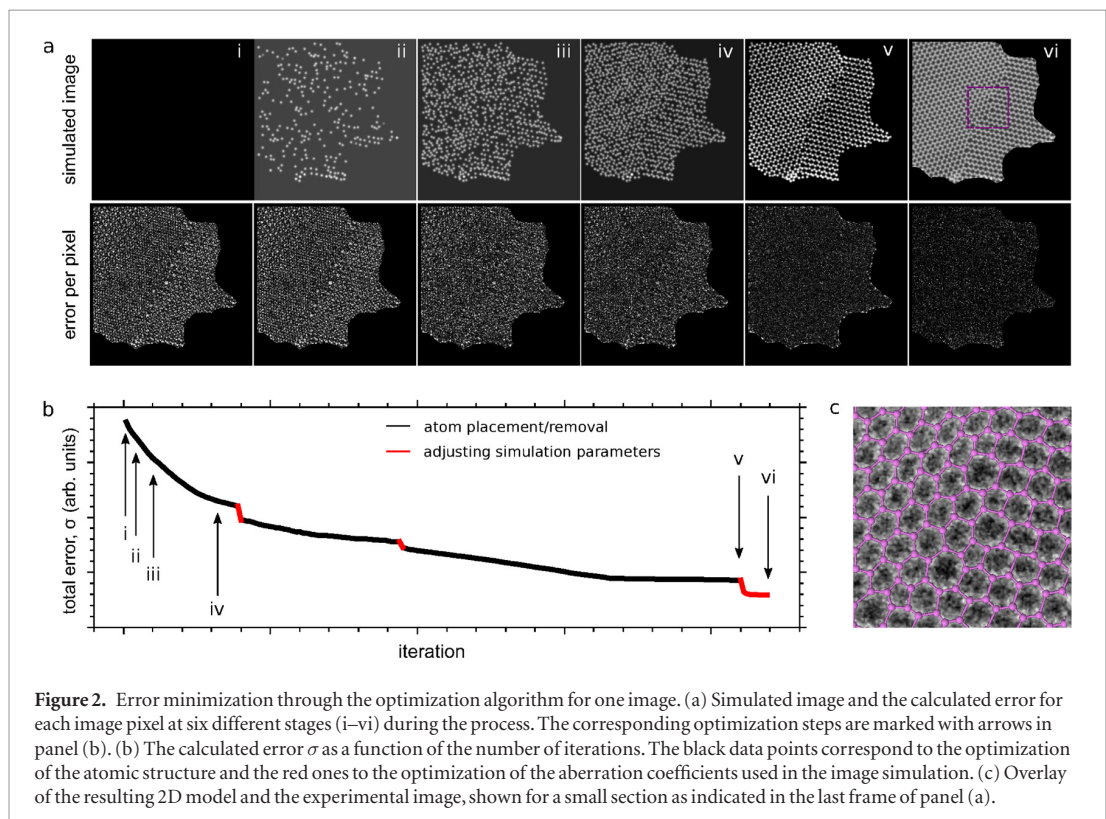
Figure 2. Error minimization through the optimization algorithm for one image. (a) Simulated image and the calculated error for each image pixel at six different stages (i–vi) during the process. The corresponding optimization steps are marked with arrows in panel (b). (b) The calculated error σ as a function of the number of iterations. The black data points correspond to the optimization of the atomic structure and the red ones to the optimization of the aberration coefficients used in the image simulation. (c) Overlay of the resulting 2D model and the experimental image, shown for a small section as indicated in the last frame of panel (a).

Figure 3. Evolution during the 3D optimization. (a) Difference between the projected atomic positions of the optimized 3D model and those in the flat models obtained during the previous optimization step. (b) Total error in the simulated STEM-MAADF images based on the 3D model, as compared to the experimental images. (c) Perspective views of the atomic structures (atoms of non-hexagonal rings in the grain boundary highlighted by color), simulated STEM-MAADF images for both tilt angles (View 1 and View 2), and the error for each pixel as compared to the experimental images. The area included in the 3D optimization is marked by the yellow dashed lines overlaid on the simulated images. The corresponding iteration steps for each case (i–iii) are marked in panels (a) and (b).

model (View 2). The situation improves quickly during the optimization process until at the end the difference between the experimental images and the simulated ones is dominated by noise.

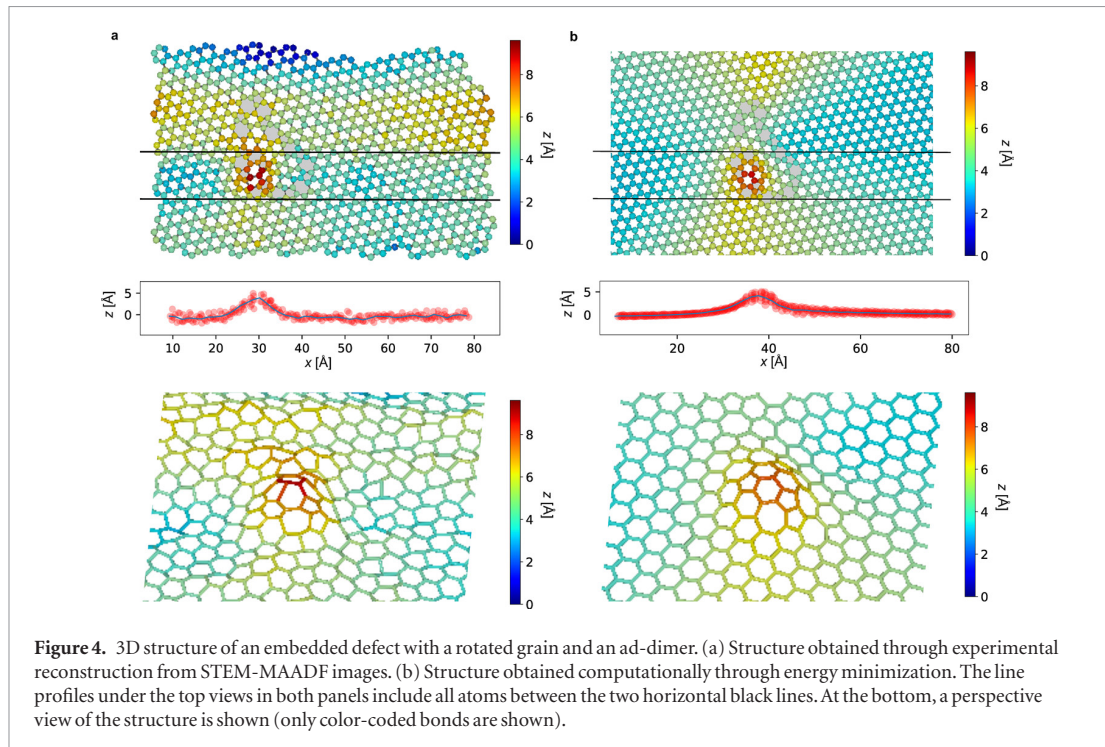In order to validate our approach and estimate its accuracy, we test it using a computationally obtained structure and simulated STEM images for realistic conditions including noise as expected for our experimental dose. For this purpose, we use a defect configuration that was also observed experimentally, but with its 3D configuration obtained by energy minimization (see Methods). Since this defect contains two extra atoms compared to an ideal graphene lattice, it displays a significant out of plane distortion and hence is ideally suited for the validation. The reconstruction from the simulated data agrees with the original model with a mean out-of-plane deviation of 0.183 Å and a mean in-plane deviation of 0.053 Å. Details of this test are given in the supplementary information. As expected, the out-of-plane error is larger than the in-plane error, since the effect of noise is amplified by the limited tilt angle between the two images.

Next, we use the two experimentally obtained STEM images of this structure. Figure 4 shows the experimental reconstruction (a) and for comparison the energy-minimized structure (b). Top views, line profiles and the side views show and excellent match between the two. The structure displays a particularly strong

distortion around the two atoms that are furthest from the plane, and which can be identified as a carbon ad-dimer integrated into the defect. Additionally, we tested our method with a small rotated grain (flower defect [27, 28]), which is flat according to both, computational analysis (energy minimization) and 3D reconstruction from experimental data. For the latter structure, we could also calculate the out-of-plane standard deviation of the coordinates. In this case, the deviation is 0.31 Å, which is slightly higher than the error obtained from the simulated data as discussed above.

After establishing the reliability of the method for resolving the 3D structure, we move onto the analysis of graphene grain boundaries. GBs are a challenge for computational techniques, because they join together two crystalline grains with different orientations, hence they can neither trivially be incorporated into a periodic supercell required for most computational techniques nor can their effect on the surrounding graphene lattice be easily estimated with calculations using non-periodic structures since often only a short piece of a GB is visible in atomic resolution images. We present results for several GBs spanning misorientation angles $\theta \in [2°, 30°]$. In figure 5, the 3D structure of two representative grain boundaries with small misorientation angles ($\theta = 2°$ and $\theta = 8°$, respectively) and in figure 6, the 3D structure of two representative grain boundaries with large misorientation

Figure 4. 3D structure of an embedded defect with a rotated grain and an ad-dimer. (a) Structure obtained through experimental reconstruction from STEM-MAADF images. (b) Structure obtained computationally through energy minimization. The line profiles under the top views in both panels include all atoms between the two horizontal black lines. At the bottom, a perspective view of the structure is shown (only color-coded bonds are shown).
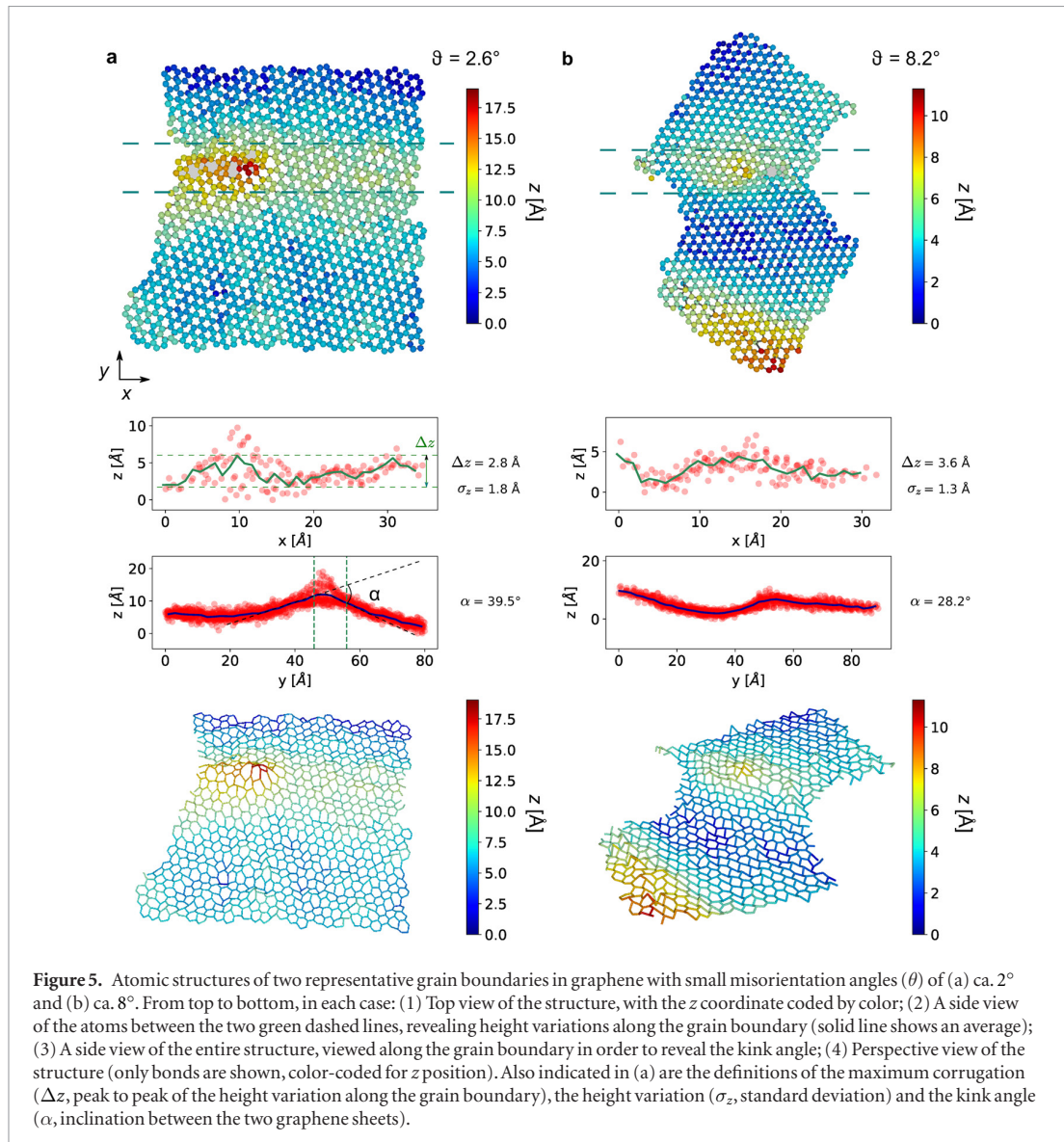
angles ($\theta = 24°$ and $\theta = 30°$, respectively) are shown. Three additional structures can be found in the supplementary information. For each structure, we show the top view colored based on the z-coordinate of each atom as well as two line profiles: one along the y-axis that contains all atoms in the structure and another along the x-axis that is limited to a narrow strip of atoms located within ca. 1 nm around the GB. From the line profiles, we also calculate the maximum corrugation (Δz), height variation (σ_z), defined as the standard deviation of the out-of-plane coordinate of the atoms in the structure from the mean value and the kink angle (α) which is measured across the grain boundary. For an optical impression of the structure, we also show a perspective view of the bonds with the same color code as in the top view.

When each of the structural characteristics are plotted as a function of the misorientation angle (θ) (figure 7), it becomes clear that they all depend strongly on θ. While the trend is most clear for the small- and high-angle grain boundaries, the intermediate data points display some scatter reflecting the large structural variability in these grain boundaries. Remarkably, the lowest measured kink angle is only $\alpha \approx 0.7°$ for a GB with $\theta \approx 30°$, whereas the highest one is nearly 40° for a GB with $\theta \approx 2.6°$. This variation is lower than what has been predicted based on density functional tight binding calculations [29]; the largest calculated angles were up to 85° with no clear correlation to the misorientation angle. This discrepancy is likely a consequence of the fact that the theoretical models were created by forcing two straight graphene edges to join, whereas during actual growth nothing prevents the carbon atoms from forming more meandering structures [20, 30–32] that help in reducing the

stress at the GB. In another theoretical work [9], it was predicted that small angle grain boundaries should show a pronounced tendency for buckling, whereas large angle grain boundaries tend to be flat. Although also this work was limited to straight GBs (and also formed of regular arrays of dislocations), this prediction is in good agreement with our experimental result. We indeed find that smaller θ predicts higher corrugation (up to $\Delta z \approx 4$ Å and $\sigma_z \approx 1.8$ Å), whereas the GBs with $\theta \sim 30°$ tend to be significantly flatter (with $\Delta z \approx 1.5$ Å and $\sigma_z \approx 0.5$ Å). These values reflect the fact that small-angle GBs contain isolated non-hexagonal rings as well as short segments where the hexagonal lattices of both grains are directly connected, leading to significant local strain that must be released through buckling [9, 33]. This is particularly clear in figure 5(a), where an essentially isolated dislocation core in a grain boundary with only 2.6° misorientation angle is observed.

In conclusion, we have demonstrated a new approach to determine the 3D structure of defective graphene at the atomic resolution from only two scanning transmission electron microscopy images taken at different sample tilts (with a respective difference of ca. 20°). We first showed an embedded defect for which the results could be directly compared to the structure obtained through energy minimization. The comparison revealed excellent agreement, except for small local height variations due to noise in the experimentally obtained structure. We then applied the method to a set of grain boundary structures with misorientation angles nearly spanning the whole available range (2.6°–29.8°). The measured height variations at the boundaries reveal a strong correlation with the misorientation angle with lower angles resulting in

Figure 5. Atomic structures of two representative grain boundaries in graphene with small misorientation angles (θ) of (a) ca. 2° and (b) ca. 8°. From top to bottom, in each case: (1) Top view of the structure, with the *z* coordinate coded by color; (2) A side view of the atoms between the two green dashed lines, revealing height variations along the grain boundary (solid line shows an average); (3) A side view of the entire structure, viewed along the grain boundary in order to reveal the kink angle; (4) Perspective view of the structure (only bonds are shown, color-coded for *z* position). Also indicated in (a) are the definitions of the maximum corrugation (Δz, peak to peak of the height variation along the grain boundary), the height variation (σ_z, standard deviation) and the kink angle (α, inclination between the two graphene sheets).

stronger corrugation and larger kink angle (slope difference for the graphene grains on the different sides of the boundary). The largest measured kink angle was almost 40° for a GB with 2.6° misorientation. As far as we know, our results allow for the first time a direct comparison with theoretical predictions for the corrugation at grain boundaries. The measured kink angles are significantly smaller than the largest predicted ones [29], probably due to artificial constraints in the theoretical models being different from the experimental reality. However, our results do qualitatively agree with the prediction that smaller misorientation leads to higher overall corrugation at the boundary [9]. Our results both open the way towards a detailed study of the complete morphology of 2D materials, including the often disregarded third dimension, and can already be used for tailoring graphene growth towards application utilizing the revealed differences in corrugations of polycrystalline samples with different misorientation angles between the graphene grains.
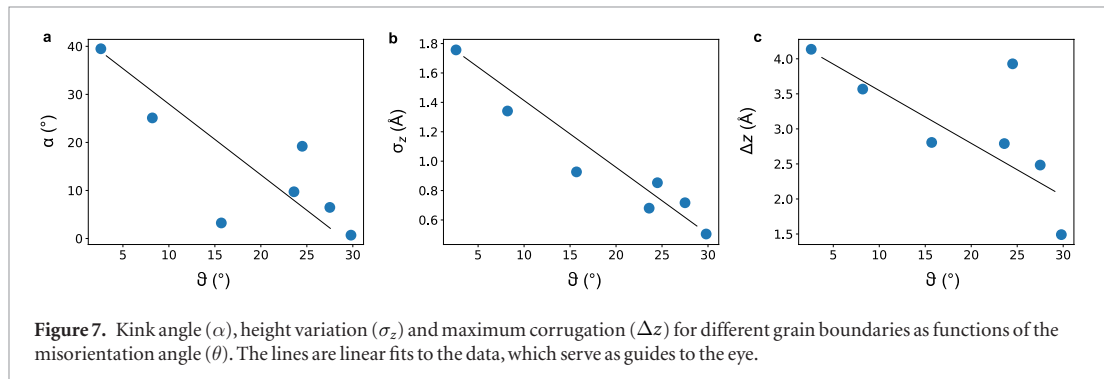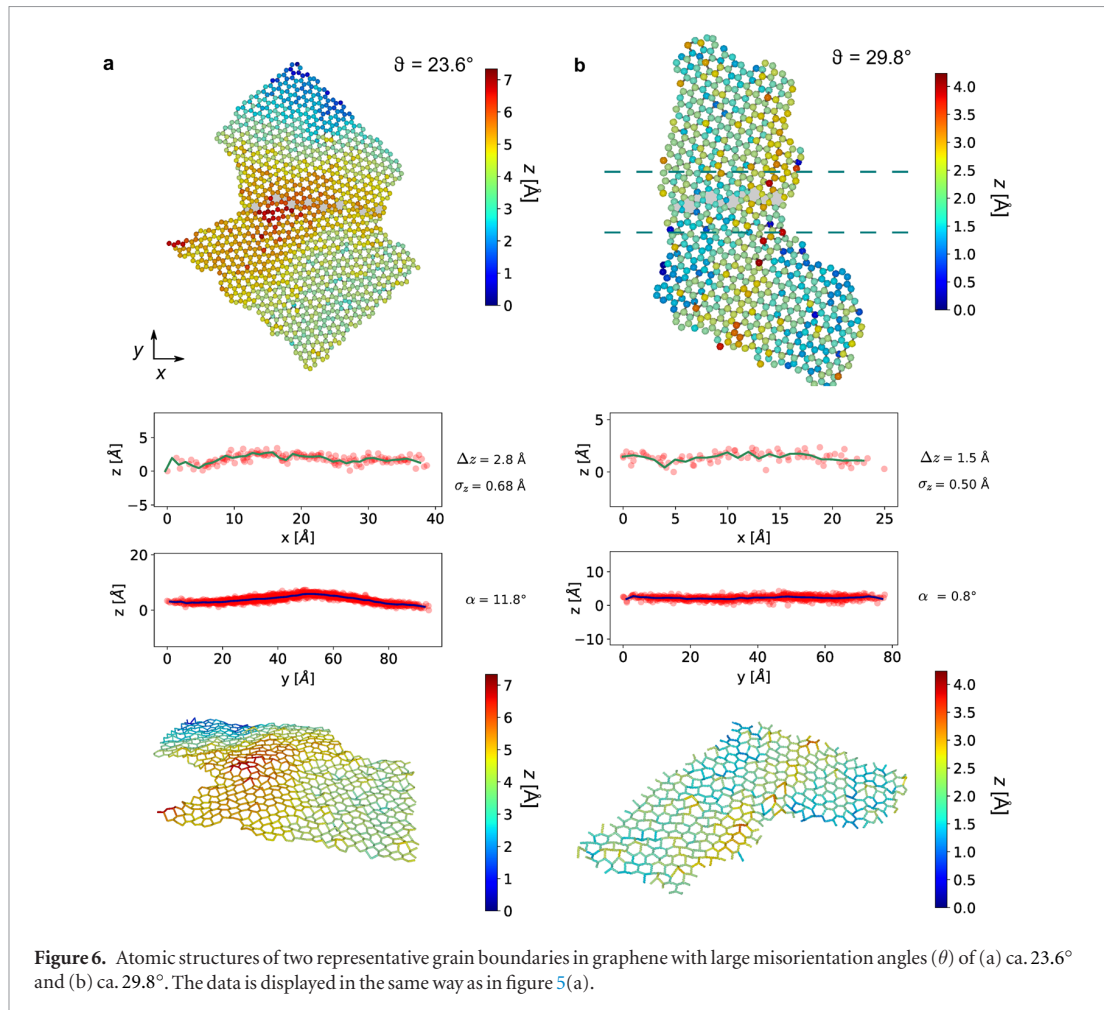
Methods

Samples

For our experiments, we studied chemical vapor deposition (CVD) grown graphene. We used commercially available graphene on TEM grids (Graphenea on Quantifoil R2/4), as well as self-grown CVD samples transferred to Quantifoil 0.6/1 grids. In order to have a high defect density in our samples, we kept the growth temperature low ($T = 960$ °C), the flow rate high ($S_F = 100$ sccm) and the annealing time as short as possible by starting the growth when the growth temperature is reached. As precursor, we used ethane which further increases the nucleation density.

Microscopy

Scanning transmission electron microscopy (STEM) experiments were conducted using a Nion UltraSTEM100, operated at 60 kV acceleration voltage. Typically, our atomic-resolution images were recorded

Figure 6. Atomic structures of two representative grain boundaries in graphene with large misorientation angles (θ) of (a) ca. 23.6° and (b) ca. 29.8°. The data is displayed in the same way as in figure 5(a).

Figure 7. Kink angle (α), height variation (σ_z) and maximum corrugation (Δz) for different grain boundaries as functions of the misorientation angle (θ). The lines are linear fits to the data, which serve as guides to the eye.

with 512×512 pixels for a field of view of 8 nm and dwell time of 32 μs per pixel using the medium angle annular dark field (MAADF) detector.

Conjugate gradient energy minimization

In order to study the strain adaptation in each of the defects, a supercell of pristine graphene with the size of 72×62 nm^2 consisting of 173 000 atoms was created and the defect structure was incorporated into this supercell. LCBOP [34] was used as the long-range bond-order potential for carbon to describe the pair interactions. All calculations were performed with Large-scale Atomic/Molecular Massively Parallel Simulator code [35, 36]. The total potential energy was minimized by relaxing

atoms until the forces were below 10^{-3} eV Å^{-1} and the strain at the borders of the graphene flake was negligible (pressure below 1 atmosphere).

STEM image simulation

Instead of a multislice algorithm, which is typically used for quantitative STEM-simulations, we used a simplified method which works for single layer materials and is much faster. We approximate the potential of the 2D lattice by a zero-filled image with non-zero pixel values on the atomic positions. The simulation is obtained by convoluting this image with a (potentially aberrated) electron probe (see supplementary information for more details).

Acknowledgments

Supporting information

The Supporting Information contains details of the STEM simulation method, additional analysis of the 3D accuracy, additional grain boundary models and a complete set of raw and processed images. Koch–Kirkland [37, 38] are cited in the supplement.

ORCID iDs

Christoph Hofer ⓘ https://orcid.org/0000-0002-0844-8366
Christian Kramberger ⓘ https://orcid.org/0000-0002-2772-3765
Andreas Mittelberger ⓘ https://orcid.org/0000-0001-9267-5184
Jani Kotakoski ⓘ https://orcid.org/0000-0002-1301-5266
Jannik C Meyer ⓘ http://orcid.org/0000-0003-4023-0778

References

[1] Colliex C 2014 Seeing and measuring with electrons: transmission electron microscopy today and tomorrow an introduction *C. R. Phys.* **15** 101–9

[2] Krivanek O, Dellby N and Lupini A 1999 Towards sub-Å electron beams *Ultramicroscopy* **78** 1–11

[3] Bals S, Goris B, Altantzis T, Heidari H, Van Aert S and Van Tendeloo G 2014 Seeing and measuring in 3D with electrons *C. R. Phys.* **15** 140–50

[4] Miao J, Ercius P and Billinge S J L 2016 Atomic electron tomography: 3D structures without crystals *Science* **353** aaf2157

[5] Weyland M and Midgley P A 2004 Electron tomography *Mater. Today* **7** 32–40

[6] Xu R *et al* 2015 Three-dimensional coordinates of individual atoms in materials revealed by electron tomography *Nat. Mater.* **14** 1099–103

[7] Yang Y *et al* 2017 Deciphering chemical order/disorder, material properties at the single-atom level *Nature* **542** 75–9

[8] Kak A C and Slaney M 1988 IEEE engineering in medicine and biology society *Principles of Computerized Tomographic Imaging* (New York: IEEE Press)

[9] Yazyev O V and Louie S G 2010 Topological defects in graphene: dislocations and grain boundaries *Phys. Rev.* B **81** 1–7

[10] Liu T-H, Gajewski G, Pao C-W and Chang C-C 2011 Structure, energy, and structural transformations of graphene grain boundaries from atomistic simulations *Carbon* **49** 2306–17

[11] Kotakoski J, Eder F R and Meyer J C 2014 Atomic structure and energetics of large vacancies in graphene *Phys. Rev.* B **89** 201406

[12] Shekhawat A and Ritchie R O 2016 Toughness and strength of nanocrystalline graphene *Nat. Commun.* **7** 10546

[13] Warner J H, Fan Y, Robertson A W, He K, Yoon E and Lee G D 2013 Rippling graphene at the nanoscale through dislocation addition *Nano Lett.* **13** 4937–44

[14] Lehtinen O, Vats N, Algara-Siller G, Knyrim P and Kaiser U 2015 Implantation and atomic-scale investigation of self-interstitials in graphene *Nano Lett.* **15** 235–41

[15] Kotakoski J, Krasheninnikov A V, Kaiser U and Meyer J C 2011 From point defects in graphene to two-dimensional amorphous carbon *Phys. Rev. Lett.* **106** 105505

[16] Meyer J C *et al* 2012 Accurate measurement of electron beam induced displacement cross sections for single-layer graphene *Phys. Rev. Lett.* **108** 196102

[17] Susi T, Hofer C, Argentero G, Leuthner G T, Pennycook T J, Mangler C, Meyer J C and Kotakoski J 2016 Isotope analysis in the transmission electron microscope *Nat. Commun.* **7** 13040

[18] Kotakoski J, Mangler C and Meyer J C 2014 Imaging atomic-level random walk of a point defect in graphene *Nat. Commun.* **5** 3991

[19] Susi T *et al* 2014 Silicon–carbon bond inversions driven by 60 keV electrons in graphene *Phys. Rev. Lett.* **113** 115501

[20] Kurasch S, Kotakoski J, Lehtinen O, Skakalova V, Smet J, Krill C E, Krasheninnikov A V and Kaiser U 2012 Atom-by-atom observation of grain boundary migration in graphene *Nano Lett.* **12** 3168–73

[21] Dyck D V, Jinschek J R and Chen F-R 2012 'Big Bang' tomography as a new route to atomic-resolution electron tomography *Nature* **486** 243–6

[22] Chen L-G, Warner J, Kirkland A I, Chen F-R and Van Dyck D 2017 Snapshot 3D electron imaging of structural dynamics *Sci. Rep.* **7** 10839

[23] Rossi A, Piccinin S, Pellegrini V, de Gironcoli S and Tozzini V 2015 Nano-scale corrugations in graphene: a density functional theory study of structure, electronic properties and hydrogenation *J. Phys. Chem.* C **119** 7900–10

[24] Atanasov V and Saxena A 2010 Tuning the electronic properties of corrugated graphene: confinement, curvature, and band-gap opening *Phys. Rev.* B **81** 205409

[25] Kotakoski J, Meyer J C, Kurasch S, Santos-Cottin D, Kaiser U and Krasheninnikov A V 2011 Stone-wales-type transformations in carbon nanostructures driven by electron irradiation *Phys. Rev.* B **83** 245420

[26] Eder F R, Kotakoski J, Kaiser U and Meyer J C 2014 A journey from order to disorder—atom by atom transformation from graphene to a 2D carbon glass *Sci. Rep.* **4** 4060

[27] Park H J, Skákalová V, Meyer J, Lee D S, Iwasaki T, Bumby C, Kaiser U and Roth S 2010 Growth and properties of chemically modified graphene *Phys. Status Solidi* **247** 2915–9

[28] Cockayne E, Rutter G M, Guisinger N P, Crain J N, First P N and Stroscio J A 2011 Grain boundary loops in graphene *Phys. Rev.* B **83** 195425

[29] Malola S, Häkkinen H and Koskinen P 2010 Structural, chemical, and dynamical trends in graphene grain boundaries *Phys. Rev.* B **81** 165447

[30] Huang P Y *et al* 2011 Grains and grain boundaries in single-layer graphene atomic patchwork quilts *Nature* **469** 389–92

[31] Kim K, Lee Z, Regan W, Kisielowski C, Crommie M F and Zettl A 2011 Grain boundary mapping in polycrystalline graphene *ACS Nano* **5** 2142–6

[32] Kotakoski J and Meyer J C 2012 Mechanical properties of polycrystalline graphene based on a realistic atomistic model *Phys. Rev.* B **85** 195447

[33] Liu Y and Yakobson B I 2010 Cones, pringles, and grain boundary landscapes in graphene topology *Nano Lett.* **10** 2178–83

[34] Los J H and Fasolino A 2003 Intrinsic long-range bond-order potential for carbon: performance in Monte Carlo simulations of graphitization *Phys. Rev.* B **68** 24107

[35] Plimpton S 1995 Fast parallel algorithms for short-range molecular dynamics *J. Comput. Phys.* **117** 1–19

[36] Plimpton S J and Thompson A P 2012 Computational aspects of many-body potentials *MRS Bull.* **37** 513–21

[37] Koch C 2002 Determination of core structure periodicity and point defect density along dislocations *PhD Thesis* Arizona State University

[38] Kirkland E J 2010 *Advanced Computing in Electron Microscopy* 2nd edn (New York: Springer)

Revealing the 3D Structure of Graphene Defects - Supplementary Information

Christoph Hofer[1], Christian Kramberger[1], Mohammad Reza Ahmadpour Monazam[1], Clemens Mangler[1], Andreas Mittelberger[1], Giacomo Argentero[1], Jani Kotakoski[1], and Jannik C. Meyer[1]

[1]Faculty of Physics, University of Vienna, Boltzmanngasse 5, A-1090, Vienna, Austria

1   STEM simulation method

Since our optimization is too computationally expensive for a complete STEM simulation, we use a simplified simulation where the image contrast is given by a set of points (atoms) and is broadened by a point spread function (taking into account aberrations). We have verified that, for a single layer of carbon atoms, this approach produces indinstinguishable results compared to a simulation using QSTEM [1]. The projected 2D positions from a set of three dimensional coordinates are calculated for the respective tilt angle. The phase of the aberrated wave front at a polar angle θ and azimuthal angle ϕ is modeled as

$$\chi(\theta_x, \theta_y) = (2\pi/\lambda) \cdot (C_1 (\theta_x^2 + \theta_y^2)/2 + C_{1,2a} (\theta_x^2 - \theta_y^2)/2 + C_{1,2b} \theta_x \theta_y +$$
$$C_{2,1a} \theta_x (\theta_x^2 - \theta_y^2)/3 + C_{2,1b} \theta_y (\theta_x^2 - \theta_y^2)/3 +$$
$$C_{2,3a} \theta_x (\theta_x^2 - 3\theta_y^2)/3 + C_{2,3b} \theta_y (3\theta_x^2 - \theta_y^2)/3)$$

where $\theta_x = \theta \cdot cos(\phi)$, $\theta_y = \theta \cdot sin(\phi)$, C_1 is the aberration coefficient of the defocus, $C_{1,2a}$ and $C_{1,2b}$ are the aberration coefficients of the astigmatism (with a relative angle of 90° with respect

1

to each other), $C_{2,1a}$ and $C_{2,1b}$ are the aberration coefficients of the coma and $C_{2,3a}$ and $C_{2,3b}$ are the aberration coefficients of the three-fold astigmatism [2]. λ is the wavelength of the incident electrons. The resulting aberrated electron wave function $\psi_f(\theta_x, \theta_y)$ is then multiplied by an aperture function and the point spread function is obtained as the square modulus of its inverse Fourier transform.

The final simulation is obtained by convoluting the point spread function with the image which represents the delta potential $M(\vec{x_1}, ..., \vec{x_n})$ of the structure. We use a zero-filled image with non zero pixel values on the atomic positions distributed over four pixels around the projected coordinates for sub-pixel accuracy. The pixel intensity is chosen such that it represents the integrated intensity on the detector of the respective atom. Using the convolution theorem yields our simulation S_0

$$S_0(\vec{x_1}, ..., \vec{x_n}) = FT^{-1}(\psi_f(\theta_x, \theta_y) \cdot FT\left(M(\vec{x_1}, ..., \vec{x_n})\right)).$$

In order to take the finite size of the tip of the electron gun, the energy spread and the atomic vibrations into account, we further processed our results by a Gaussian blur.

Supplementary Figure 1 summarizes the procedure of the simulation algorithm and compares the resulting image with the simulation obtained by QSTEM. The computation time is about 1000 times shorter with this algorithm.

2 Accuracy of the 3D reconstruction

As test structure for our approach, we simulated two STEM images with realistic experimental conditions (including noise) from a computational model. These images were used as input for our reconstruction algorithm (see Supplementary Figure 2a). This allows us to directly compare the reconstructed structure with the energy minimized model. Apart from noise, the reconstructed structure agrees well with the original model. Supplementary Figure 2d shows the distribution of the deviations of the corresponding atomic positions.

As a further potential source of error, we consider the effect of sample or beam drift during acquisition of a scanned image. Such drift would result in an offset in the projected atom positions that slowly varies during image acquisition, and hence, variations in the reconstructed height. As shown in one of the reconstructed grain boundaries (GBs) in Supplementary Figure
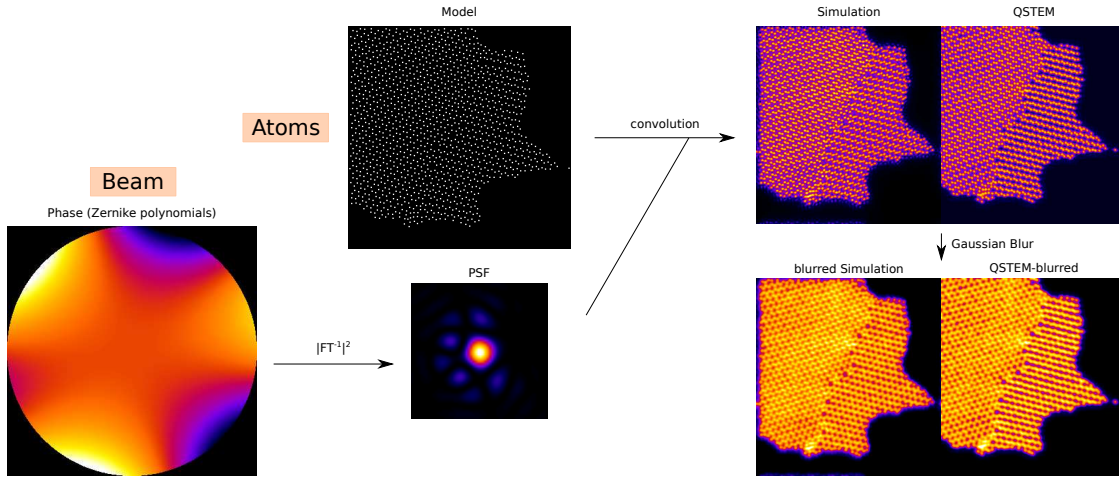
Supplementary Figure 1: Simplified simulation method to simulate monolayer materials. First, the phase of the electron beam is computed. With the real and imaginary part of the function, the FT is computed, squared and normalized in order to obtain the point spread function. Then the PSF is convoluted with the model, which is a black image with pixel spots at the projected atomic positions. To obtain the final simulation, the result is Gaussian blurred.

3, drift may result in small height variations along the slow scan direction. This artefact can be identified in the reconstruction from parallel undulations going across the entire sheet. Consequently, it is important to orient the scan pattern so that the fast scan direction probes the height variation of interest – for example, we choose the fast scan direction across the grain boundary. Along the fast scan direction, subsequent lines of the scan consititute a repeated measurement, so that sudden changes in the structure would be noticed as an unphysical line-to-line variation.

For a few structures, we managed to obtain more than two images before the atomic configuration changed. In this case, a further validation is possible. For example, the 3D reconstruction can be carried out in such a way that the difference between the simulation and the experiment is minimized with respect to all images. This was done for the grain boundaries with 23.6 and 24.6° misorientation angle (full data shown in Supplementary Figure 12 and 11). In both cases, the final difference images do not only contain noise, but show some weak periodic features indicating a mismatch that can not be fully resolved by the structural optimization. In Supplementary Figure 12, this effect is small, and indicated by a red circle. In Supplementary Figure 11, a larger residual mismatch between the simulation and the experiment is found (difference
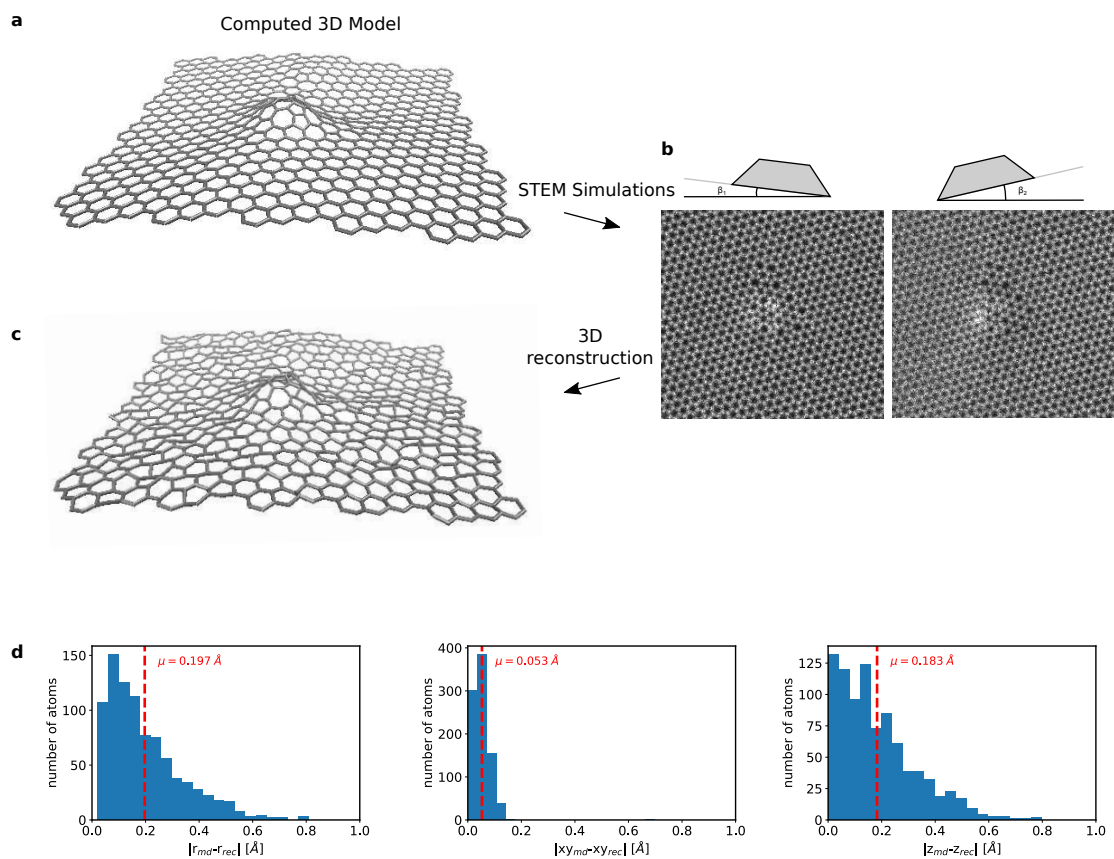
3

images show weak lattice fringes in some areas). Indeed, these fringes indicate some changes in the 3D structure or the imaging parameters (e.g. drift) between or during the measurements. Since the atomic configuration within the clean graphene region have not changed, they may have been caused, e.g., by changes in the contamination around the edges (which is indeed changing between images). These differences at the strongest point correspond to a mismatch in the projected position of 0.7 Å. However, the mismatch does not arise sharply from one atom to its neighbor, but rather indicate a difference in curvature of the graphene sheet between the grain boundary and the surrounding contamination.

In order to further evaluate the consequences of this effect, we created multiple 3D reconstructions from different pairs of these images. The results are shown in Supplementary Figure 4. Importantly, the 3D configurations of the grain boundary are in excellent agreement with each other. However, the height and curvature of the graphene sheet around the grain boundary differs slightly. Hence, we can conclude that the changes in the contamination slightly affect the curvature of the graphene, but not the atomic configuration near the defects. In any case, the differences between these reconstructions are clearly at a level where they do not affect the conclusions of the present work.

Also for the rotated grain structure, we were able to record four images. Here, the difference between all experimental and simulated images is reduced to noise after the 3D optimization (Supplementary Figure 15, bottom line). Hence, in this case we can exclude any changes in the structure as well as sample or beam drift during imaging.

3   Additional structures

Supplementary Figure 5 shows three more grain boundaries. For each structure, we show the top view colored based on the z-coordinate of each atom as well as two line profiles: one along the y-axis that contains all atoms in the structure and another along the x-axis that is limited to a narrow strip of atoms located within ca. 1 nm around the GB. From the line profiles, we also calculate the maximum corrugation (Δz), height variation (σ_z), defined as the standard deviation of the out-of-plane coordinate of the atoms in the structure from the mean value and the kink angle (α) which is measured across the grain boundary. For an optical impression of the structure, we also show a perspective view of the bonds with the same color-code as in the

4

a Computed 3D Model

b STEM Simulations

c 3D reconstruction

d

Supplementary Figure 2: Comparison between a modeled 3D structure and a reconstructed structure. a) Energy-minimized structure. b) Two STEM simulations of the known structure with an relative tilt angle of $20°$ and noise corresponding to an electron dose of $5 \cdot 10^5 \ e^-/Å^2$. c) Reconstructed structure. d) Histograms of the deviations of the corresponding atomic positions. Left: Total deviation. Middle: In-plane deviation. Right: Out-of-plane deviation.
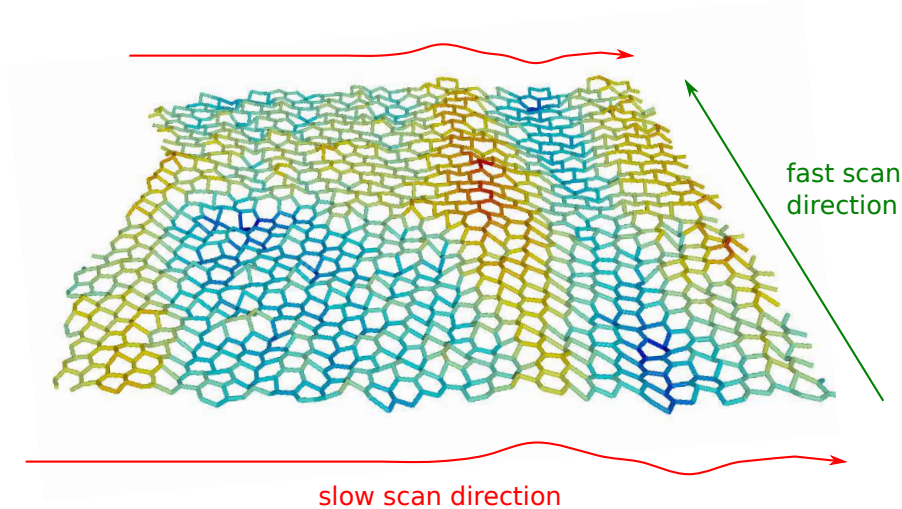
Supplementary Figure 3: 3D structure of a grain boundary shown in Figure 6a of the main article. The undulation along the slow scan direction reveals a scan distortion.

top view.

Supplementary Figure 6 shows the color-coded top view, a line profile, and a perspective view of the small rotated grain (flower defect) for the experimental reconstruction and the simulated structure. Apart from noise in the experimental data, an excellent match is obtained.

4 Complete set of raw and processed images

Supplementary Figures 7-15 show all raw and processed data used in this work. For each structure, we show the raw data with the corresponding tilt angle, the filtered data, the simulations of the final 3D model, and the difference between the simulated and experimental data.

References

[1] C. Koch, *Determination of core structure periodicity and point defect density along dislocations*. PhD thesis, Arizona State University, 2002.

6
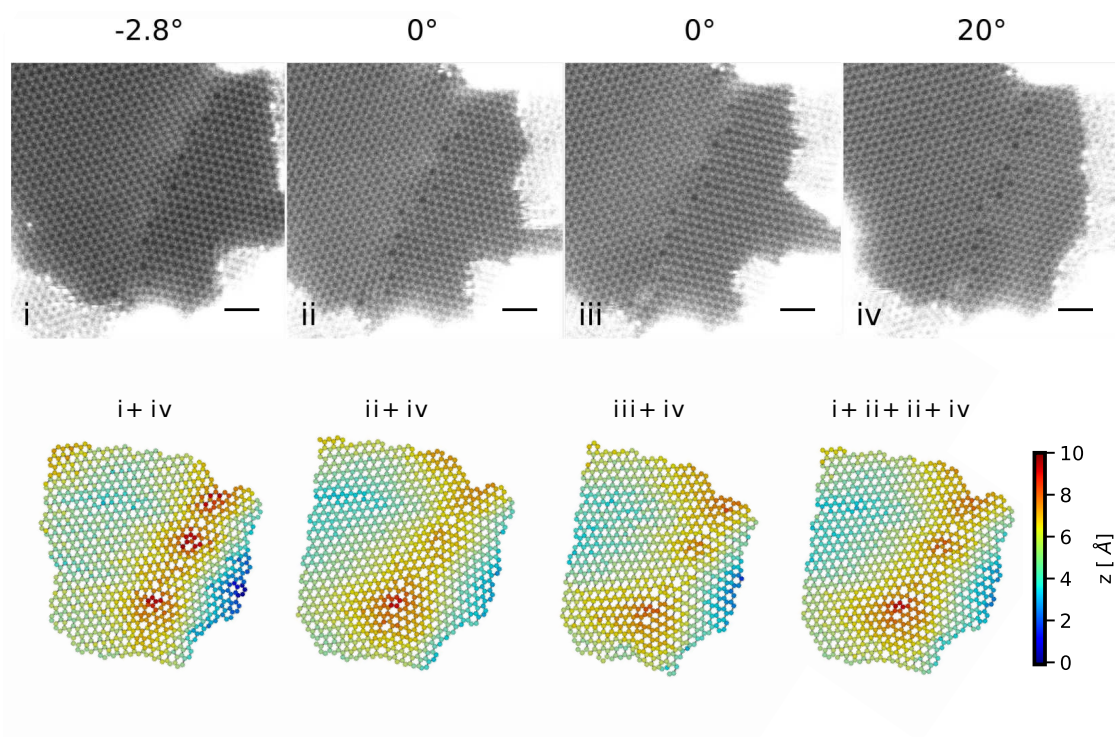
Supplementary Figure 4: 3D structures of a grain boundary obtained with different pairs of images. Top: experimental images with sample tilt of -2.8°, 0°, 0° and 20°, respectively. Bottom: Color-coded top view of the reconstructions using different images. The same grain boundary is shown in Supplementary Figure 5b

7
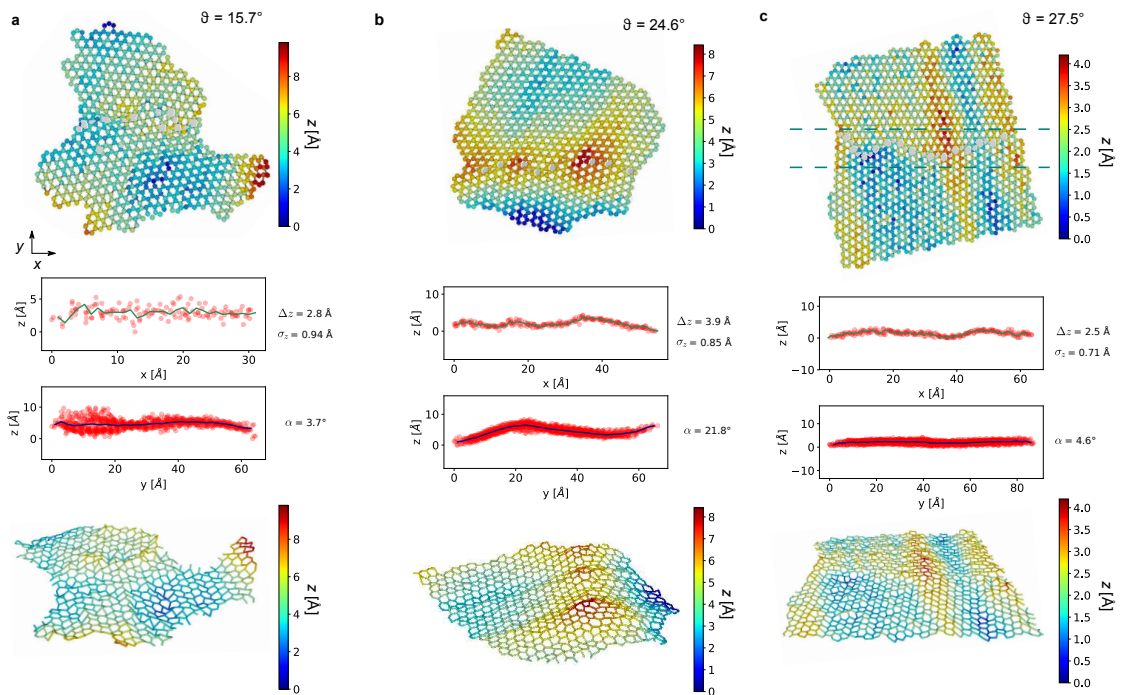
Supplementary Figure 5: Atomic structures of three grain boundaries. The line profiles under the top views show side views for the x-direction for atoms within ca. 1 nm around the grain boundary (green dashed area) and for the y-direction for all atoms in the structure. Definitions for the maximum corrugation (Δz), height variation (σ_z) and kink angle (α) are shown in Figure 5a of the main article.

8
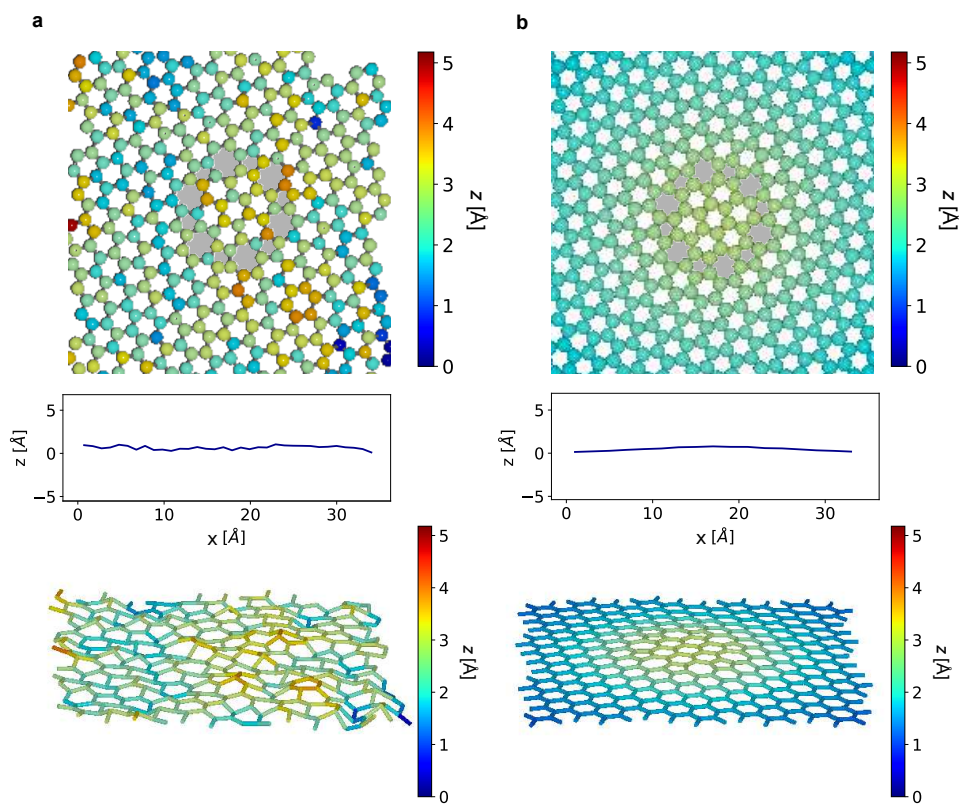
Supplementary Figure 6: 3D structure of the flower defect. (a) Structure obtained through experimental reconstruction from STEM-MAADF images. (b) Structure obtained computationally through energy minimization. Below the line profile, a perspective view of the structure is shown (only color-coded bonds shown).
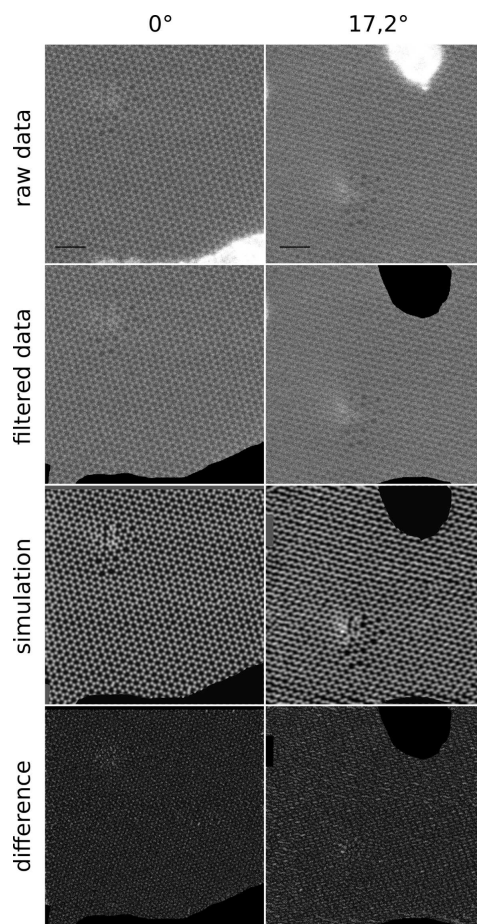
Supplementary Figure 7: Experimental data, filtered data for processing, simulations and the difference of the extended defect in Figure 4 of the main article.
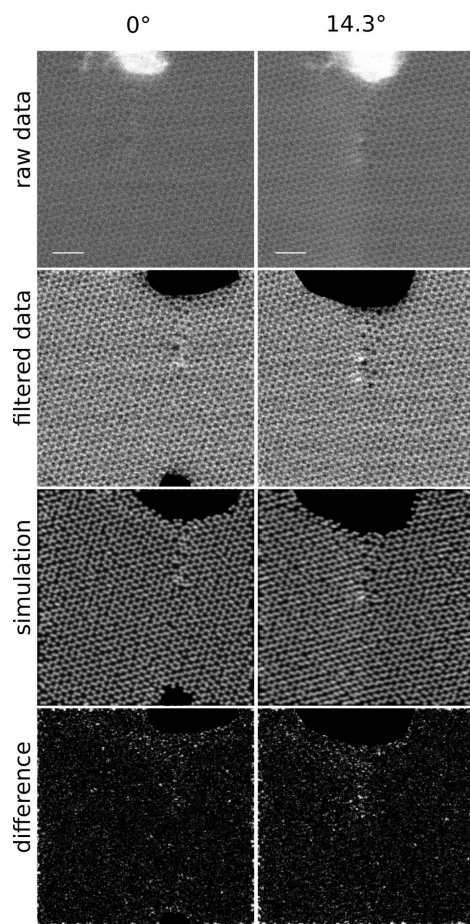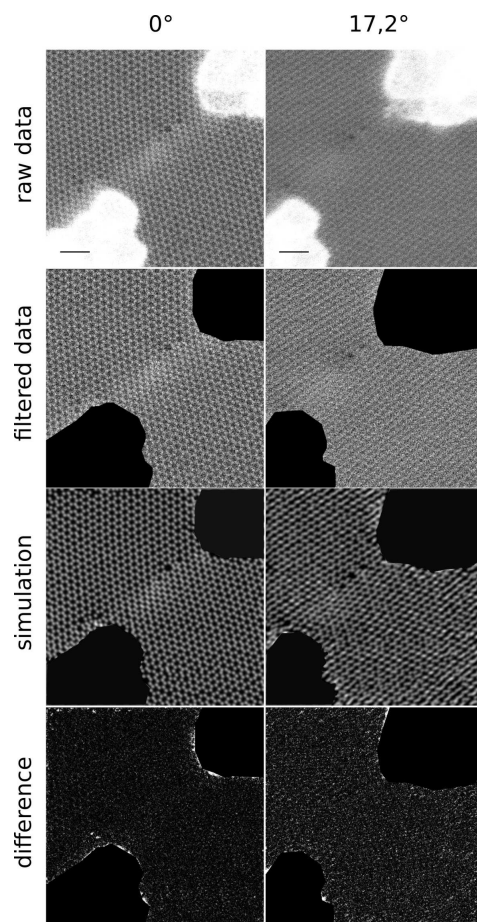
10

Figure 8: Experimental data, filtered data for processing, simulations and the difference of the grain boundary in Figure 5a. of the main article.

11

Supplementary Figure 9: Experimental data, filtered data for processing, simulations and the difference of the grain boundary in Figure 5b. of the main article.
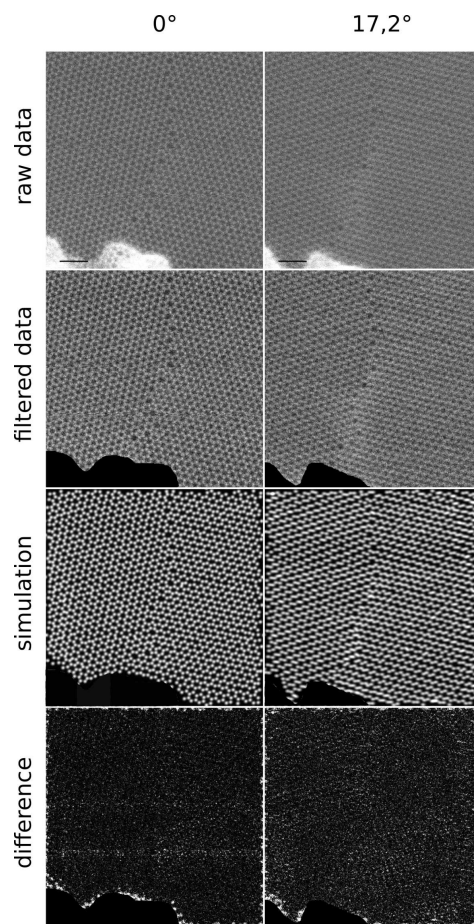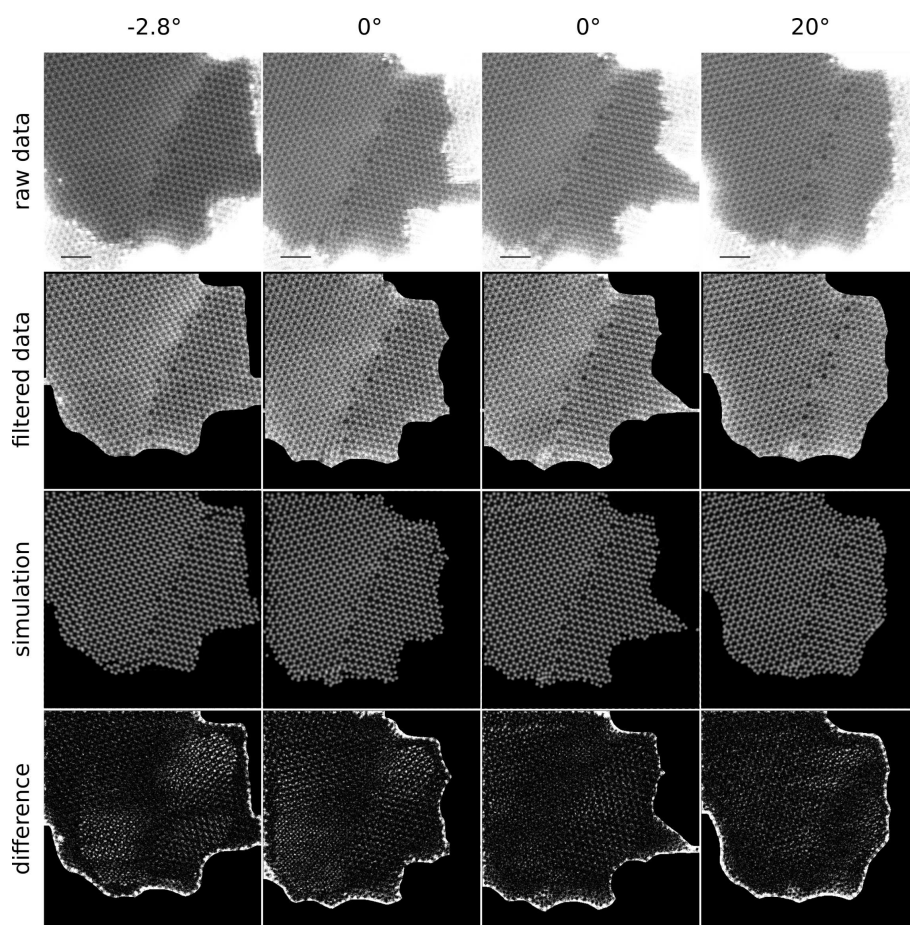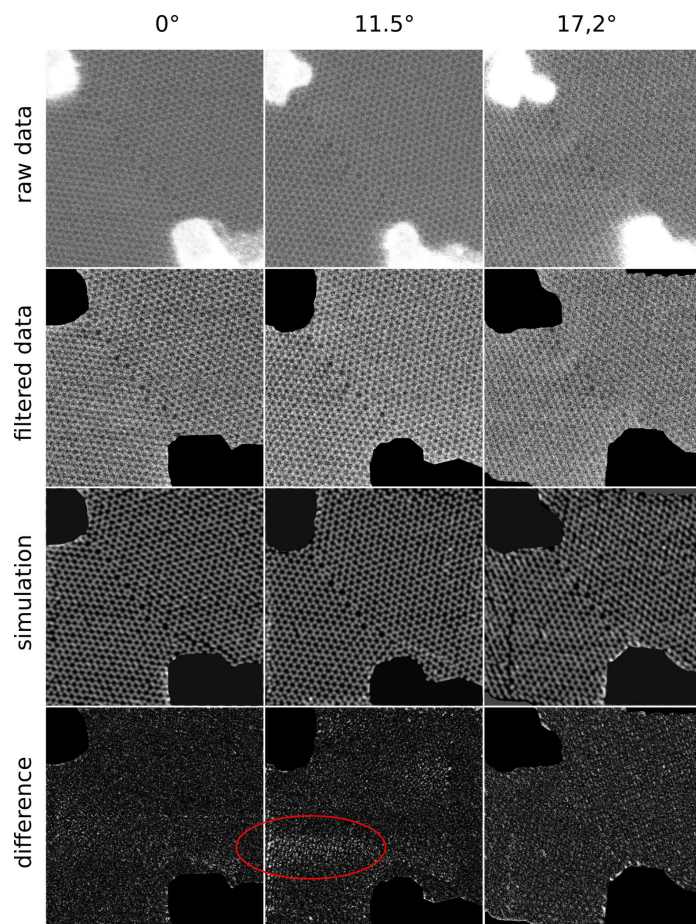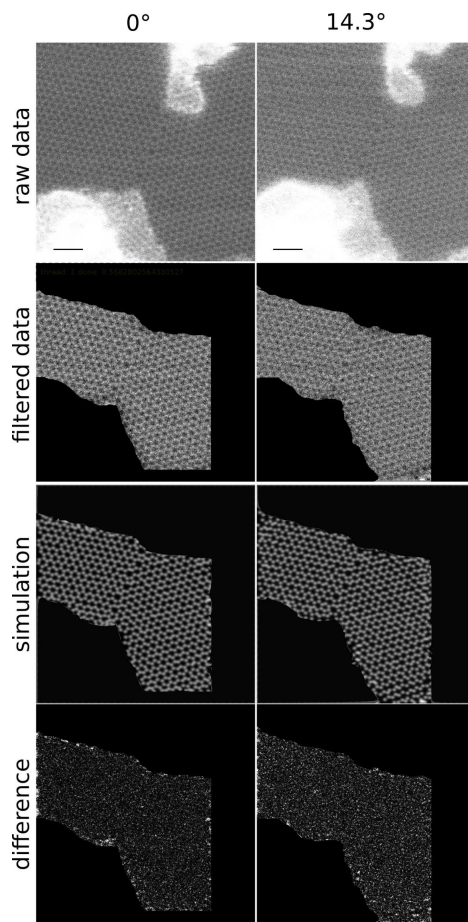
12

Figure 10: Experimental data, filtered data for processing, simulations and the difference of the grain boundary in Supplementary Figure 5c.

Supplementary Figure 11: Experimental data, filtered data for processing, simulations and the difference of the grain boundary in Supplementary Figure 5b.

14

Supplementary Figure 12: Experimental data, filtered data for processing, simulations and the difference of the grain boundary in Figure 6a of the main article.

Supplementary Figure 13: Experimental data, filtered data for processing, simulations and the difference of the grain boundary in Figure 6b of the main article.

16

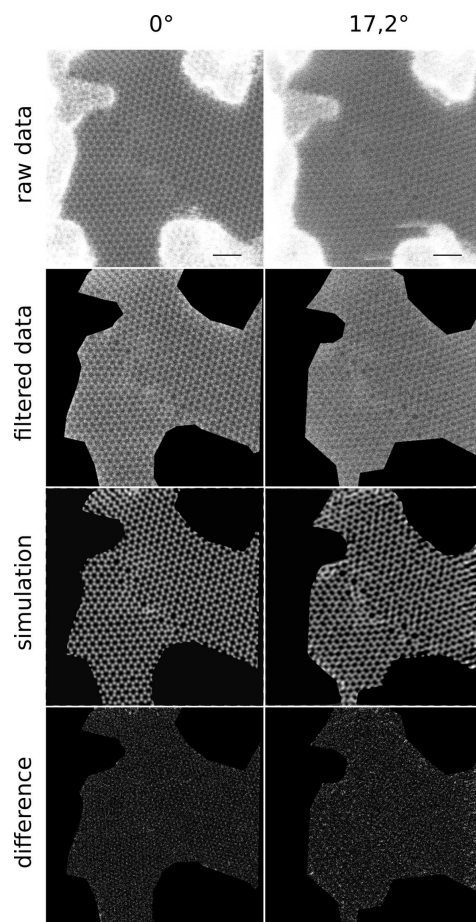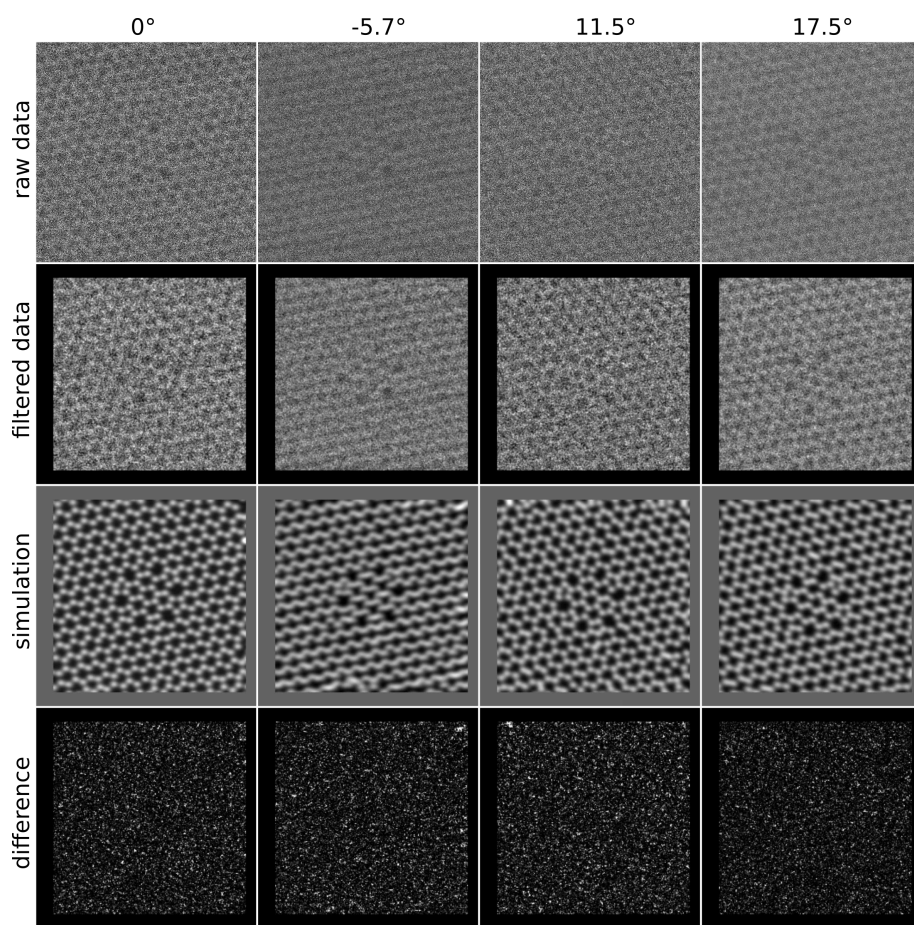Figure 14: Experimental data, filtered data for processing, simulations and the difference of the grain boundary in Supplementary Figure 5a.

Supplementary Figure 15: Experimental data, filtered data for processing, simulations and the difference of the flower defect in Supplementary Figure 6

18

[2] E. J. Kirkland, *Advanced computing in electron microscopy*. New York: Springer US, 2 ed., 2010.

4.2 Paper II

Paper II is a follow up to the first paper. It presents the 3D structure of Si impurities in graphene in the form of substitutions, trimers and tetramers. Moreover, it reveals interesting dynamics of these heteroatoms induced by the electron beam.

Author contributions

The author of this thesis performed STEM measurements, carried out the 3D reconstruction, analyzed the structures and drafted the figures and the manuscript. V.S. performed the sample preparation and participated in the STEM experiments. M.R.A.M. and T.S. performed the DFT simulations. C.M. prepared alignments for the STEM instrument and supported the experiments. J.K. and J.C.M conceived and supervised the study.

Direct visualization of the 3D structure of silicon impurities in graphene

Christoph Hofer (iD), Viera Skakalova (iD), Mohammad R. A. Monazam, Clemens Mangler, Jani Kotakoski (iD), Toma Susi (iD), and Jannik C. Meyer (iD)

View Online   Export Citation   CrossMark

ARTICLES YOU MAY BE INTERESTED IN

AIP Publishing

Direct visualization of the 3D structure of silicon impurities in graphene

Christoph Hofer,[1,2,a)] (iD) Viera Skakalova,[1] (iD) Mohammad R. A. Monazam,[1] Clemens Mangler,[1] Jani Kotakoski,[1] (iD)
Toma Susi,[1] (iD) and Jannik C. Meyer[1,2,a)] (iD)

AFFILIATIONS

[1] Faculty of Physics, University of Vienna, Boltzmanngasse 5, A-1090 Vienna, Austria
[2] Institute for Applied Physics, Eberhard Karls University of Tuebingen, Auf der Morgenstelle 10, D-72076 Tuebingen, Germany

[a)]Electronic addresses: christoph.hofer@uni-tuebingen.de, jannik.meyer@uni-tuebingen.de

ABSTRACT

We directly visualize the three-dimensional (3D) geometry and dynamics of silicon impurities in graphene as well as their dynamics by aberration-corrected scanning transmission electron microscopy. By acquiring images when the sample is tilted, we show that an asymmetry of the atomic position of the heteroatom in the projection reveals the non-planarity of the structure. From a sequence of images, we further demonstrate that the Si atom switches between up- and down- configurations with respect to the graphene plane, with an asymmetric cross-section. We further analyze the 3D structure and dynamics of a silicon tetramer in graphene. Our results clarify the out-of-plane structure of impurities in graphene by direct experimental observation and open a route to study their dynamics in three dimensions.

Published under license by AIP Publishing. https://doi.org/10.1063/1.5063449

Although the extraordinary properties of pristine graphene have raised enormous interest in the scientific community and industry, most applications require modified properties such as a non-zero energy bandgap in the electronic structure.[1,2] One approach to tailor graphene properties is doping with heteroatoms, which may open a bandgap[3–6] or enhance local plasmon resonances.[7] To understand the influence of atomic substitutions, the three-dimensional (3D) position of every atom has to be determined. The 3D structure as well as the beam-induced dynamics is also important in the context of single atom manipulation in graphene.[8–10]

Out-of-plane buckling of heteroatoms has already been demonstrated indirectly by analyzing the fine structure of electron energy loss spectra.[11–14] Nevertheless, to fully understand the real magnitude of the displacement from the graphene plane as well as the local lattice distortion, there is a need for directly measuring the 3D structure. Although recent advances in scanning transmission electron microscopy (STEM) allow extracting structural and chemical information at the atomic scale,[15,16] this is only possible as a two-dimensional projection of the object. Electron tomography allows the reconstruction of the 3D atomic structure[17–21] but requires a large number of images from different projections, which is difficult to obtain for radiation sensitive structures.

Here, we obtain the structure of an ultra-thin sample—one atomic layer for the Si substitution or up to two atoms behind each other in a projection for the Si tetramer—from a small number of images with different sample tilts. We directly show the out-of-plane buckling induced by the Si dopant from the medium-angle annular dark-field (MAADF) STEM images with the sample (and hence the plane of the graphene sheet) tilted by approximately 20° away from the normal incidence of the electron beam. While the Si dopant in graphene appears symmetric in normal incidence plane-view images,[11] the out-of-plane deformation of the atoms causes a significant symmetry breaking of the atomic positions in the tilted projection. First, we show that a computationally relaxed model of a silicon substitution in graphene matches significantly better to a tilted STEM image of this structure than to a flat one. This already indicates that the theoretical model agrees well with the experimental observation. For a quantitative analysis of the 3D structure, we use an optimization process where an atomistic model is iteratively optimized to achieve the best possible fit to two experimental images with different viewing angles. The details of the method are described in Ref. 22.

Since the electron beam can transfer more energy to Si in the graphene lattice than is required for flipping a buckled Si

atom from one side of the lattice to the other,[8] this process should be expected. As a consequence, one might expect all Si atoms to be on the side opposite from the electron source. However, our results reveal both configurations and the transition between the two. We also show the 3D structure of a pyramid-like Si-tetramer, whose formation and observation were reported in Ref. 23. Also in our case, the structure was formed from a Si trimer[24] by the capture of an additional Si atom. Calculations show that the central Si atom in the tetrameric configuration is almost 3 Å above the graphene plane. The projected position of this atom is displaced relative to the other atoms when the sample is tilted. Also here, the 3D structure can be reconstructed by matching the model to the experimental images, and our reconstruction is in excellent agreement with the computer model. Similar to the single Si substitution, we observed a single flipping event presumably induced by the electron beam. Our results not only show experimentally obtained 3D structures but also provide insights into their electron beam induced out-of-plane dynamics.

Figure 1 shows a STEM image of a Si dopant with a sample tilt of ca. 18°, overlaid by a tilted flat model (left panel) and a relaxed model (right panel). The model was scaled and translated so that the graphene lattice around the impurity matches the experimental image. In the flat structure, the expected Si position deviates from the experimentally observed position, whereas the carbon positions match very well. However, a visually perfect match between the model and the STEM projection can be obtained by overlaying the computationally relaxed 3D model to the experimental image. This approach already qualitatively
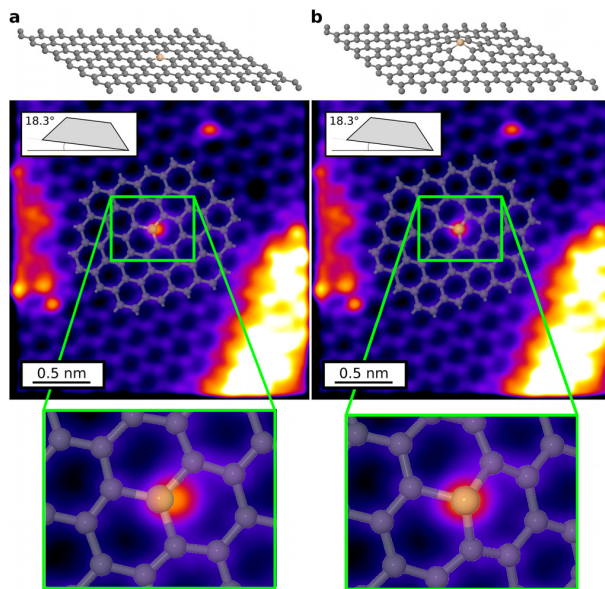

FIG. 1. Double-gaussian-processed[25] STEM image of a Si dopant in graphene overlaid by a flat model (a) and a relaxed model (b). On the top row, a side view of the used models is shown. The magnified image (bottom) shows a poor match of the Si atom position using the flat model (a) but an excellent match using a buckled structure (b).

confirms that the theoretically predicted 3D structure can also be verified using an electron microscope.

Figure 2 shows two different STEM images with a Si substitution with the same sample tilt as in Fig. 1. From the tilt direction, the Si atom in panel (a) can be identified as sticking above the graphene plane (with respect to the electron beam coming from the bottom in our microscope). Although two energetically equivalent states of the silicon (buckling above and below the graphene plane) are expected, this configuration appears to be more frequent due to the direction of the electron beam. After several more scans, the same projected silicon atom is seen on the other side of the graphene plane [panel (b)]. The stability of this configuration is, as expected to be, much lower than the previous one because the direction of the buckling is opposite to the direction of the momentum of the electron beam. The expected dose required to cause the dopant to flip from "up" to "down" and vice versa is calculated by a Poisson analysis. The electron doses until a corresponding event occurs are collected and shown in the histograms in Fig. 2. In total, 10 events for each configuration are used for the analysis. The blue and the orange columns show the flip from above the graphene plane to below (towards the electron beam) and vice versa. A Poisson fit yields the mean values $\lambda_u = 2.87 \times 10^6$ e$^-$ Å^2 for the flip from up to down and $\lambda_d = 4.96 \times 10^5$ e$^-$ Å^2 for the flip from down to up.

Based on a density functional theory (DFT) molecular dynamics simulation,[8] the kinetic energy perpendicular to the graphene lattice that a probe electron would need to transfer to a Si substitution in order to shift it from one side of the graphene lattice to the other is between 1.375 eV and 1.50 eV. For our 60 keV electron beam, this corresponds to a cross section of about 1100 barn.[26] The experimentally observed areal event dose of 0.5×10^6 e$^-$ Å^2 corresponds to a cross section value of 200 barn. On the other hand, the Si bouncing back to the side facing towards the electron beam was not observed in the molecular dynamics simulation. These discrepancies might be due to non-perpendicular momentum transfers due to sample tilt. Including a full description of the angular dependence of the momentum transfer and of the displacement threshold energy itself[27] would potentially improve agreement with experiment but is beyond our scope here.

With experimental images of the "up" and "down" configuration at a fixed sample tilt, and a reference image of the impurity at zero sample tilt, we reconstruct the 3D configuration as described previously.[22] In brief, an atomistic model is created, and the atoms are shifted in such a way that the difference between the experimental images and simulated images is minimized. The obtained 3D structures in the corresponding orientations are shown in the bottom row of Fig. 2. Besides the out-of-plane position of the Si impurity, they reveal slight buckling also of the surrounding graphene sheet. The Si-C bond length obtained from the experimental data via the 3D reconstructions is (1.68 ± 0.07) Å, which is close to the theoretical prediction (1.74 Å).

Next, we show the 3D structure of a Si tetramer. This structure is very beam stable allowing us to tilt the sample in different directions and reconstruct its three-dimensional shape. Computational studies of this structure reveal a triangular pyramid structure, where the central Si atom is sticking out of the
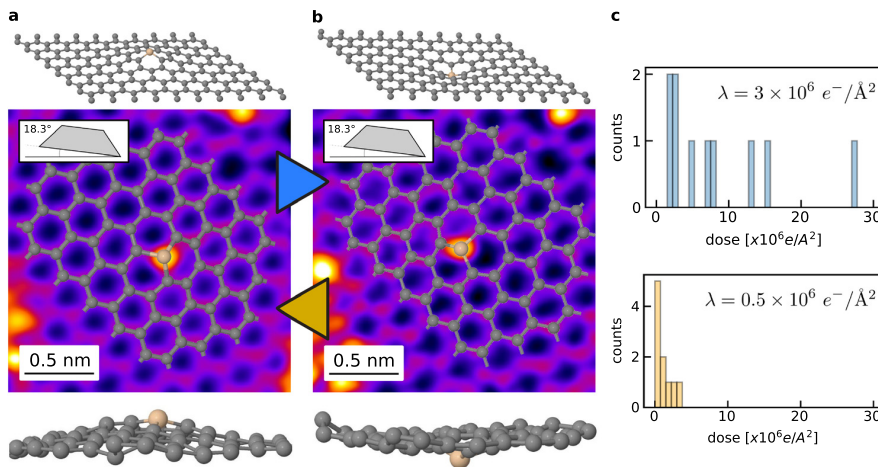
FIG. 2. Double-gaussian-processed STEM images of a Si dopant in graphene with a sample tilt of ca. 18°. On the top row, a side view of the used models is shown. Panels a and b show that the experiment exhibits both "buckled up" and "buckled down" structures. The bottom row shows the actual 3D reconstruction. Panel c shows how much dose is required to flip the Si from below the graphene plane to above it and vice versa, respectively in orange and blue.
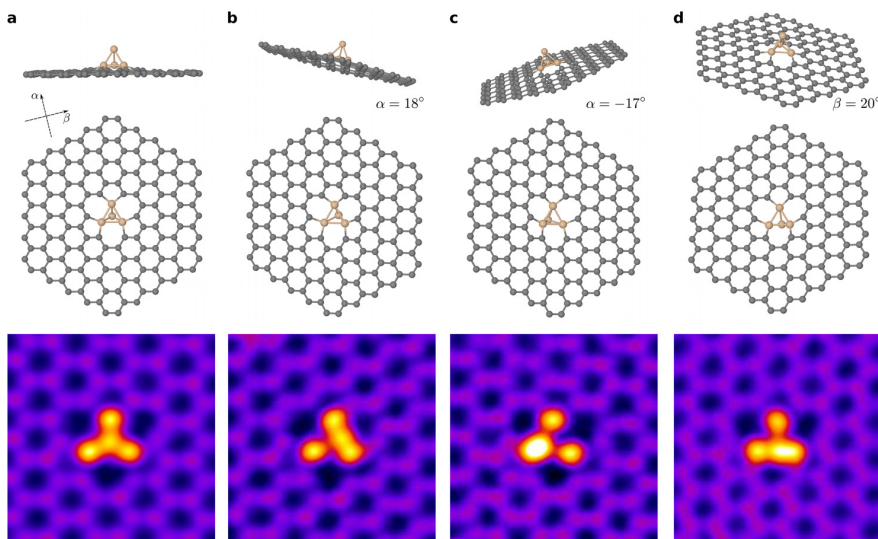
FIG. 3. Computational models (side view in the top row and top view in the second row) and double-gaussian-processed STEM images of a Si tetramer in graphene (bottom row) with a non-tilted specimen (a) and with a specimen tilt of ca. 20° (b)–(d) in different directions. The highly asymmetric displacement of the central Si atom indicates a significantly out-of-plane position.

plane by ca. 3 Å. The top row of Fig. 3 shows a side view of the relaxed model tilted in different directions. The top view (second row) shows the projected positions with respect to the electron beam. The experimental images (third row) agree well with the model. Again, we further reconstruct the 3D shape using all four projections, and the result matches precisely with simulations (Fig. 4).

We also observed a transition of the tetramer, where the Si$_4$ pyramid flipped from below to above the graphene plane. Also in this case, breaking the symmetry by tilting the sample is the key to observe the dynamics. Figure 5(a) shows a STEM image of a Si trimer, which captures a fourth Si atom to create the tetramer (b). In this case, the Si was captured below the graphene plane.

However, after some time the continuous electron irradiation triggers a transition to an intermediate step (panel c), which could not be clearly identified. Eventually, the Si atoms are arranged again as a tetramer, facing in the opposite direction with respect to the initial state. Hence, the whole tetramer was

FIG. 4. 3D structures of the Si tetramer obtained by image reconstruction (left) and DFT calculation (right).

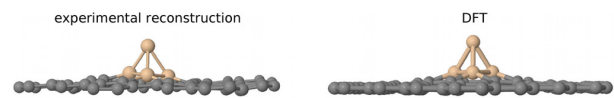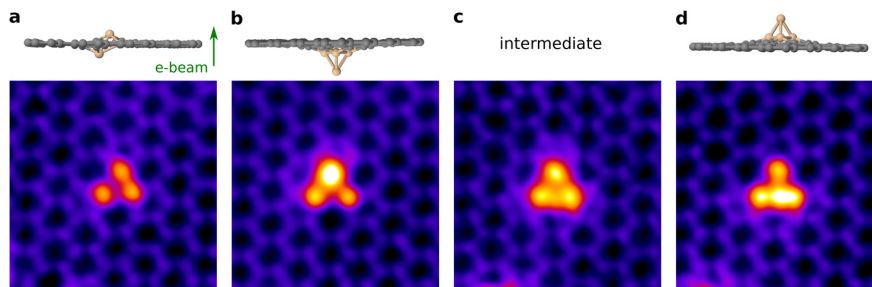**FIG. 5.** Computational models and double-gaussian-processed STEM images of the Si tetramer in graphene with a sample tilt of ca. 20°. After a fourth Si atom formed the tetramer, the pyramid like structure transitioned after an electron dose of ca. 1.6×10^7 e$^-$ Å^{-2} to the other side of graphene, facing away from the electron beam. This configuration did not change further. The top row shows the 3D models of the expected structures.

flipped to the opposite side of the graphene plane, where it remained stable for a large number of atomically resolved STEM images.

We have experimentally confirmed the out-of-plane structure of a single Si substitution and revealed the 3D structure of a Si tetramer in graphene. The single silicon dopant induced a buckling of the surrounding graphene sheet and we observed its electron beam induced flip in both directions, with an asymmetric cross-section. The Si tetramer is stable under the electron beam, after changing from opposing the electron beam to the other side of graphene. Our results provide insights into the structure and dynamics of Si dopants in graphene, and the approach may be extended to other impurities.

For our experiment, we used graphene oxide (GO; Danubia NanoTech, CAS No. 7782-42-5) which contains mobile C and Si adatoms as by-products. Water dispersion of GO was received from Danubia NanoTech, Ltd. The oxidation method of graphitic powder and subsequent exfoliation were developed by the company with an ultimate goal to preserve the long-range structural order in the graphene oxide flakes exfoliated down to the single-atom thickness. Water dispersion of GO was significantly diluted (∼1:100); a TEM grid was then vertically dipped into the dispersion for a minute and dried in air afterwards. The sample was baked for 8 h at 160 °C in ultra-high vacuum before inserting it into the microscope. Patches of clean graphene were revealed after reducing the functional groups by electron exposure.

Scanning transmission electron microscopy (STEM) experiments were conducted using a Nion UltraSTEM100, operated at 60 kV. Typically, our atomic-resolution images were recorded with 512×512 pixels for a field of view of 2–4 nm and a dwell time of 16 μs per pixel using the medium angle annular dark field (MAADF) detector with a semi-angular detector range of 60–200 mrad. The probe current was approximately 20 pA and the (semi-)convergence angle was 30 mrad. To enhance the signal, 2–5 identical images were averaged, if the structure clearly did not change.

Density functional theory as implemented in the GPAW package was used to minimize structural models of the Si substitution[8] and the Si$_4$ pyramid. For the latter case, a graphene supercell of $11 \times 11 \times 1$ containing 242 carbon atoms was constructed. Some of the carbon atoms were substituted with Si to construct a model matching the experimental observation. Employing the LCAO double zeta polarized basis set, a $|k|$-point mesh of $5 \times 5 \times 1$, the Perdew-Burke-Ernzerhof (PBE) functional, and a computational grid spacing of 0.2 Å, the models were

relaxed until the maximum forces were less than 0.01 eV Å^{-1}. In addition, we estimated via molecular dynamics simulations[8] the perpendicular kinetic energy required to shift a Si substitution from one side of the graphene lattice to the other.

See supplementary material for the whole set of raw data.

REFERENCES

[1] S. Y. Zhou, G.-H. Gweon, A. V. Fedorov, P. N. First, W. A. de Heer, D.-H. Lee, F. Guinea, A. H. Castro Neto, and A. Lanzara, "Substrate-induced bandgap opening in epitaxial graphene," Nat. Mater. **6**, 770–775 (2007).

[2] F. Schwierz, "Graphene transistors," Nat. Nanotechnol. **5**, 487–496 (2010).

[3] M. S. Azadeh, A. Kokabi, M. Hosseini, and M. Fardmanesh, "Tunable bandgap opening in the proposed structure of silicon-doped graphene," Micro Nano Lett. **6**, 582 (2011).

[4] M. Shahrokhi and C. Leonard, "Tuning the band gap and optical spectra of silicon-doped graphene: Many-body effects and excitonic states," J. Alloys Compd. **693**, 1185–1196 (2017).

[5] M. Houmad, H. Zaari, A. Benyoussef, A. El Kenz, and H. Ez-Zahraouy, "Optical conductivity enhancement and band gap opening with silicon doped graphene," Carbon **94**, 1021–1027 (2015).

[6] S. J. Zhang, S. S. Lin, X. Q. Li, X. Y. Liu, H. A. Wu, W. L. Xu, P. Wang, Z. Q. Wu, H. K. Zhong, and Z. J. Xu, "Opening the band gap of graphene through silicon doping for the improved performance of graphene/GaAs hetero-junction solar cells," Nanoscale **8**, 226–232 (2016).

[7] A. N. Grigorenko, M. Polini, and K. S. Novoselov, "Graphene plasmonics," Nat. Photonics **6**, 749–758 (2012).

[8] T. Susi, J. Kotakoski, D. Kepaptsoglou, C. Mangler, T. C. Lovejoy, O. L. Krivanek, R. Zan, U. Bangert, P. Ayala, J. C. Meyer, and Q. Ramasse, "Silicon carbon bond inversions driven by 60-keV electrons in graphene," Phys. Rev. Lett. **113**, 115501 (2014).

[9] T. Susi, D. Kepaptsoglou, Y.-C. Lin, Q. M. Ramasse, J. C. Meyer, K. Suenaga, and J. Kotakoski, "Towards atomically precise manipulation of 2D nano-structures in the electron microscope," 2D Mater. **4**, 042004 (2017).

[10] M. Tripathi, A. Mittelberger, N. A. Pike, C. Mangler, J. C. Meyer, M. J. Verstraete, J. Kotakoski, and T. Susi, "Electron-beam manipulation of silicon dopants in graphene," Nano Lett. **18**, 5319–5323 (2018).

[11] Q. M. Ramasse, C. R. Seabourne, D.-M. Kepaptsoglou, R. Zan, U. Bangert, and A. J. Scott, "Probing the bonding and electronic structure of single atom dopants in graphene with electron energy loss spectroscopy," Nano Lett. **13**, 4989–4995 (2013).

[12] M. Tripathi, A. Markevich, R. Böttger, S. Facsko, E. Besley, J. Kotakoski, and T. Susi, "Implanting germanium into graphene," ACS Nano **12**(5), 4641–4647 (2018).

[13] T. Susi, T. P. Hardcastle, H. Hofsäss, A. Mittelberger, T. J. Pennycook, C. Mangler, R. Drummond-Brydson, A. J. Scott, J. C. Meyer, and J. Kotakoski, "Single-atom spectroscopy of phosphorus dopants implanted into graphene," 2D Mater. **4**, 021013 (2017).

[14] W. Zhou, M. D. Kapetanakis, M. P. Prange, S. T. Pantelides, S. J. Pennycook, and J.-C. Idrobo, "Direct determination of the chemical bonding of individual impurities in graphene," Phys. Rev. Lett. **109**, 206803 (2012).

[15] O. Krivanek, N. Dellby, and A. Lupini, "Towards sub-Å electron beams," Ultramicroscopy **78**, 1–11 (1999).

[16] C. Colliex, "Seeing and measuring with electrons: Transmission electron microscopy today and tomorrow–An introduction," C. R. Phys. **15**, 101–109 (2014).

[17] S. Bals, B. Goris, T. Altantzis, H. Heidari, S. Van Aert, and G. Van Tendeloo, "Seeing and measuring in 3D with electrons," C. R. Phys. **15**, 140–150 (2014).

[18] J. Miao, P. Ercius, and S. J. L. Billinge, "Atomic electron tomography: 3D structures without crystals," Science **353**, aaf2157 (2016).

[19] M. Weyland and P. A. Midgley, "Electron tomography," Mater. Today **7**, 32–40 (2004).

[20] R. Xu, C.-C. Chen, L. Wu, M. C. Scott, W. Theis, C. Ophus, M. Bartels, Y. Yang, H. Ramezani-Dakhel, M. R. Sawaya, H. Heinz, L. D. Marks, P. Ercius, and J. Miao, "Three-dimensional coordinates of individual atoms in materials revealed by electron tomography," Nat. Mater. **14**, 1099–1103 (2015).

[21] Y. Yang, C.-C. Chen, M. C. Scott, C. Ophus, R. Xu, A. Pryor, L. Wu, F. Sun, W. Theis, J. Zhou, M. Eisenbach, P. R. C. Kent, R. F. Sabirianov, H. Zeng, P. Ercius, and J. Miao, "Deciphering chemical order/disorder and material properties at the single-atom level," Nature **542**, 75–79 (2017).

[22] C. Hofer, C. Kramberger, M. R. A. P. Monazam, C. Mangler, A. Mittelberger, G. Argentero, J. Kotakoski, and J. C. Meyer, "Revealing the 3D structure of graphene defects," 2D Mater. **5**(4) (2018).

[23] O. Dyck, S. Kim, E. Jimenez-Izal, A. N. Alexandrova, S. V. Kalinin, and S. Jesse, "Building structures atom-by-atom via electron beam manipulation," Small **14**, 1801771 (2018).

[24] Z. Yang, L. Yin, J. Lee, W. Ren, H.-M. Cheng, H. Ye, S. T. Pantelides, S. J. Pennycook, and M. F. Chisholm, "Direct observation of atomic dynamics and silicon doping at a topological defect in graphene," Angew. Chem. **126**, 9054–9058 (2014).

[25] O. L. Krivanek, M. F. Chisholm, V. Nicolosi, T. J. Pennycook, G. J. Corbin, N. Dellby, M. F. Murfitt, C. S. Own, Z. S. Szilagyi, M. P. Oxley, S. T. Pantelides, and S. J. Pennycook, "Atom-by-atom structural and chemical analysis by annular dark-field electron microscopy," Nature **464**, 571–574 (2010).

[26] T. Susi, C. Hofer, G. Argentero, G. T. Leuthner, T. J. Pennycook, C. Mangler, J. C. Meyer, and J. Kotakoski, "Isotope analysis in the transmission electron microscope," Nat. Commun. **7**, 13040 (2016).

[27] C. Su, M. Tripathi, Q.-B. Yan, Z. Wang, Z. Zhang, L. Basile, G. Su, M. Dong, J. Kotakoski, J. Kong, J.-C. Idrobo, T. Susi, and J. Li, "Competing dynamics of single phosphorus dopant in graphene with electron irradiation," preprint arXiv:1803.01369 (2018).

Direct visualization of the 3D structure of silicon impurities in graphene - Supplementary Information

Christoph Hofer[1], Viera Skakalova[1], Mohammad Reza Ahmadpour Monazam[1], Clemens Mangler[1], Jani Kotakoski[1], Toma Susi[1], and Jannik C. Meyer[1]

[1]Faculty of Physics, University of Vienna, Boltzmanngasse 5, A-1090, Vienna, Austria

Example of Si substitution in tilted projection

Supplementary Figure 1 shows one example of the flipping process of a single Si substitution. The sample is tilted by approx. 20 degrees and the numbers in the arrows show the number of frames until the flip occurs. All the images are averaged, all individual unprocessed images are found in Video 1. Supplementary Figure 2 shows the raw images of the processed images shown in Figure 3 of the main text.

Raw data and videos

The Video files 1-3 show unprocessed STEM images with a sample tilt of ca. $\alpha = 19°, \alpha = 19°$ and $\beta = 20°$ as videos of the Si substitution, respectively. Alpha and beta are the tilt axis aligned to the y and x axis of the image, respectively. Here, the flipping process can be seen clearly. Video 4 and 5 shows a sequence of unprocessed STEM images with a sample tilt of $\beta = 17°$ of the Si tetramer. The first video of them shows the formation from a Si trimer revealed by the extra intensity from fourth Si atom. The latter show the flip induced by the electron beam.

1
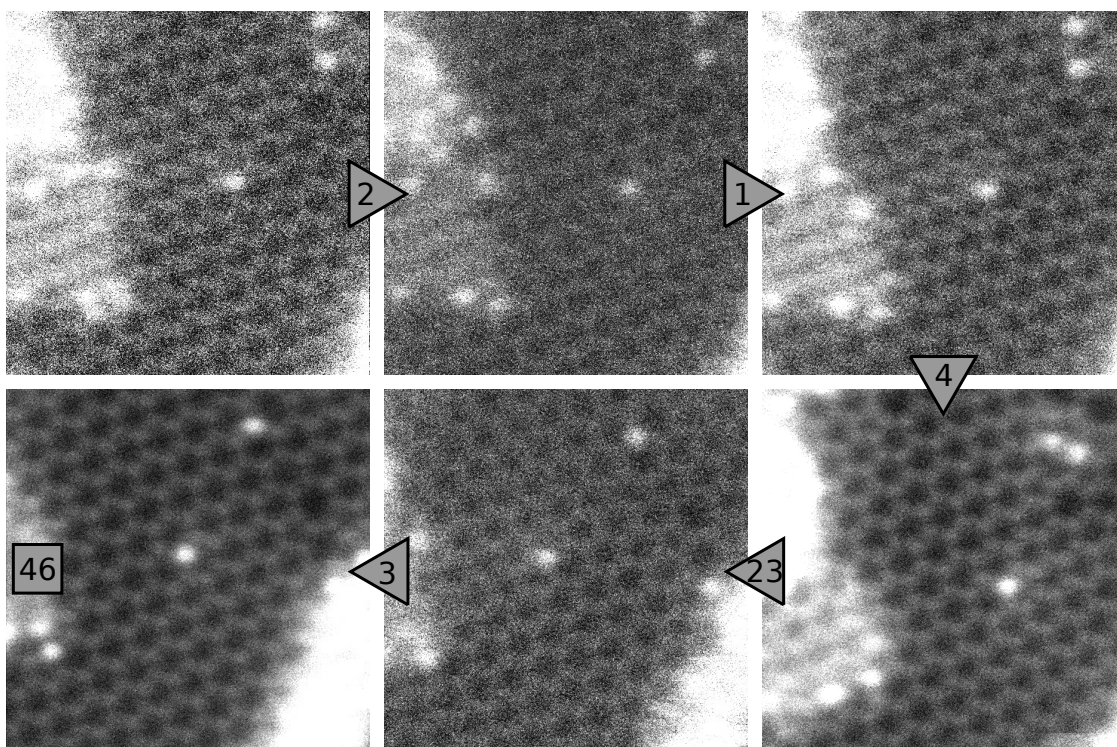
Supplementary Figure 1: Averaged STEM images of a Si substitution with a sample tilt of ca. 20 degrees. The sequence shows the flips of the Si atom through the graphene plane. The number corresponds the the number of frames which is required to occure the event.
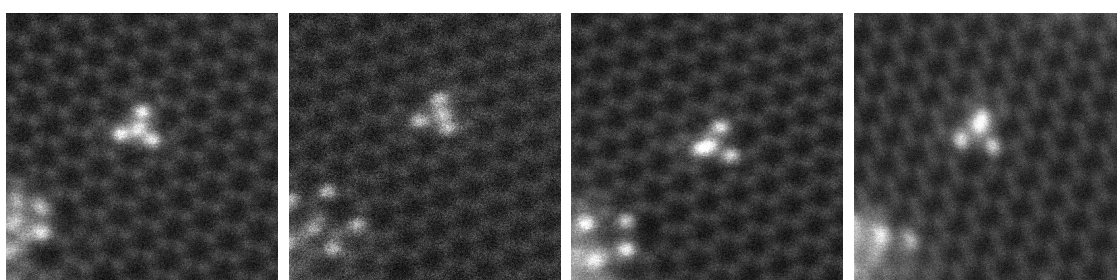
Supplementary Figure 2: Averaged STEM images of the Si tetramer with different sample tilts.

2

4.3 Paper III

Paper III uses STEM to analyze light elements in graphene, specifically nitrogen and oxygen impurities incorporated into the carbon lattice. Nitrogen and oxygen atoms were found to bond to their neighbors in a rich variety of configurations. For the most part, the study confirmed the textbook model for this system, which can now be displayed with direct images of actual atoms: Nitrogen atoms were incorporated into the carbon framework via two or three bonds, and most oxygen atoms had two bonds to the neighboring carbon atoms. However, also oxygen substitutions binding to three carbon neighbors were found (which were previously only known in a highly charged state, referred to as oxonium and difficult to stabilize in extended compounds).

Author contributions

The author of this thesis conducted the STEM measurements of GO, analyzed the configurations and drafted the figures and the manuscript. V.S. performed the sample preparation and participated in the STEM experiments. T.G., A.M. and M.T. performed the synthesis, STEM experiments, and analysis of N-doped graphene. M.R.A.M. and T.S. performed the DFT simulations. C.M. prepared alignments for the STEM instrument and supported the experiments. J.K. and J.C.M conceived and supervised the study.

Direct imaging of light-element impurities in graphene reveals triple-coordinated oxygen

Christoph Hofer [1,2,3]*, Viera Skákalová [1], Tobias Görlich[1], Mukesh Tripathi[1], Andreas Mittelberger [1], Clemens Mangler[1], Mohammad Reza Ahmadpour Monazam[1], Toma Susi [1], Jani Kotakoski [1] & Jannik C. Meyer [1,2,3]

Along with hydrogen, carbon, nitrogen and oxygen are the arguably most important elements for organic chemistry. Due to their rich variety of possible bonding configurations, they can form a staggering number of compounds. Here, we present a detailed analysis of nitrogen and oxygen bonding configurations in a defective carbon (graphene) lattice. Using aberration-corrected scanning transmission electron microscopy and single-atom electron energy loss spectroscopy, we directly imaged oxygen atoms in graphene oxide, as well as nitrogen atoms implanted into graphene. The collected data allows us to compare nitrogen and oxygen bonding configurations, showing clear differences between the two elements. As expected, nitrogen forms either two or three bonds with neighboring carbon atoms, with three bonds being the preferred configuration. Oxygen, by contrast, tends to bind with only two carbon atoms. Remarkably, however, triple-coordinated oxygen with three carbon neighbors is also observed, a configuration that is exceedingly rare in organic compounds.

[1] Faculty of Physics, University of Vienna, Boltzmanngasse 5, A-1090 Vienna, Austria. [2] Institute for Applied Physics, Eberhard Karls University of Tuebingen, Auf der Morgenstelle 10, D-72076 Tuebingen, Germany. [3] Natural and Medical Sciences Institute at the University of Tuebingen, Markwiesenstr. 55, D-72770 Reutlingen, Germany. *email: christoph.hofer@uni-tuebingen.de

Recent advances in transmission electron microscopy, in particular aberration correction, have enabled the study of low-dimensional materials at low electron energies with atomic resolution. In scanning transmission electron microscopy (STEM)[1], the contrast mechanism behind annular dark field images allows the identification of light elements (e.g. B, C, N, O) despite their very similar atomic number[2]. In aberration-corrected high-resolution transmission electron microscopy (HRTEM), however, these elements have an almost-identical contrast and their discrimination becomes difficult in particular when they are incorporated into irregular structures such as defects[3,4]. Atomic resolution images have revealed the bonding configurations of several types of impurities in light-element samples. For example, nitrogen dopants in graphene and carbon nanotubes have been revealed in several studies[5–9], boron dopants have been identified in graphene by STEM[8], and carbon and oxygen impurities have been revealed in monolayer hexagonal boron nitride[2]. Oxygen impurities in graphene are of high relevance due to their importance for the processing of graphene oxide (GO), and are likely to play a role, e.g. in the degradation of graphene in oxygen or in air at high temperatures. Despite efforts to quantify the functional groups in GO[10–15], the nature of oxygen binding to graphene is still not well understood. Although few HRTEM studies have revealed disorder and defects in graphene oxide[16–19], a direct visualization of oxygen atoms that includes their unambiguous chemical identification (e.g., via contrast in STEM or via electron energy loss spectroscopy, EELS) along with their bonding with a carbon matrix has not been achieved yet.

Here, we study a large number of oxygen impurities in samples of graphene oxide. The oxygen atoms are identified by their contrast in medium-angle annular dark field STEM images[2], and in several cases also by EELS. For comparison, we also prepared a graphene sample with nitrogen impurities by low-energy plasma and ion treatment (see the "Methods" section). In contrast to an earlier study[8], our samples are transferred under vacuum from implantation to STEM imaging, which prevents configurations with open bonds from being saturated with contamination. Our data set is large enough to carry out a statistical analysis of the different bonding configurations for oxygen and nitrogen. Moreover, we describe the dynamics of reduction observed under the electron beam for the case of oxygen.

Results

Configurations. Before discussing the observed atomic configurations, it must be pointed out that initial changes occur in the structure of graphene oxide already at relatively low doses, which makes it challenging if not impossible to capture the pristine structure in atomic resolution TEM or STEM images. In agreement with earlier findings[20], we observed changes in the EELS signal at doses between 10^3 and $10^6\,e^-\,\text{Å}^{-2}$ (Fig. 1a–d). We assume that functional groups which are attached to the basal plane, edges, or defects of graphene via relatively weak bonds (such as hydroxyl, carboxyl, epoxide, or ketone groups) are destroyed at these doses before an image could be obtained. Nevertheless, what remains after initial electron irradiation is a defective graphene sample, where numerous oxygen impurities are incorporated into a carbonaceous host structure. These structures, which are stable enough for STEM imaging and in some cases EELS, reveal a variety of bonding configurations for oxygen in an sp^2-bonded carbon system.

A high-magnification image where the defective carbon honeycomb lattice can be resolved is presented in Fig. 1e. While the regular graphene lattice dominates the area of the sample, a remarkably high density of defects with brighter impurity atoms

can be identified. By analyzing the intensities[2], most of these atoms can be assigned as oxygen. Figure 1f, g show the histogram of the intensities. We further confirmed the identity for some of the impurities by EELS (which in turn validates the intensity analysis). Due to a lower dose than that used in ref. [2] necessitated by the sample stability, a small fraction of the impurities cannot be uniquely assigned, e.g. where the tails between the nitrogen and oxygen intensity distribution overlap in the histogram (Fig. 1g). For example, the atom in Fig. 1c marked by the blue circle could—based on the intensity alone—be either nitrogen or oxygen. However, since the EELS signal of the GO samples shows no indication of nitrogen, we assume the impurity atom to be oxygen in such cases.

For the N-doped graphene, we classify the configurations in agreement with earlier literature into graphitic (substitution with three N–C bonds), pyridinic (two N–C bonds in a hexagon) and pyrrolic (two N–C bonds in a pentagon) configurations. Different oxygen and nitrogen configurations are shown in Fig. 2.

For the oxygen impurities, the conventional classification into different types of functional groups is not useful for describing the observed structures. Instead, we classify the oxygen configurations into three frequently observed types. The first, and surprisingly frequently observed, configuration consists of two oxygen atoms substituting two neighboring carbon atoms. An example of a STEM image of this configuration is shown in Fig. 2a. Graphitic substitutions are our second type of configuration (Fig. 2b). This is the only configuration in which oxygen binds with three carbon neighbors, similar to the oxygen impurities imaged in hexagonal boron nitride[2]. Our third class of configurations are oxygen atoms next to vacancies. Interestingly, they form defect reconstructions that are very similar to those in graphene without heteroatoms, except that one or two carbon atoms at the edge of a vacancy are replaced by oxygen. We label these defects in accordance with the carbon-only structures. In a 5–9 monovacancy (MV)[21], for example, a single oxygen replaces the carbon atom with only two bonds (Fig. 2c, first column) while the structure undergoes a distortion that looks like the Jahn–Teller distortion of a carbon-only vacancy. If two oxygen atoms are present, however, both remain two-coordinated and the bond at the pentagon remains open leading to a symmetric MV configuration (Fig. 2c, second column). Another prominent example is the divacancy (DV)[22], where two oxygen atoms can sit in the same pentagon of a 5-8-5 DV (third column of Fig. 2c). Also here, the two oxygen atoms do not form a bond and have a larger projected distance than the corresponding carbon atoms at the opposite pentagon. The 555–777 DV (fourth column) shows an interesting behavior when one carbon is replaced by an oxygen atom: Here, the oxygen only binds with two carbon atoms, breaking the three-fold symmetry. In a configuration where three carbon atoms are missing (last column of Fig. 2c), the oxygen atom binds with two carbon atoms building a "bridge". This appears very similar to a graphene trivacancy (TV). All of these configurations, except for the graphitic type, form an ether-like bond, i.e. an oxygen binding to two different carbon atoms.

A statistical analysis of the distribution of the configurations reveals that the oxygen pair is the most prominent one (Fig. 2e), whereas the graphitic substitution is the least frequent. In contrast, in our N-doped graphene sample, the pyrrolic configuration was the most favored one followed by the graphitic substitution. The occurrence of the pyridinic configuration is low in our case. It can be increased by ozone treatment during sample preparation[23], which we have not done. The difference of the bonding configurations of N and O in graphene can be highlighted by the distribution of their coordination numbers (Fig. 2f). The statistical analysis of our atomic resolution images
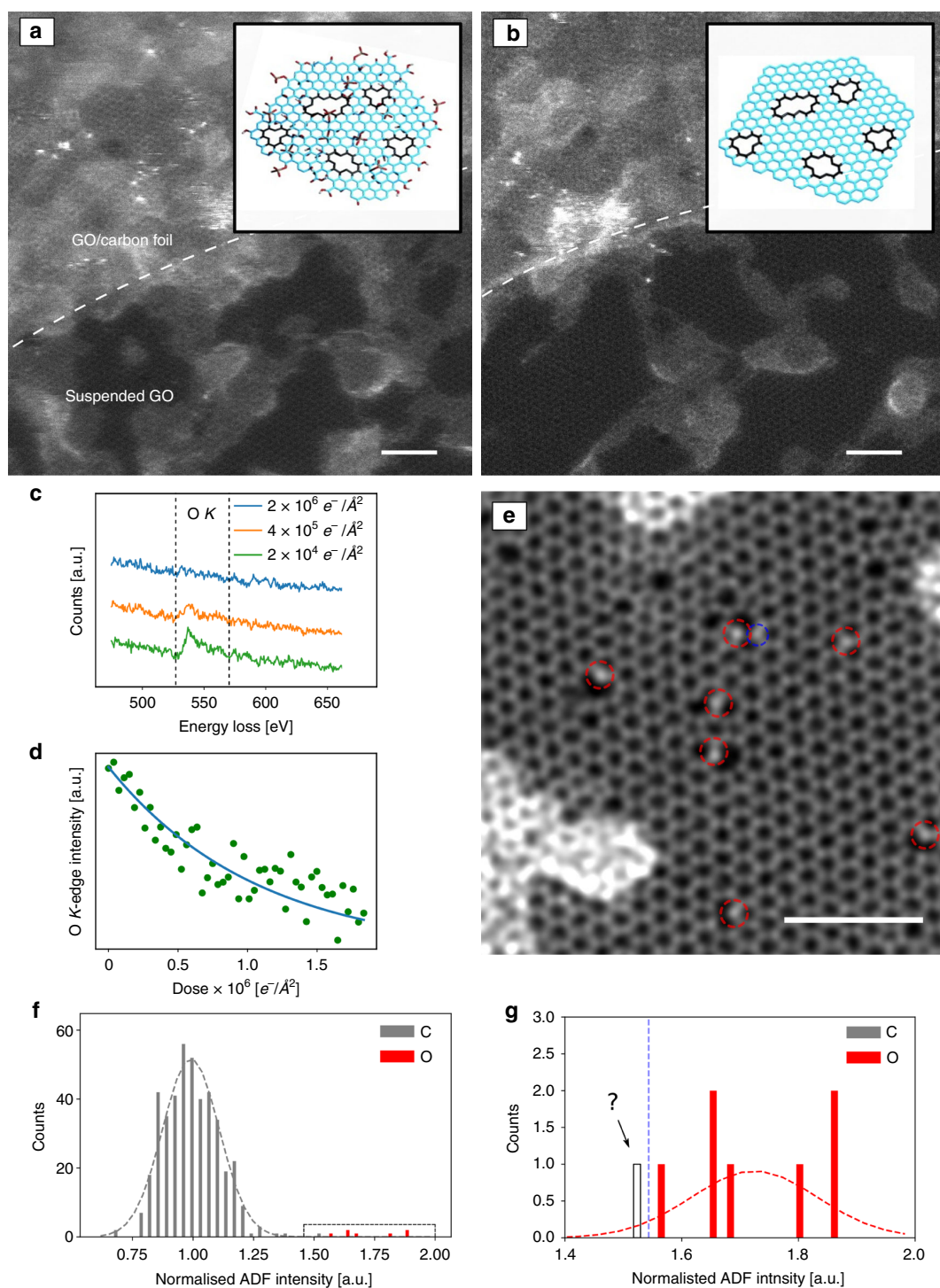
Fig. 1 Reduction of GO under the beam. Lower magnification (lattice resolution) STEM images: **a** initial and **b** after ~50 scans. Adsorbates shrink under observation, and the clean lattice area increases. The insets show a model with and without functional groups attached to the graphene sheet (reduced GO). The upper left section of the image contains the supporting carbon film. **c** EEL spectra after different electron doses showing the loss of the oxygen *K*-edge. **d** EEL intensity of the oxygen *K*-edge as a function of electron dose. **e** High magnification double-Gaussian filtered image where the graphene lattice with defects and impurities is resolved. The bright atoms (red dashed circles) can be identified as oxygen. The atom in the blue dashed circle is at the edge of the intensity distribution and might be either nitrogen or oxygen. **f** Histogram of the ADF intensities of carbon (gray) and oxygen atoms (red). **g** Magnified histogram of panel **f**. Insets in **a**, **b** are reprinted from ref. [10] with permission. Scale bars are 2 nm
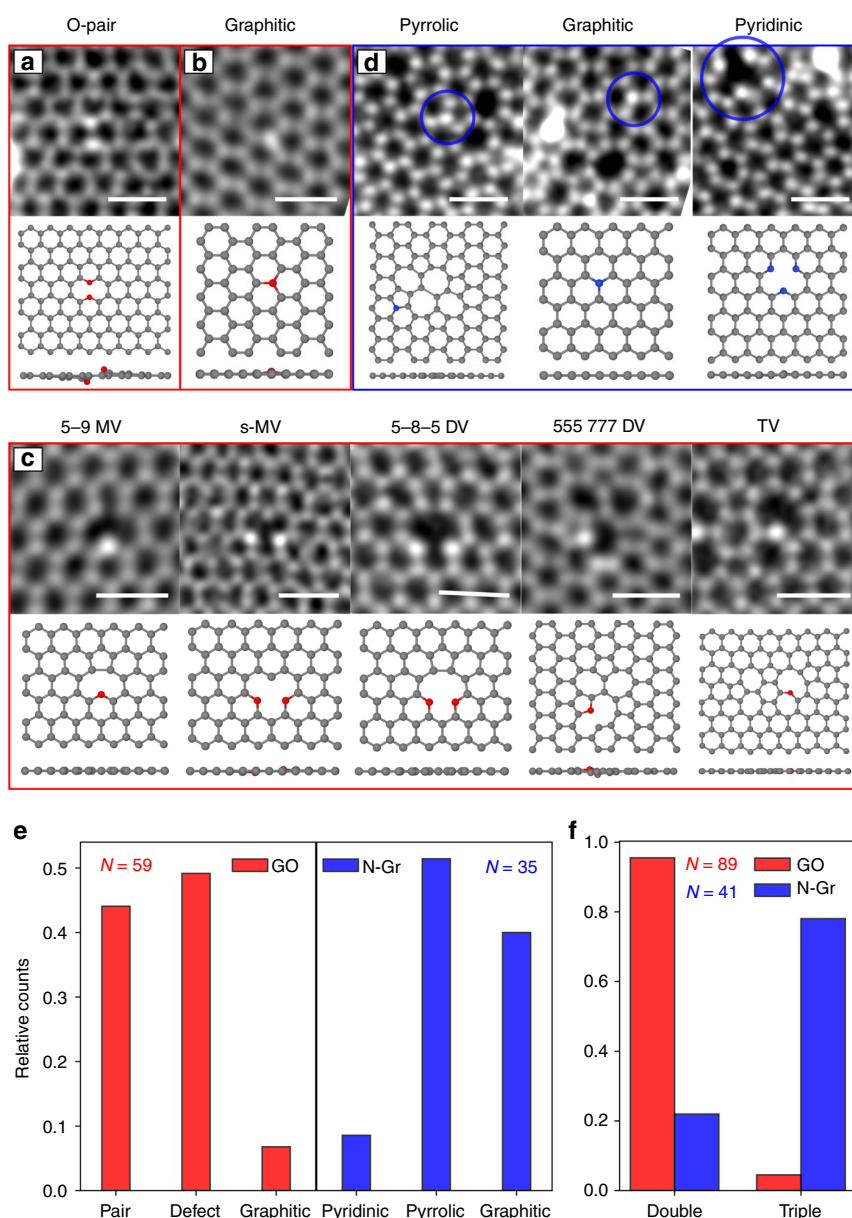
Fig. 2 STEM images of different configurations of oxygen and nitrogen atoms in graphene. **a** Oxygen pair. **b** Graphitic substitution by oxygen. **c** Oxygen atoms within vacancies. **d** Nitrogen-doped graphene configurations. **e** Distribution of the different configurations in GO (red) and N-doped graphene (blue). **f** Distribution of double-coordinated and triple-coordinated heteroatoms in GO (red) and N-doped graphene (blue). N shows the total number of heteroatoms of each sample (note that some configurations contain multiple heteroatoms). Scale bars are 0.5 nm

directly confirms that oxygen prefers two bonds while nitrogen prefers three bonds. This is in agreement with the different electronic configuration of these elements, and hence different preferences for forming chemical bonds with carbon.

To analyze their structural properties, we performed density functional theory (DFT) calculations for each configuration. The obtained relaxed models are shown below the STEM images in Fig. 2. In some cases, we find clear differences in the structural relaxation for oxygen in comparison to nitrogen. For example, the relaxed structure of the 555–777 DV (Fig. 2c, fourth column) shows a large projected distance of the oxygen atom to one of its three neighbors, breaking the three-fold symmetry of this configuration. Clearly, the oxygen in this case binds only with

two carbon atoms. However, a nitrogen atom in the same position results in a highly symmetric configuration with three neighbors close to the impurity (Supplementary Fig. 2). For the double-oxygen site (Fig. 2a), the two oxygen atoms do not bind but stick out of the graphene plane in opposite directions, with a projected distance that is significantly larger than the carbon–carbon bond in graphene. This is not the case for a simulated double-nitrogen structure (see Supplementary Discussion). All other considered configurations have very similar structural properties for both nitrogen and oxygen impurities, except for small out-of-plane displacements.

The energies of the relaxed configurations with the heteroatoms incorporated in the lattice (E_{in}) for both, nitrogen and

oxygen, were also obtained by DFT. We calculated the sum of the energies ($E_{out} + E_{isolated}$) when the heteroatoms are released from the lattice (after relaxation) and the isolated atoms (half of N_2 or O_2). The difference $E_{in} - (E_{out} + E_{isolated})$ is referred as binding energy and is lower (meaning higher stability) for all N configurations. This is in agreement with the observed higher stability of N dopants in graphene. All calculated energies are listed in Supplementary Table 2. The binding energies are negative in all cases, which means that the structures are stable with respect to forming a carbon-only vacancy plus isolated O or N.

Dynamics. The oxygen substitutions are sputtered after a dose with a geometrical mean of $5 \times 10^5 \, e^- \, Å^{-2}$ and replaced by a carbon atom, whereas nitrogen substitutions can withstand orders of magnitude higher doses[24] (cf. Fig. 3a–c). To understand this difference, we performed DFT-based molecular dynamics calculations (see the "Methods" section). The threshold energy for removing an oxygen atom from the lattice is 10.3 eV, and the threshold for removing the neighboring carbon is 15.0 eV. This energy is almost 2/3 of the calculated 22.0 eV threshold kinetic energy for a carbon in pristine graphene and also significantly lower than for nitrogen in graphene (19.09 eV)[25]. Indeed, graphitic nitrogen in graphene was found to be extremely stable

under 60 or 80 kV electron irradiation, such that the atomic structure of the dopant site is more likely to be changed by displacing a neighboring carbon atom before the dopant atom itself is sputtered under electron irradiation[25]. Hence, the observed clear difference in the stability under the beam between graphitic oxygen and nitrogen impurities is in agreement with the calculations. We further performed intensity analysis of another STEM image, where multiple oxygen pair configurations, as well as a graphitic configuration are present (see Fig. 3d). The histogram of the atom intensities (Fig. 3e) shows that the intensity of the graphitic configuration is clearly within the distribution of oxygen.

As mentioned above, we often observed the neighboring double-oxygen configuration as shown in Fig. 4a. Calculations[26] and experiments[27] show that directly neighboring nitrogen atoms are energetically unfavorable, while our experiments indicate that in the case of oxygen such a configuration is stable. Interesting dynamics can be observed when one oxygen atom is sputtered and a MV configuration with a single oxygen atom is left behind (Fig. 4b, c): During imaging, the oxygen atom jumps frequently to the opposite vacancy site. Similar dynamics were reported in a N-doped sample[5]. The number of images between such events spans the range from 1 to 15 with a dose of ca. $6 \times 10^5 \, e^- \, Å^{-2}$ per image. After a long electron exposure, the second O atom can be removed, leaving behind a DV (Fig. 4d), which is also highly dynamic[22]. A video of this process is shown in the Supplementary Discussion.

Another example of dynamics is shown in Fig. 4f. In this case, two oxygen atoms were found in a MV. After a few images, one carbon is sputtered and a 5-8-5 DV with two oxygen atoms forms (cf. Fig. 2c, middle column).

Then, after a few scans, one oxygen is removed and after some intermediate (not clearly observed) steps, a structure with two defects, a MV and a 555–777 DV, is formed. These observations indicate that, similar to all-carbon defects in graphene, also carbon–oxygen configurations can undergo beam-induced bond rotations and thereby migrate in the lattice[22]. Figure 4g shows the 5-8-5 DV in two distinct, but equivalent states.

Discussion

Oxygen with three carbon neighbors appears as a surprise, because it seems to contradict the textbook concept of oxygen forming two bonds (or one double bond), while nitrogen forms three, and carbon up to four covalent bonds. Within the known organic compounds, trivalent oxygen only appears in a charged state, referred to as oxonium, and is difficult to stabilize in extended compounds[28]. Here, the oxygen with three carbon neighbors is found in an extended organic matrix, and the fact that it survives sufficient dose of high-energy electrons for recording several high-resolution images means that it must have a remarkable stability.

With respect to the structure of GO, our results indicate that oxygen atoms incorporated into the graphene lattice or integrated into small defects within in the graphene plane could play an important role among the structural configurations in GO or reduced GO. In particular, the high stability of these configurations means that they would be difficult to remove, e.g. by thermal annealing. Indeed, several of our configurations appear to have been predicted by simulations of oxidation and annealing of graphene (Fig. 2 of ref.[29]), and formed under simulated annealing conditions where most functional groups attached to the basal plane were removed.

In conclusion, we have shown a large variety of bonding configurations of nitrogen and oxygen atoms in a carbon matrix

Fig. 3 Graphitic oxygen substitution. **a** Unprocessed STEM image of a graphitic oxygen substitution in graphene. **b** Oxygen atom is sputtered after four frames, leaving a vacancy. **c** Pristine graphene lattice after the vacancy gets refilled by a carbon atom. **d** Low-magnification image of the GO sample, where multiple pair configurations and a graphitic substitution is present. **e** Histogram of intensity distribution of atoms in panel **d**. Scale bars in panel **a–c** and in panel **d** are 0.25 and 1 nm, respectively

Fig. 4 In situ oxygen reduction and dynamics in GO. **a** STEM image of the oxygen pair configuration. **b**, **c** One oxygen is released after several scans, creating a vacancy beside the oxygen atom. The oxygen atom jumps frequently to the opposite equivalent site. **d** Second oxygen is knocked out after several scans creating a divacancy. **e** EEL spectrum of a double-O configuration, which converted into single-O during spectrum acquisition (total dose: ca. 2×10^{10} e$^-$ Å^{-1}). **f** Reduction process of oxygen. **g** Rotation of the 5-8-5 DV with two oxygen atoms. Scale bar is 0.5 nm

via atomic resolution imaging. For the first time, individual oxygen impurities were clearly identified, and a statistical analysis for both oxygen-containing and nitrogen-containing defects was presented. By and large, the preference of nitrogen for three bonds, versus the preference of oxygen for two bonds, is conf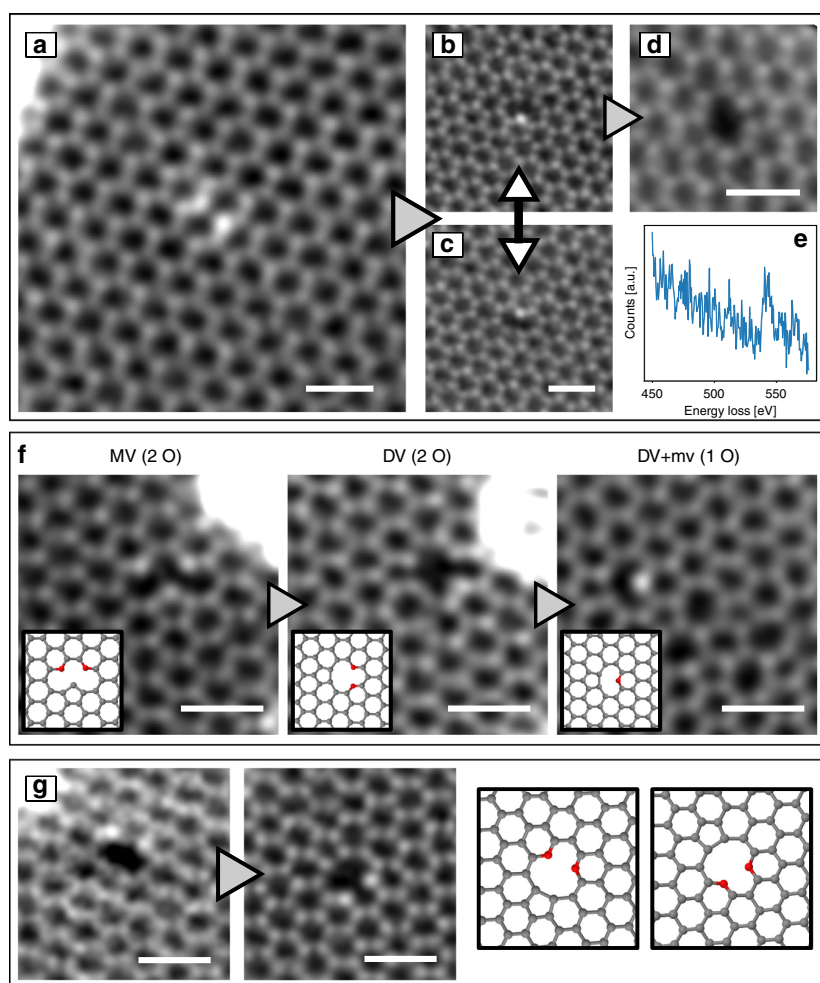irmed. An oxygen pair configuration is revealed to be a very frequent configuration in GO, followed by different types of double-coordinated oxygen atoms at the edges of vacancies. As a remarkable minority, symmetric, graphitic substitutions of oxygen binding to three carbon neighbors in graphene were found. Further, we presented electron-beam-induced reduction dynamics. Overall, we find that the structural features of the defects are similar for all-carbon defects compared to nitrogen-containing or oxygen-containing defects in the same configuration, while differences in the bond lengths or stability are nevertheless detectable.

Methods

Sample preparation. GO is usually prepared from graphite oxide[30–32] by mixing graphite powder into an acid solution, which leads to oxidation. In an improved method, the temperature during oxidation is kept low in order to suppress the extensive formation of CO_2, which therefore improves the quality of the sample[33]. Water dispersion of graphene oxide was received from the company Danubia

NanoTech, Ltd. The oxidation method of graphitic powder and subsequent exfoliation were developed with a goal to preserve the long-range structural order in the graphene oxide flakes exfoliated down to the single-atom thickness. Water dispersion of GO was significantly diluted (ca. 1:100). A TEM grid was then vertically dipped into the dispersion for one minute and dried in air afterwards.

Nitrogen-doped samples prepared for comparison were made by irradiating graphene on TEM grids (obtained from Graphenea) with 50 eV nitrogen ions[26]. The plasma irradiation was carried out in a target chamber that is directly connected to the Nion microscope via a UHV transfer system[34]. The sample was irradiated for 16 min at a pressure of ca. 3×10^{-6} mbar, resulting in a total ion dose of 4 ions nm^{-2}. During irradiation, the sample was heated with a laser (270 mW) in order to reduce contamination. The irradiation treatment in the vacuum system is very similar to the preparation in ref. [34] except that we used nitrogen instead of argon. As a result, we find numerous defects where open bonds can still be observed, e.g., the pyridinic nitrogen configuration (which would likely be covered with contamination if the sample were transferred through air) without post-annealing the sample[5].

Electron microscopy. STEM experiments were conducted using a Nion Ultra-STEM100, operated at 60 kV. Typically, our atomic-resolution images were recorded with 512 × 512 pixels for a field of view of 6–8 nm and dwell time of 16 µm per pixel using the medium angle annular dark field (MAADF) detector with an angular range of 60–200 mrad. The probe current was ~20 pA and the beam (semi-)convergence angle was 30 mrad. Where appropriate if the structure did not change, a few (2–5) experimental images were averaged in order to increase the signal-to-noise ratio.

Intensity analysis. The histograms show integrated atom intensities of the double-Gaussian processed STEM images. The parameters for the filter are similar as in ref. [2] so that the maximum of the double-Gaussian function is between the first two orders of the graphene peaks in the reciprocal space. The width of the Gaussian fit of the carbon peak is assumed to be the same as for the intensity distribution of the other elements.

Density functional theory. We used DFT as implemented in the Vienna ab initio simulation package (VASP)[35] within the generalized gradient approximation of Perdew, Burke, and Ernzernhof (PBE) for exchange and correlation[36]. Projector-augmented wave (PAW) potentials[37] were used to describe the core electrons. The kinetic energy cutoff was 700 eV. In case of oxygen impurities, a spin-polarized density-functional method was used. Depending on the defect size and number of impurity atoms, different supercells were selected for modeling. The smallest one was a $5 \times 5 \times 1$ supercell with 50 atoms for the nitrogen graphitic impurity, whereas a $8 \times 8 \times 1$ supercell containing 128 atoms was used for the TV defect. For all defect structures, a Γ-centered k-point sampling was used for the Brillouin-zone integration. The k-point meshes were selected to correspond to $36 \times 36 \times 1$ points for the unit cell of graphene. The structures were fully optimized using the damped molecular dynamics method until the residual forces were smaller than 0.005 eV Å^{-1}. Due to the size of the defects and existing impurities, special care was devoted to minimize the external pressure or strain on the supercells calculated from traces of the stress tensor. The total energies were calculated based on supercell sizes with minimum external pressure.

To calculate the displacement threshold energy, we carred out DFT/MD calculations at 300 K using the Langvin NVT thermostat. In these simulations, appropriate velocity is given to the oxygen atom and the simulation is run with a 0.5 fs time step for 100 fs. The calculation is then repeated for the neighboring carbon atom.

Data availability

The full STEM data on which the statistical analysis of the configurations are based are available on figshare with identifier https://doi.org/10.6084/m9.figshare.9205367.v3[38]. Although the data is classified in different sub-folders, each image might contain multiple configurations.

References

1. Krivanek, O., Dellby, N. & Lupini, A. Towards sub-Å electron beams. *Ultramicroscopy* **78**, 1–11 (1999).
2. Krivanek, O. L. et al. Atom-by-atom structural and chemical analysis by annular dark-field electron microscopy. *Nature* **464**, 571–574 (2010).
3. Meyer, J. C. et al. Experimental analysis of charge redistribution due to chemical bonding by high-resolution transmission electron microscopy. *Nat. Mater.* **10**, 209–215 (2011).
4. Kurasch, S., Meyer, J. C., Künzel, D., Groß, A. & Kaiser, U. Simulation of bonding effects in HRTEM images of light element materials. *Beilstein J. Nanotechnol.* **2**, 394–404 (2011).
5. Lin, Y.-C. et al. Structural and chemical dynamics of pyridinic-nitrogen defects in graphene. *Nano. Lett.* **15**, 7408–7413 (2015).
6. Warner, J. H., Lin, Y.-C., He, K., Koshino, M. & Suenaga, K. Stability and spectroscopy of single nitrogen dopants in graphene at elevated temperatures. *ACS Nano* **8**, 11806–11815 (2014).
7. Nicholls, R. J. et al. Probing the bonding in nitrogen-doped graphene using electron energy loss spectroscopy. *ACS Nano* **7**, 7145–7150 (2013).
8. Bangert, U. et al. Ion implantation of graphenetoward IC compatible technologies. *Nano. Lett.* **13**, 4902–4907 (2013).
9. Arenal, R. et al. Atomic configuration of nitrogen-doped single-walled carbon nanotubes. *Nano. Lett.* **14**, 5509–5516 (2014).
10. Eigler, S. & Hirsch, A. Chemistry with graphene and graphene oxide-challenges for synthetic chemists. *Angew. Chem. Int. Ed.* **53**, 7720–7738 (2014).
11. Hofmann, U. & König, E. Untersuchungen über Graphitoxyd. *Z. Anorg. Allg. Chem.* **234**, 311–336 (1937).
12. Brodie, B. C. On the atomic weight of graphite. *Philos. Trans. R. Soc. Lond.* **149**, 249–259 (1859).
13. Dreyer, D. R., Todd, A. D. & Bielawski, C. W. Harnessing the chemistry of graphene oxide. *Chem. Soc. Rev.* **43**, 5288 (2014).
14. Eng, A. Y. S., Chua, C. K. & Pumera, M. Refinements to the structure of graphite oxide: absolute quantification of functional groups via selective labelling. *Nanoscale* **7**, 20256–20266 (2015).
15. Skákalová, V. et al. Chemical oxidation of graphite: evolution of the structure and properties. *J. Phys. Chem. C* **122**, 929–935 (2018).
16. Erickson, K. et al. Determination of the local chemical structure of graphene oxide and reduced graphene oxide. *Adv. Mater.* **22**, 4467–4472 (2010).
17. Wilson, N. R. et al. Graphene oxide: structural analysis and application as a highly transparent support for electron microscopy. *ACS Nano* **3**, 2547–2556 (2009).
18. Gomez-Navarro, C. et al. Atomic structure of reduced graphene oxide. *Nano Lett.* **10**, 1144–1148 (2010).
19. Pacilé, D. et al. Electronic properties and atomic structure of graphene oxide membranes. *Carbon N. Y.* **49**, 966–972 (2011).
20. Tararan, A., Zobelli, A., Benito, A. M., Maser, W. K. & Stéphan, O. Revisiting graphene oxide chemistry via spatially-resolved electron energy loss spectroscopy. *Chem. Mater.* **28**, 3741–3748 (2016).
21. Robertson, A. W. et al. Structural reconstruction of the graphene monovacancy. *ACS Nano* **7**, 4495–4502 (2013).
22. Kotakoski, J., Mangler, C. & Meyer, J. C. Imaging atomic-level random walk of a point defect in graphene. *Nat. Commun.* **5**, 3991 (2014).
23. Lin, Y.-C., Teng, P.-Y., Chiu, P.-W. & Suenaga, K. Exploring the single atom spin state by electron spectroscopy. *Phys. Rev. Lett.* **115**, 206803 (2015).
24. Susi, T. et al. Towards atomically precise manipulation of 2D nanostructures in the electron microscope. *2D Mater.* **4**, 042004 (2017).
25. Susi, T. et al. Atomistic description of electron beam damage in nitrogen-doped graphene and single-walled carbon nanotubes. *ACS Nano* **6**, 8837–8846 (2012).
26. Åhlgren, E. H., Kotakoski, J. & Krasheninnikov, A. V. Atomistic simulations of the implantation of low-energy boron and nitrogen ions into graphene. *Phys. Rev. B* **83**, 115424 (2011).
27. Lv, R. et al. Nitrogen-doped graphene: beyond single substitution and enhanced molecular sensing. *Sci. Rep.* **2**, 586 (2012).
28. Mascal, M., Hafezi, N., Meher, N. K. & Fettinger, J. C. Oxatriquinane and oxatriquinacene: extraordinary oxonium ions. *J. Am. Chem. Soc.* **130**, 13532–13533 (2008).
29. Lin, L.-C. & Grossman, J. C. Atomistic understandings of reduced graphene oxide as an ultrathin-film nanoporous membrane for separations. *Nat. Commun.* **6**, 8335 (2015).
30. Zhu, Y. et al. Graphene and graphene oxide: synthesis, properties, and applications. *Adv. Mater.* **22**, 3906–3924 (2010).
31. Hummers, W. S. & Offeman, R. E. Preparation of graphitic oxide. *J. Am. Chem. Soc.* **80**, 1339–1339 (1958).
32. Zaaba, N. et al. Synthesis of graphene oxide using modified hummers method: solvent influence. *Procedia Eng.* **184**, 469–477 (2017).
33. Eigler, S. et al. Wet chemical synthesis of graphene. *Adv. Mater.* **25**, 3583–3587 (2013).
34. Inani, H. et al. Silicon substitution in nanotubes and graphene via intermittent vacancies. *J. Phys. Chem. C* **123**, 13136–13140 (2019).
35. Kresse, G. & Hafner, J. Ab initio molecular dynamics for liquid metals. *Phys. Rev. B* **47**, 558–561 (1993).
36. Perdew, J. P., Burke, K. & Ernzerhof, M. Generalized gradient approximation made simple. *Phys. Rev. Lett.* **77**, 3865–3868 (1996).
37. Kresse, G. & Joubert, D. From ultrasoft pseudopotentials to the projector augmented-wave method. *Phys. Rev. B* **59**, 1758–1775 (1999).
38. Hofer, C. et al. Raw data of graphene oxide and N-irradiated graphene. *figshare.* https://doi.org/10.6084/m9.figshare.9205367.v3 (2019).

Author contributions

C.H. performed the STEM experiments, analysis of GO, and drafted the figures and the manuscript. V.S. prepared GO samples and participated in STEM measurements. T.G., A.M. and M.T. performed the synthesis, STEM experiments, and analysis of N-doped graphene. M.R.A.M. and T.S. performed the DFT simulations. C.M. prepared alignments for the STEM instrument and supported the experiments. J.K. and J.C.M conceived and supervised the study.

Competing interests

The authors declare no competing interests.

Additional information

Direct imaging of light-element impurities in graphene reveals triple-coordinated oxygen

Hofer et. al

Supplementary Discussion

DFT calculations

We used DFT calculations to analyse the differences in structural properties when nitrogen and oxygen are incorporated into graphene. The relaxed models are shown in Supplementary Figure 1. The projected interatomic distances and out-of-plane distances are listed in Supplementary Table 1. Significant differences in the projected positions occur for the pair configuration and the 555-777 DV. In the first case, the two oxygen atoms do not form a bond and stick out of the graphene plane in opposite directions. Their projected distance is larger than the interatomic distance in graphene or the distance between two neighboring nitrogen substitutions. Supplementary Figure 2a compares the experimental data with the projected positions of the pair configuration with oxygen (red atoms) and nitrogen (blue atoms). As clearly visible from the magnified overlay of the model and the STEM image, only the relaxed oxygen configuration fits to the experiment. The same analysis can by applied to the 555-777 DV (Supplementary Figure 2b), where the difference is even larger. Also here, the relaxed configuration with the oxygen atom fits to the STEM image. The other configurations are very similar, except for small variations in the out-of-plane direction, which cannot be distinguished in the projected STEM images.

Supplementary Table 2 shows the energy of the relaxed configurations with the heteroatoms incorporated in the lattice for both, nitrogen and oxygen (E_{in}), the sum of the energies ($E_{out} + E_{isolated}$) when the heteroatoms are released from the lattice (after relaxation) and the isolated

Configurations	Oxygen			Nitrogen		
	r_1 [pm]	r_2 [pm]	z [pm]	r_1 [pm]	r_2 [pm]	z [pm]
Pair	123	186	65	141	145	0
Graphitic	149	-	20	141	-	0
5-9 MV	135	-	1	132	-	0
s-MV	136	264	13	135	266	0
5-8-5 DV	136	242	0	132	248	13
555-777 DV	138	206	22	145	145	0
TV	133	138	3	131	134	0

Supplementary Table 1: Projected interatomic distances and out-of-plane distances of different configurations with oxygen and nitrogen as heteroatoms in graphene. Definitions of r_1 and r_2 are in SFig. 1.

atoms (the half of N_2 or O_2). The difference $E_{in} - (E_{out} + E_{isolated})$ is referred as binding energy and the difference between the binding energies is shown in the last column of the table.

Configurations	Oxygen			Nitrogen			
	E_{in}	$E_{out} + E_{iso}$	E_{bind}	E_{in}	$E_{out} + E_{iso}$	E_{bind}	E_{diff}
Pair	-1175.47	-1162.30	-13.17	-1179.37	-1163.50	-15.87	2.69
Graphitic	-295.99	-280.66	-8.08	-294.20	-281.87	-12.33	4.25
5-9 MV	-649.07	-642.43	-6.65	-650.48	-643.63	-6.85	0.20
s-MV	-645.68	-631.19	-14.49	-650.015	-632.39	-17.62	3.13
5-8-5 DV	-636.31	-622.88	-13.44	-639.87	-624.08	-15.79	2.35
555-777 DV	-857.16	-853.34	-3.82	-862.22	-854.54	-7.68	3.86
TV	-1144.03	-1137.76	-6.27	-1145.59	-1138.97	-6.62	0.35

Supplementary Table 2: Total energy of each configuration in eV when the heteroatom is in the lattice (E_{in}), when the heteroatom is out of the lattice plus the isolated energy ($E_{out} + E_{iso}$), its difference (E_{bind}) and the difference between the binding energies $E_{diff} = E_{bind,O} - E_{bind,N}$
.

2

STEM image sequences

Video1 is a sequence of STEM images that shows the reduction of the oxygen pair configuration (cf. main text).
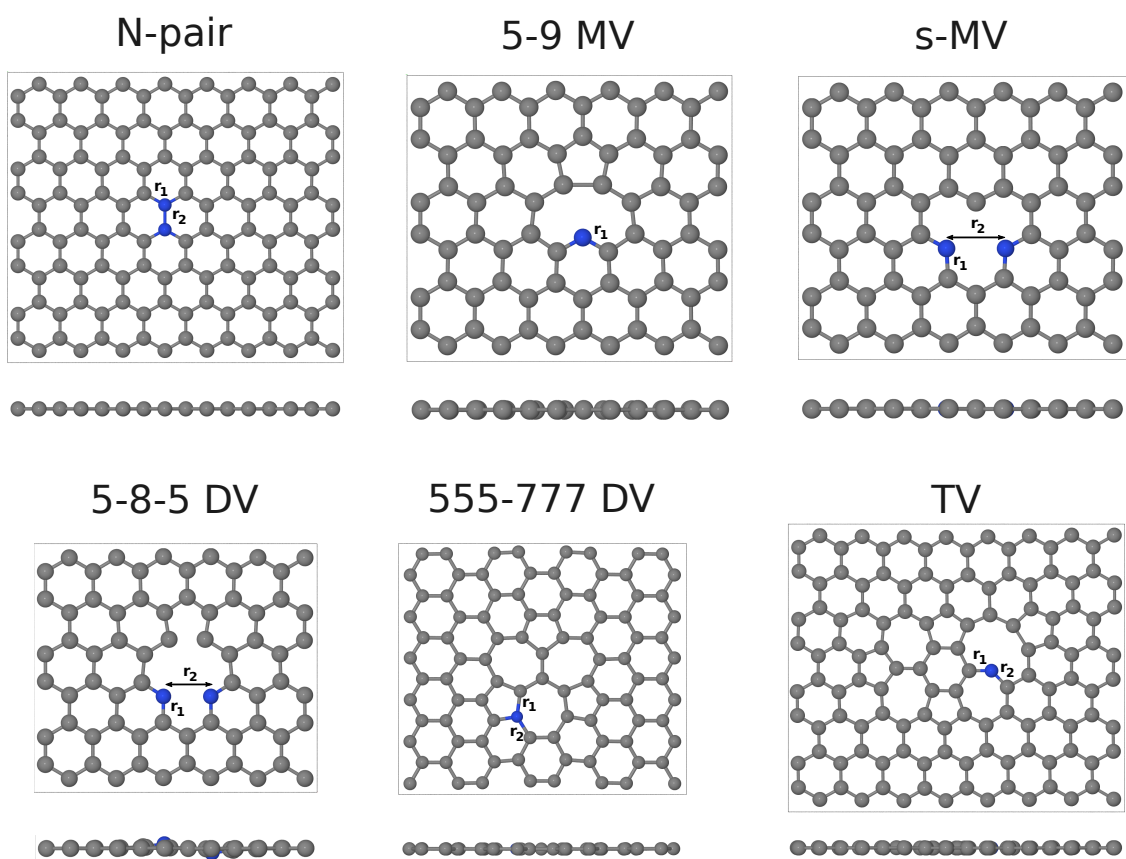
Supplementary Figure 1: Relaxed models for each impurity configuration with nitrogen instead of oxygen.
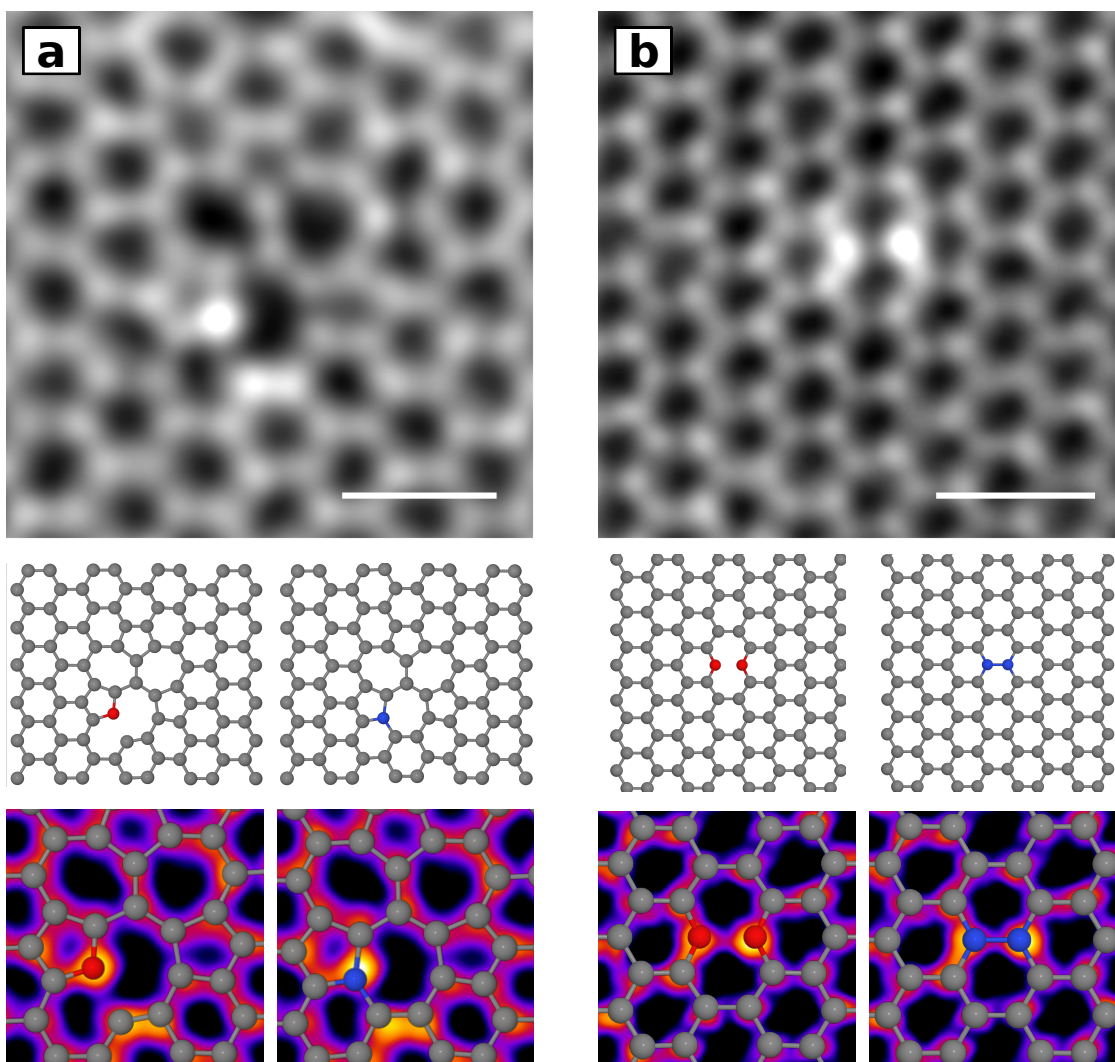
Supplementary Figure 2: Filtered STEM images of (a) the 555-777 DV and (b) the pair configuration. The middle row shows the top view of the relaxed model using oxygen or nitrogen as heteroatoms, respectively. The bottom row shows an overlay of the image from the oxygen sample and the model with oxygen or nitrogen. In both cases, the simulated oxygen configuration matches the experimental image.

5

4.4 Paper IV

Paper IV applies the reconstruction to a mixed-dimensional Van-der-Waals heterostructure. In this case, carbon nanotubes on graphene are analysed by STEM. Applying the reconstruction method to the underlying graphene (where every atom can be easily resolved) reveals deformations of the graphene induced by the interaction of the two structures. The reconstructions excellently match the computational relaxed heterostructures.

Author contributions

The author of this thesis participated in the STEM measurements and carried out the 3D reconstruction. The other authors conducted the rest of the study.

ACSNANO

ARTICLE

Atomic-Scale Deformations at the Interface of a Mixed-Dimensional van der Waals Heterostructure

Kimmo Mustonen,*,[†] Aqeel Hussain,[‡] Christoph Hofer,[†] Mohammad R. A. Monazam,[†] Rasim Mirzayev,[†] Kenan Elibol,[†] Patrik Laiho,[‡] Clemens Mangler,[†] Hua Jiang,[‡] Toma Susi,[†] Esko I. Kauppinen,[‡] Jani Kotakoski,[†] and Jannik C. Meyer*,[†]

[†]University of Vienna, Faculty of Physics, 1090 Vienna, Austria
[‡]Aalto University School of Science, Department of Applied Physics, P.O. Box 15100, FI-00076 Aalto, Finland

S Supporting Information

ABSTRACT: Molecular self-assembly due to chemical interactions is the basis of bottom-up nanofabrication, whereas weaker intermolecular forces dominate on the scale of macromolecules. Recent advances in synthesis and characterization have brought increasing attention to two- and mixed-dimensional heterostructures, and it has been recognized that van der Waals (vdW) forces within the structure may have a significant impact on their morphology. Here, we suspend single-walled carbon nanotubes (SWCNTs) on graphene to create a model system for the study of a 1D−2D molecular interface through atomic-resolution scanning transmission electron microscopy observations. When brought into contact, the radial deformation of SWCNTs and the emergence of long-range linear grooves in graphene revealed by the three-dimensional reconstruction of the heterostructure are observed. These topographic features are strain-correlated but show no sensitivity to carbon nanotube helicity, electronic structure, or stacking order. Finally, despite the random deposition of the nanotubes, we show that the competition between strain and vdW forces results in aligned carbon−carbon interfaces spanning hundreds of nanometers.

KEYWORDS: *carbon nanotube, graphene, scanning transmission electron microscopy, elasticity, interfacing*
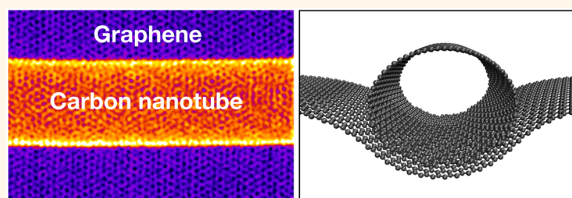
Building on enormous advances in graphene research, interest has recently shifted to the creation of so-called van der Waals heterostructures (vdWHs). These typically combine graphene and other two-[1] or lower-dimensional[2,3] molecules into vertical stacks. The principal idea of this concept is to preserve the covalent bonding structure of the molecules that interact with each other mainly through van der Waals (vdW) forces while the electronic and plasmonic coupling between the layers remains relatively strong and enables the creation of functional (meta)materials.[1,3−7] However, regardless of the nominally weak vdW interaction, the lattice mismatches in these structures can result in significant morphological changes.[8,9]

The creation of exclusively 2D heterostructures has proven relatively straightforward, either by directly placing two sheets into contact[1] or via epitaxial growth.[10−14] Furthermore, the energetic tendency to maximize the contact area seems to drive self-cleaning within the vdW gap,[15] enabling atomically pure interfaces. However, it is much more challenging to obtain sufficiently clean, ordered, and thin layers of lower-dimensional structures owing to their higher chemical reactivity. This in turn

has hindered the efforts to experimentally study fundamental phenomena governing the interactions between the layers. We recently studied monolayers of C_{60} molecules trapped in between two graphene sheets[16] in a higher-dimensional analogue of carbon pea pods.[17] In this mixed-dimensional heterostructure, we observed the deformation of the graphene sheets only at the edges of C_{60} molecular layers.

Here, to create a 1D−2D molecular interface, we have dry-deposited single-walled carbon nanotubes (SWCNTs) on suspended monolayer graphene. Using scanning transmission electron microscopy (STEM), we study how they stack onto graphene and how the adsorbtion changes the morphology of both materials. Unlike most other molecules of this class, SWCNTs are hollow tubes that may deform when interacting with substrates,[18−20] and although their covalent structure remains intact, this is expected to affect their transport
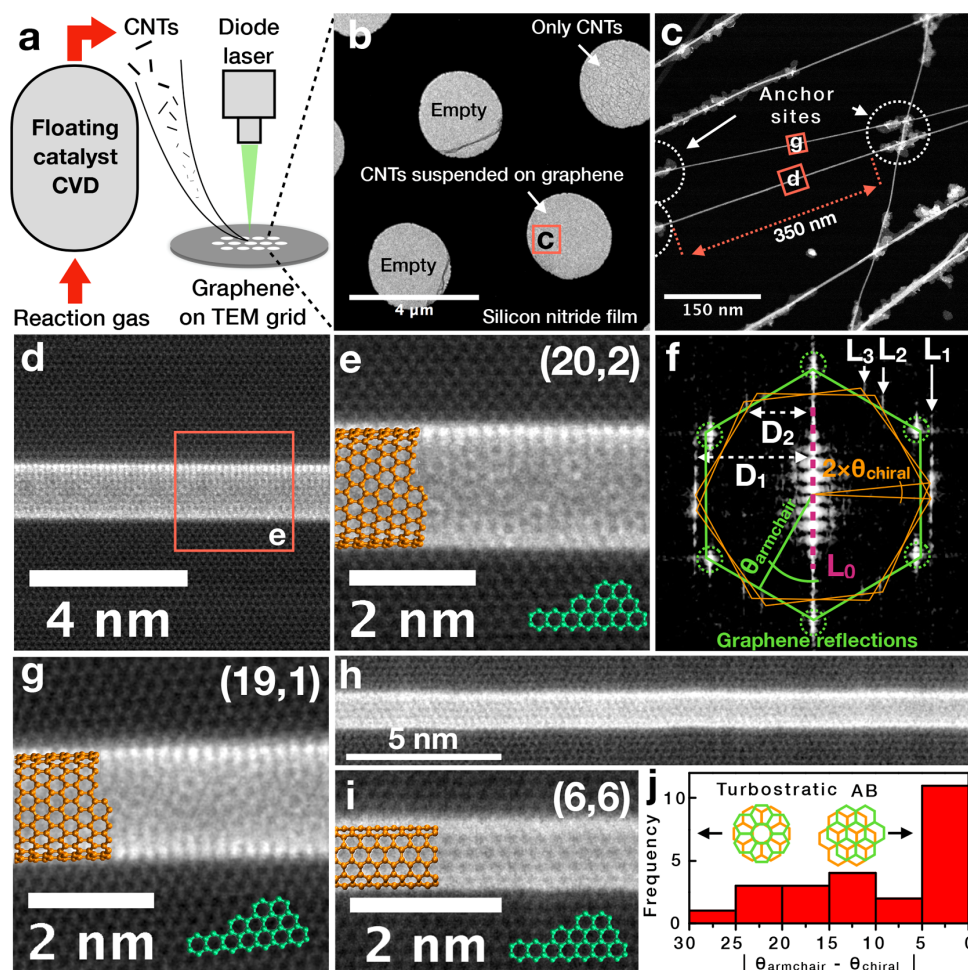
Figure 1. SWCNT−graphene interface. (a) Heterostructure fabrication by the thermophoretic deposition[29] of floating catalyst CVD SWCNTs[27,28] on graphene and laser cleaning in vacuum.[30] (b) Bright-field overview of a typical laser-cleaned sample (tubes on graphene cannot be seen at this magnification) and (c) a STEM MAADF image from the region marked as [c]. (d, e) Atomic-resolution close-up of a tube in region [d] in contact with graphene and (f) corresponding Fourier transform (FT). The chiral indices analyzed from the FT correspond to $(20, 2)$. (g) Close-up of region [g] showing a $(19, 1)$ tube and (h, i) a $(6, 6)$ armchair tube completely aligned by AB stacking with graphene, i.e., $|\theta_{armchair} - \theta_{chiral}| = 0°$. (j) Histogram of observed stacking angles for 24 distinct interfaces, with 30° representing turbostratic and 0° representing AB stacking.

properties.[21] Likewise, the relative orientation strongly influences their electronic coupling: in earlier experiments, the contact barriers between graphite and carbon nanotubes were modulated by an order of magnitude simply by changing the orientation.[22]

Through three-dimensional reconstructions of the interfaces, we find that graphene partially folds around the suspended molecules. The interplay between vdW and elastic energies allows them to maximize the contact area and thus minimize the total energy of the system. Much like a canvas strained by a mass that it supports, the graphene membrane also becomes slightly strained. This tension dampens the mechanical vibrations of clean suspended areas, allowing the vdWHs to be imaged at resolutions higher than separately possible for either material as cleanly as here. Unlike their vacuum-suspended counterparts, individual atoms of the tubes embedded in heterostructures can be resolved not just near the suspension point[23] but also over their entire length. Complementary to scanning probe

techniques,[24,25] this approach may prove useful for the direct identification of point defects at ambient temperature.

Finally, we find that the carbon nanotubes align on the surface according to the symmetry of graphene, presumably to optimize the stacking of their lower wall with the underlying lattice. Nanotubes have been previously observed to grow epitaxially on graphite step edges,[26] but here they self-order on ultraclean graphene due to thermal excitation.

RESULTS AND DISCUSSION

The heterostructures were fabricated as in Figure 1a, starting with the synthesis of carbon nanotubes by floating catalyst chemical vapor deposition (CVD)[27,28] followed by direct deposition[29] onto monolayer graphene and cleaning by laser irradiation in vacuum.[30] The cleaning procedure exposed large atomically pure areas of up to 1 μm^2 in size for atomic-resolution scanning transmission electron microscopy (STEM) analysis, as shown by the medium-angle annular dark field (MAADF) image

91
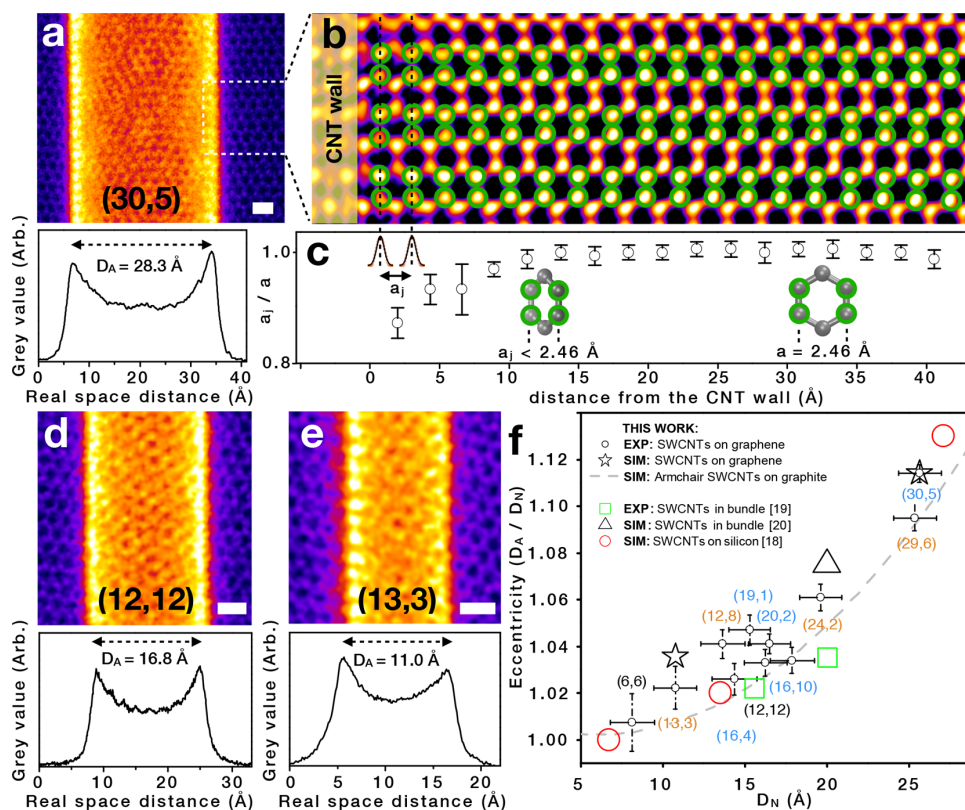
Figure 2. SWCNT deformation. (a) Large-diameter (30, 5) SWCNT on graphene, with a line profile revealing its apparent diameter. (b) Fourier-filtered graphene lattice next to the (30, 5) tube with (c) the corresponding interatomic distances a_j as a function of the distance from the SWCNT wall. (d, e) Close-ups of (12, 12) and (13, 3) tubes with their line profiles. (f) Measured eccentricity ($\epsilon = D_A/D_N$) of SWCNTs suspended on graphene. The coloring of the tabulated (n, m) values encodes semiconducting (orange), metallic (black), and semimetallic (blue) carbon nanotube species. Each image scale bar in (a) and (d−e) has a length of 0.4 nm. To enhance the image contrast in (a, b) and (d, e), ImageJ lookup table "Fire" was applied.

in Figure 1c magnifying a small part of what was imaged in bright-field mode in Figure 1b. Within the example field of view, we find several SWCNTs in direct contact with graphene over hundreds of nanometers, as evidenced by their common focus. (To appear sharp, atoms need to lie within the depth of field of our STEM system, approximately 2−3 nm, and at these distances, the molecules are brought together by vdW forces.) Unlike noncleaned samples (Supporting Information Section 1), these structures are devoid of contamination, hindering the view during STEM observations, and their atomic structure can be directly determined. The interfaces assume either well-aligned or meandering configurations, both visible in our examples. In the following analysis, however, we restrict ourselves to the aligned segments that exhibit the highest possible periodicity and thus structural unambiguity.

The structure of a SWCNT is completely described by its chiral indices (n, m). Together with the graphene basis vectors, these span chiral vector C_h.[31] Any tube can thus be constructed by wrapping a sheet of graphene around a cylinder at a chiral angle θ_{chiral} and connecting the perimeters. The chiral indices of a nanotube can be directly determined from its electron diffraction pattern,[32] an atomically resolved real-space image,[33] or its Fourier transform (FT). Here we exclusively use the latter approach, acquiring atomically resolved images such as those shown in Figure 1d,e,g,i. When SWCNTs are deposited on

graphene, the contrast of the lattices is intermixed and structural identification requires working in Fourier space. For example, the FT of the heterostructure of Figure 1d is presented in Figure 1f, showing distinct contributions from both materials. The layer lines $L_{1\cdots n}$ and the equatorial line L_0 arise from the lattice of the nanotube, and the graphene reflections arise from the atoms in the background. The intensity oscillations along $L_{1\cdots n}$ and their spacing $d_{1\cdots n}$ are mathematically related to the structure of the tube, with each line being described by a single Bessel function.[34] Given that SWCNTs may compress radially on the surface and thus have an ill-defined diameter,[18] the best structural unambiguity is achieved by separately analyzing the layer line spacing[35] and the oscillations along the lines[36] and comparing the experiments to STEM simulations.[37] For example, the best structural match for the tube in Figure 1d,e is (20, 2) having a chiral angle of 4.7° and nominal diameter D_N of 16.51 Å. The methods for structural determination are discussed in Supporting Information Section 2.

Following this procedure, we can acquire the structure of any suspended SWCNT imaged with a sufficiently high signal-to-noise ratio. For example, the tube in Figure 1g is (19, 1) and thus has a slightly smaller diameter of 15.28 Å, as also readily visible from the real-space image. A particularly interesting case of a (6, 6) armchair tube with an extremely small diameter of just 8.18 Å appearing to be perfectly aligned with the supporting graphene
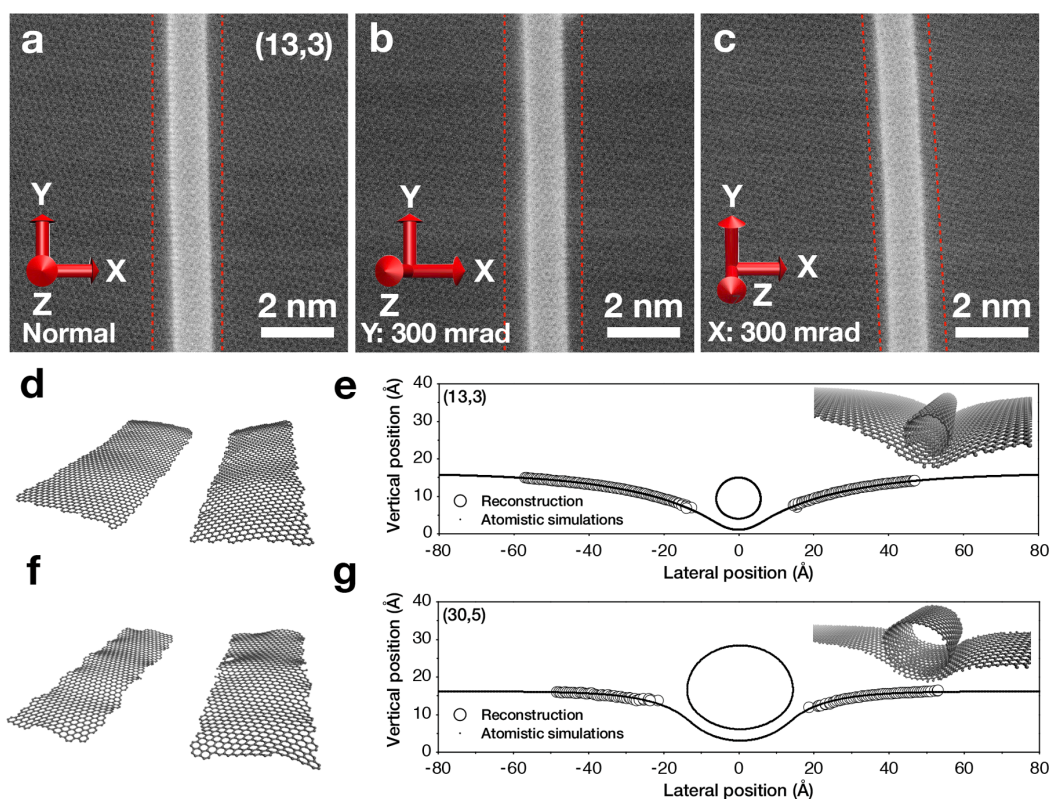
Figure 3. Graphene deformation. (a) Atomically resolved normal projection of the (13, 3) tube on graphene. Projections of the same site rotated by 300 mrad around either the *y* (b) or *x* axis (c). (d) Reconstructed graphene lattice around the (13, 3) tube and the cross-section of the fitted atomistic simulations in (e). The simulated model is shown in the upper right corner as an inset. (f) Reconstruction of the graphene lattice around the (30, 5) tube and (g) the fitted simulation. The experimental points in (e) and (g) are average atom positions perpendicular to the tube axis.

lattice is presented in Figure 1h,i. Since FT represents the frequency components of a real-space image in all directions, it also encodes the orientation of any periodic structure. Hence, we can find the relative orientation of graphene and SWCNT hexagons (although we cannot know which frequency components arise from the bottom and which arise from the top layer) by determining angles $\theta_{armchair}$ and θ_{chiral} in Fourier space (Figure 1f). For example, the (20, 2) tube has a helicity of 4.7° (i.e., the armchair edge is rotated by this amount with respect to the tube axis), and from the FT, we see that $\theta_{armchair}$ (angle between the tube axis and the nearest graphene armchair edge) is exactly 30°. This gives us a misalignment angle of 25.3° for the (20, 2) tube and 0° for the (6, 6) tube.

We systematically analyzed 24 heterostructures for which the related angles could be reliably determined. The distribution of these angles is shown in Figure 1j. Interestingly, we observe a nonuniform distribution favoring the aligned configuration, implying that the SWCNTs are not randomly oriented despite having landed on the substrate randomly.[29]

We suspect that this alignment is not spontaneous but is enabled by the laser treatment, simultaneously providing the required thermal energy while removing the contamination that would hinder the movement. Approximately 55% of the heterostructures remain disordered, which could result from residual contamination stuck in the nanotube junctions, such as those presented in Figure 1c. The nanotubes appear to reach a (constrained) energy minimum within the potential landscape

of graphene and hence preserve their orientation over relatively long distances. Interestingly, the aligned structures not only have the highest possible symmetry but also allow the nanotube handedness to be directly extracted based on the graphene orientation.[26]

We now turn our attention to the detailed response of the heterostructure to dispersion forces, first concentrating on the nanotubes. After seminal molecular mechanics predictions in the early 1990s,[20] the radial deformation of SWCNTs as influenced by substrates has also been studied experimentally.[18,19] Most investigations, however, have been limited to scanning probe methods,[18,38,39] posing problems with tip deconvolution, the vdW distance to the substrate, and surface roughness.[38] Moreover, a structural determination using these techniques is extremely demanding.[25] In contrast, our heterostructures provide the first clean view to measure such effects using an electron probe free of these confounding factors. Furthermore, the image scale can be directly calibrated in Fourier space by using the nearest-neighbor distance in graphene and finally the apparent diameter (D_A) measured at sub-angstrom accuracy.

The eccentricity (ϵ) of a deformed tubular object can be described as the ratio of the major and minor axes of the ellipse it forms. Here we use a slightly different definition, $\epsilon = D_A/D_N$, i.e., comparing the apparent and nominal diameters directly. For this comparison, we have chosen three tubes (13, 3), (12, 12), and (30, 5) with nominal diameters of 10.79, 16.29, and 25.67 Å,
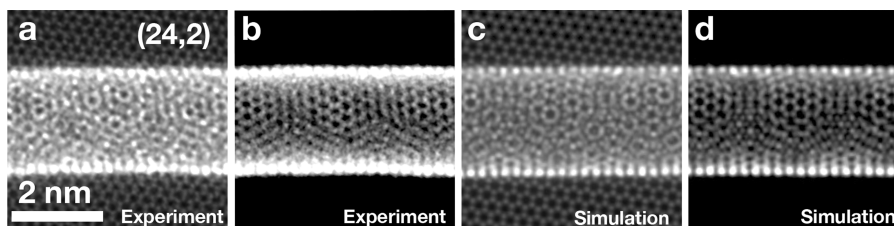
93

Figure 4. Imaging stability. (a) A STEM MAADF image of a (24, 2) SWCNT supported on graphene and (b) the same image after Fourier filtering the graphene. (c) Image simulation of the same structure with graphene removed in (d). Note that the signal-to-noise ratio in (a, b) was improved by double Gaussian filtering.[42]

respectively, as shown in Figure 2a,d,e. To determine their eccentricity, we analyzed the wall separation by fitting Gaussian line shapes to the nanotube cross-sectional intensity profiles shown below the real-space images. For example, the small-diameter (13, 3) tube is quite rigid, undergoing only a small deformation to $\epsilon = 1.022$. The slightly larger (12, 12) tube flattens more to an eccentricity of 1.033, and the (30, 5) tube flattens to as high as 1.114. In total, we studied the deformation of 10 structurally identified tubes, with the results gathered in Figure 2f. Neither the chiral angle nor the electronic type (semiconductor or metal) appear to be correlated with the amount of deformation, which confirms earlier theoretical predictions.[40] Generally speaking, however, and especially considering the accuracy of our method, the data shows a large variation in ϵ. Surprisingly, deformation on graphene seems to be greater than what is separately reported for bundled SWCNTs[19] or on bulk substrates.[18]

To understand these discrepancies, we used atomistic simulations (Methods) to study the adsorption of SWCNTs on both graphene and graphite. Graphite was imitated by completely fixing a single layer of graphene, whereas to reproduce the curvature of graphene found in experiments (discussed next), the simulation cell perpendicular to tube axis was initially compressed by 0.7−0.8%, leaving the graphene under a negative strain and thus free to adapt to the adsorbed tube. Simulations were performed on (i) (13, 3) and (30, 5) tubes suspended on graphene and marked with star symbols in Figure 2f and (ii) for a number of armchair tubes suspended on graphite, as indicated by the dashed line.

Interestingly, tubes on graphene show larger deformations than on graphite, $\epsilon = 1.038$ vs 1.009 for (13, 3) and 1.110 vs 1.090 for (30, 5). This initially counterintuitive result is explained by an increase in binding energy on graphene, in respective order yielding 0.085 vs 0.176 eV/Å and 0.205 vs 0.411 eV/Å. This is a direct consequence of graphene minimizing the surface energy by partially folding around the nanotube as in Figure 3e−g and Supporting Information Figure S5. Thus, the gain in surface energy is achieved by the greater structural deformation of the tube.

The observed variation in ϵ can be similarly explained: randomly oriented tubes on isotropically strained graphene undergo minimum deformation, but a uniaxial strain allows graphene to bend perpendicular to this axis, with some of the tubes deviating from the curve.

Apparently, the real-world membrane behaves like this, with the strain continuously varying in both direction and magnitude at different locations on the sample.

We turn our attention next to graphene, which ideally is a perfectly two-dimensional crystal. We start by analyzing the interatomic spacing of the graphene lattice around the carbon

nanotubes. In normal projection, a planar topology has isotropic atomic separations quantized to 60° angles. This, however, systematically changes on a curved surface, as schematically depicted in the lower part of Figure 2c. Here, we chose the lattice near the (30, 5) tube and used Fourier filtering to produce a clearer view of the atom positions, shown in Figure 2b. From the filtered image, we extracted the interatom separations by fitting Gaussian line shapes to the intensity profiles of each atom, highlighted by the green circles, producing the data shown in Figure 2c. If we schematically approach the interface from the right-hand side, then we observe a decrease in the apparent atom separation, extending ~20 Å from the edge and thus implying local out-of-plane curvature. By this method alone, however, the vertical direction of the inclination is ambiguous.

This limitation can be overcome by analyzing atomic-resolution images of the sample recorded from the same area under different tilt angles. We have recently developed an algorithm that obtains the 3D structure of a 2D material (graphene) from a minimum of two projections with a relative sample tilt of about 15−20°.[41] The algorithm identifies the position of each atom within the experimental projections and then finds the best-matching 3D structure that minimizes the difference between simulated images of the structure and the available experimental ones. Figure 3b,c shows projections of the (13, 3) tube on graphene acquired by rotating the sample separately around the x and y axes by 300 mrad (17.2°) relative to the normal incidence in Figure 3a. Since only the structure of the single-layer graphene can be unambiguously reconstructed, the atom positions between the red dashed lines were omitted from the analysis, finally yielding the 3D atomic model shown in Figure 3d. To recover the complete structure including the nanotube, we performed several atomistic simulations with a varying degree of strain in the graphene to simultaneously match the result to experimental graphene curvature and SWCNT eccentricity (Methods). As readily visible in Figure 3e, the simulation reveals an ~14-Å-deep 1D groove symmetrically expanding on both sides of the tube. The experimental points here represent the average vertical positions of atoms perpendicular to the tube axis. Following the same procedure, we also studied the graphene curvature around the (30, 5) tube, for which the reconstructed lattice and simulation are shown in Figure 3f,g, respectively.

Finally, given the high adsorption energies and the strain in graphene, these hybrid structures are extremely stable in our STEM experiments. Images can be acquired from arbitrary positions at resolution exceptional for such large and atomically clean systems. Furthermore, graphene can be effectively eliminated from the data by Fourier filtering.[16] This reveals a beautiful view of the SWCNT lattice from which the positions of individual atoms can be resolved along the tube axis. Such an

example is shown in Figure 4a,b, displaying a (24, 2) tube with and without the graphene background. These images are extremely sharp, exhibiting a striking resemblance to the image simulations in Figure 4c,d.

CONCLUSIONS

By using graphene and single-walled carbon nanotubes as a model heterostructure, we have studied atomic-scale deformations in a 1D−2D molecular interface held together by van der Waals forces. The interface shows topographically interesting features, with nanotubes dipping into the supporting graphene layer, creating ordered, long-range, one-dimensional grooves that reduce the surface energy of the structure. With the help of multiple projections, the three-dimensional structure of the lattice can be reconstructed, and when correlated with atomistic simulations, the morphology of the complete heterostructure is recovered. The graphene support thus allows the nanotubes to be observed along their entire length at room temperature with accuracy previously possible only through scanning probe techniques on rigid substrates.

METHODS

Sample Fabrication. Carbon nanotubes were synthesized using floating catalyst chemical vapor deposition. For small-diameter tubes, we used carbon monoxide as the carbon precursor, decomposing on *ex-situ*-generated iron nanoparticles at 880 °C.[27] The larger-diameter tubes were synthesized at 1050 °C by ethylene precursor decomposing on nanoparticles formed *in situ* from ferrocene vapor.[28] The as-synthesized tubes were dry-deposited[29] on commercial CVD graphene (Graphenea Inc.) suspended on perforated silicon nitride grids (Ted Pella Inc.) The structures were cleaned by 20 s of laser irradiation at 3 W excitation power[30] under 10^{-7} Pa pressure and transferred to the microscope column within the same vacuum system.

Scanning Transmission Electron Microscopy. Atomic-resolution imaging used the aberration-corrected Nion UltraSTEM 100 operated with a 60 keV primary beam energy, with the sample in a near-ultrahigh vacuum of 2×10^{-7} Pa. The angular range for the medium-angle annular dark-field (MAADF) detector was 60−200 mrad. Sample tilt was eliminated by bringing a 64×64 nm field of view completely into focus by rotating the sample in a standard Nion double-tilt holder. With our 2 to 3 nm depth of field, this corresponds to a maximum tilt of less than 5°, providing good unambiguity in the (n, m) assignment.[37] To minimize spatial inaccuracies caused by scan distortions (i.e., variations in the vertical scan speed) or drift, the nanotube diameters were measured from images acquired by setting the scan direction perpendicular to the carbon nanotube axis. For reliable (n, m) assignment, both parallel and perpendicular scans were used and compared.

Scanning Transmission Electron Microscopy Simulations. STEM simulations were performed using QSTEM 2.31 with a chromatic aberration coefficient of 1 mm, a spherical aberration coefficient of 1 μm, an energy spread of 0.48 eV, and MAADF detector angles set to the experimental range of 60−200 mrad. The illumination semiangle was 35 mrad. In Figure 4c,d, the best match with the experiment was achieved by placing the carbon nanotube at a van der Waals distance (0.34 nm) from the graphene membrane (without energy optimization) and rotating the whole system by 5° around the principal axis perpendicular to the tube, with the electron beam then encountering the sample plane at this angle. The chiral index, (24, 2), and the relative graphene orientation in the simulation were identified from the experimental image as described in the text and in Supporting Information Section 2. To mimic the experimental contrast in Figure 4d, graphene was first included in the simulations and manually removed by Fourier filtering.

Three-Dimensional Reconstruction. The three-dimensional reconstruction was done by matching a simulated model to a series of experimental images acquired from different tilt angles by rotating

the sample to ±300 mrad inclination during imaging. Finally, the structure was obtained through an optimization process where both the atomic positions and the simulated imaging parameters were iteratively changed until the best possible match to the experiment was found.[41] This was possible since the location of each graphene lattice atom and their connections to nearest neighbors could be discerned from each projection.

Atomistic Simulations. The adaptive intermolecular reactive empirical bond order (AIREBO)[43] potential was used to describe the covalent bonding in graphene and nanotubes, whereas vdW interactions were included by augmenting the model with a Morse potential.[44] The torsion component of the AIREBO potential for the nanotube was turned off since this gave a better match with the experimental results, and the Morse potential parameters were identical to the AIREBO Morse potential.[44] All structural minimization processes were performed using the large-scale atomic/molecular massively parallel simulator (LAMMPS) code.[45,46]

For each carbon nanotube, the graphene structure was oriented so that it is commensurate with a single unit cell of the chiral nanotubes, which is necessary to enforce the periodic boundary conditions along the axis. For the (13, 3) and (30, 5) tubes, the rotated graphene unit cell was multiplied perpendicular to the axis by 12- and 28-fold, respectively. Hence, the total width of graphene for the (13, 3) tube was ∼64 nm, and that for the (30, 5) tube was ∼66 nm. To match the graphene curvature with the reconstructed results, the bounding box of the cell was shrunk by 0.7 and 0.8% for the (13, 3) and (30, 5) tubes, respectively. The nanotube eccentricity was determined by comparing the diameters of a relaxed nanotube in vacuum and on the surface.

ASSOCIATED CONTENT

ⓈSupporting Information

The Supporting Information is available free of charge on the ACS Publications website at DOI: 10.1021/acsnano.8b04050.

> Images of non-laser-treated heterostructures, description of the chiral index assignment, and the relation of adsorption energy and carbon nanotube eccentricity (PDF)

AUTHOR INFORMATION

Corresponding Authors
*E-mail: kimmo.mustonen@univie.ac.at.
*E-mail: jannik.meyer@univie.ac.at.

ORCID ⓞ
Kimmo Mustonen: 0000-0002-0953-7299
Christoph Hofer: 0000-0002-0844-8366
Kenan Elibol: 0000-0002-8765-2794
Patrik Laiho: 0000-0001-8234-1607
Toma Susi: 0000-0003-2513-573X
Jannik C. Meyer: 0000-0003-4023-0778

Notes
The authors declare no competing financial interest.

ACKNOWLEDGMENTS

95

REFERENCES

(1) Geim, A. K.; Grigorieva, I. V. Van der Waals Heterostructures. *Nature* **2013**, *499*, 419−425.

(2) Jariwala, D.; Marks, T. J.; Hersam, M. C. Mixed-dimensional van der Waals Heterostructures. *Nat. Mater.* **2017**, *16*, 170.

(3) Liu, Y.; Weiss, N. O.; Duan, X.; Cheng, H.-C.; Huang, Y.; Duan, X. Van der Waals Heterostructures and Devices. *Nat. Rev. Mater.* **2016**, *1*, 16042.

(4) Britnell, L.; Ribeiro, R.; Eckmann, A.; Jalil, R.; Belle, B.; Mishchenko, A.; Kim, Y.-J.; Gorbachev, R.; Georgiou, T.; Morozov, S.; Grigorenko, A. N.; Geim, A. K.; Casiraghi, C.; Castro Neto, A. H.; Novoselov, K. S. Strong Light-Matter Interactions in Heterostructures of Atomically Thin Films. *Science* **2013**, *340*, 1311−1314.

(5) Zheng, Q.; Saidi, W. A.; Xie, Y.; Lan, Z.; Prezhdo, O. V.; Petek, H.; Zhao, J. Phonon-Assisted Ultrafast Charge Transfer at van der Waals Heterostructure Interface. *Nano Lett.* **2017**, *17*, 6435−6442.

(6) Gjerding, M. N.; Petersen, R.; Pedersen, T.; Mortensen, N. A.; Thygesen, K. S. Layered van der Waals Crystals with Hyperbolic Light Dispersion. *Nat. Commun.* **2017**, *8*, 320.

(7) Yu, W. J.; Vu, Q. A.; Oh, H.; Nam, H. G.; Zhou, H.; Cha, S.; Kim, J.-Y.; Carvalho, A.; Jeong, M.; Choi, H.; Castro Neto, A. H.; Lee, Y. H.; Duan, X. Unusually Efficient Photocurrent Extraction in Monolayer van der Waals Heterostructure by Tunnelling Through Discretized Barriers. *Nat. Commun.* **2016**, *7*, 13278.

(8) Argentero, G.; Mittelberger, A.; Reza Ahmadpour Monazam, M.; Cao, Y.; Pennycook, T. J.; Mangler, C.; Kramberger, C.; Kotakoski, J.; Geim, A.; Meyer, J. C. Unraveling the 3D Atomic Structure of a Suspended Graphene/hBN van der Waals Heterostructure. *Nano Lett.* **2017**, *17*, 1409−1416.

(9) Leven, I.; Maaravi, T.; Azuri, I.; Kronik, L.; Hod, O. Interlayer Potential for Graphene/h-BN Heterostructures. *J. Chem. Theory Comput.* **2016**, *12*, 2896−2905.

(10) Yang, W.; Chen, G.; Shi, Z.; Liu, C.-C.; Zhang, L.; Xie, G.; Cheng, M.; Wang, D.; Yang, R.; Shi, D.; Watanabe, K.; Taniguchi, T.; Yao, Y.; Zhang, Y.; Zhang, G. Epitaxial Growth of Single-Domain Graphene on Hexagonal Boron Nitride. *Nat. Mater.* **2013**, *12*, 792.

(11) Zhang, C.; Zhao, S.; Jin, C.; Koh, A. L.; Zhou, Y.; Xu, W.; Li, Q.; Xiong, Q.; Peng, H.; Liu, Z. Direct Growth of Large-Area Graphene and Boron Nitride Heterostructures by a Co-Segregation Method. *Nat. Commun.* **2015**, *6*, 6519.

(12) Yan, A.; Velasco, J., Jr; Kahn, S.; Watanabe, K.; Taniguchi, T.; Wang, F.; Crommie, M. F.; Zettl, A. Direct Growth of Single-and Few-Layer MoS2 on h-BN with Preferred Relative Rotation Angles. *Nano Lett.* **2015**, *15*, 6324−6331.

(13) Xu, S.; Han, Y.; Chen, X.; Wu, Z.; Wang, L.; Han, T.; Ye, W.; Lu, H.; Long, G.; Wu, Y.; Lin, J.; Cai, K. M.; Yuan, Ho; He, Y.; Wang, N. van der Waals Epitaxial Growth of Atomically Thin Bi₂Se₃ and Thickness-Dependent Topological Phase Transition. *Nano Lett.* **2015**, *15*, 2645−2651.

(14) Zuo, Z.; Xu, Z.; Zheng, R.; Khanaki, A.; Zheng, J.-G.; Liu, J. In-situ Epitaxial Growth of Graphene/h-BN van der Waals Heterostructures by Molecular Beam Epitaxy. *Sci. Rep.* **2015**, *5*, 14760.

(15) Rooney, A. P.; Kozikov, A.; Rudenko, A. N.; Prestat, E.; Hamer, M. J.; Withers, F.; Cao, Y.; Novoselov, K. S.; Katsnelson, M. I.; Gorbachev, R.; Haigh, S. J. Observing Imperfection in Atomic Interfaces for van der Waals Heterostructures. *Nano Lett.* **2017**, *17*, 5222−5228.

(16) Mirzayev, R.; Mustonen, K.; Monazam, M. R.; Mittelberger, A.; Pennycook, T. J.; Mangler, C.; Susi, T.; Kotakoski, J.; Meyer, J. C. Buckyball Sandwiches. *Sci. Adv.* **2017**, *3*, e1700176.

(17) Smith, B. W.; Monthioux, M.; Luzzi, D. E. Encapsulated C₆₀ in Carbon Nanotubes. *Nature* **1998**, *396*, 323−324.

(18) Hertel, T.; Walkup, R. E.; Avouris, P. Deformation of Carbon Nanotubes by Surface van der Waals Forces. *Phys. Rev. B: Condens. Matter Mater. Phys.* **1998**, *58*, 13870.

(19) Jiang, Y.; Zhou, W.; Kim, T.; Huang, Y.; Zuo, J. Measurement of Radial Deformation of Single-wall Carbon Nanotubes Induced by Intertube van der Waals Forces. *Phys. Rev. B: Condens. Matter Mater. Phys.* **2008**, *77*, 153405.

(20) Ruoff, R. S.; Tersoff, J.; Lorents, D. C.; Subramoney, S.; Chan, B. Radial Deformation of Carbon Nanotubes by van der Waals Forces. *Nature* **1993**, *364*, 514−516.

(21) Kim, T.; Kim, G.; Choi, W. I.; Kwon, Y.-K.; Zuo, J.-M. Electrical Transport in Small Bundles of Single-Walled Carbon Nanotubes: Intertube Interaction and Effects of Tube Deformation. *Appl. Phys. Lett.* **2010**, *96*, 173107.

(22) Paulson, S.; Helser, A.; Nardelli, M. B.; Taylor, R.; Falvo, M.; Superfine, R.; Washburn, S. Tunable Resistance of a Carbon Nanotube-Graphite Interface. *Science* **2000**, *290*, 1742−1744.

(23) Warner, J. H.; Young, N. P.; Kirkland, A. I.; Briggs, G. A. D. Resolving Strain in Carbon nanotubes at the Atomic Level. *Nat. Mater.* **2011**, *10*, 958.

(24) Ishigami, M.; Choi, H. J.; Aloni, S.; Louie, S. G.; Cohen, M. L.; Zettl, A. Identifying Defects in Nanoscale Materials. *Phys. Rev. Lett.* **2004**, *93*, 196803.

(25) Odom, T. W.; Huang, J.-L.; Kim, P.; Lieber, C. M. Atomic Structure and Electronic Properties of Single-Walled Carbon Nanotubes. *Nature* **1998**, *391*, 62−64.

(26) Chen, Y.; Shen, Z.; Xu, Z.; Hu, Y.; Xu, H.; Wang, S.; Guo, X.; Zhang, Y.; Peng, L.; Ding, F.; Liu, Z.; Zhang, J. Helicity-Dependent Single-Walled Carbon Nanotube Alignment on Graphite for Helical Angle and Handedness Recognition. *Nat. Commun.* **2013**, *4*, 2205.

(27) Mustonen, K.; Laiho, P.; Kaskela, A.; Zhu, Z.; Reynaud, O.; Houbenov, N.; Tian, Y.; Susi, T.; Jiang, H.; Nasibulin, A. G.; Kauppinen, E. I. Gas Phase Synthesis of Non-Bundled, Small Diameter Single-Walled Carbon Nanotubes With Near-Armchair Chiralities. *Appl. Phys. Lett.* **2015**, *107*, 013106.

(28) Hussain, A.; Liao, Y.; Zhang, Q.; Ding, E.-X.; Laiho, P.; Ahmad, S.; Wei, N.; Tian, Y.; Jiang, H.; Kauppinen, E. I. Floating Catalyst CVD Synthesis of Single Walled Carbon Nanotubes from Ethylene for High Performance Transparent Electrodes. *Nanoscale* **2018**, *10*, 9752−9759.

(29) Laiho, P.; Mustonen, K.; Ohno, Y.; Maruyama, S.; Kauppinen, E. I. Dry and Direct Deposition of Aerosol Synthesized Single-Walled Carbon Nanotubes by Thermophoresis. *ACS Appl. Mater. Interfaces* **2017**, *9*, 20738−20747.

(30) Tripathi, M.; Mittelberger, A.; Mustonen, K.; Mangler, C.; Kotakoski, J.; Meyer, J. C.; Susi, T. Cleaning Graphene: Comparing Heat Treatments in Air and in Vacuum. *Phys. Phys. Status Solidi RRL* **2017**, *11*, 1700124.

(31) Dresselhaus, M. S.; Dresselhaus, G.; Eklund, P.; Rao, A. *The Physics of Fullerene-Based and Fullerene-Related Materials*; Springer, 2000; pp 331−379.

(32) Iijima, S.; Ichihashi, T. Single-Shell Carbon Nanotubes of 1-nm Diameter. *Nature* **1993**, *363*, 603.

(33) Hashimoto, A.; Suenaga, K.; Urita, K.; Shimada, T.; Sugai, T.; Bandow, S.; Shinohara, H.; Iijima, S. Atomic Correlation Between Adjacent Graphene Layers in Double-Wall Carbon Nanotubes. *Phys. Rev. Lett.* **2005**, *94*, 045504.

(34) Amelinckx, S.; Lucas, A.; Lambin, P. Electron Diffraction and Microscopy of Nanotubes. *Rep. Prog. Phys.* **1999**, *62*, 1471.

(35) Jiang, H.; Nasibulin, A. G.; Brown, D. P.; Kauppinen, E. I. Unambiguous Atomic Structural Determination of Single-Walled Carbon Nanotubes by Electron Diffraction. *Carbon* **2007**, *45*, 662−667.

(36) Liu, Z.; Qin, L.-C. A Direct Method to Determine the Chiral Indices of Carbon Nanotubes. *Chem. Phys. Lett.* **2005**, *408*, 75−79.

(37) Liu, Z.; Qin, L.-C. Electron Diffraction from Elliptical Nanotubes. *Chem. Phys. Lett.* **2005**, *406*, 106−110.

(38) Giusca, C. E.; Tison, Y.; Silva, S. R. P. Atomic and Electronic Structure in Collapsed Carbon Nanotubes Evidenced by Scanning

Tunneling Microscopy. *Phys. Rev. B: Condens. Matter Mater. Phys.* **2007**, *76*, 035429.

(39) Barraza-Lopez, S.; Albrecht, P. M.; Lyding, J. W. Carbon Nanotubes on Partially De-Passivated n-Doped Si (100)-(2 × 1): H Substrates. *Phys. Rev. B: Condens. Matter Mater. Phys.* **2009**, *80*, 045415.

(40) Li, C.; Chou, T.-W. Elastic Properties of Single-Walled Carbon Nanotubes in Transverse Directions. *Phys. Rev. B: Condens. Matter Mater. Phys.* **2004**, *69*, 073401.

(41) Hofer, C.; Kramberger, C.; Ahmadpour Monazam, M. R.; Mangler, C.; Mittelberger, A.; Argentero, G.; Kotakoski, J.; Meyer, J. C. Revealing the 3D Structure of Graphene Defects. *Conference on Physics of Defects in Solids: Quantum Mechanics Meets Topology*; July 12, 2018, Trieste, Italy.

(42) Krivanek, O. L.; Chisholm, M. F.; Nicolosi, V.; Pennycook, T. J.; Corbin, G. J.; Dellby, N.; Murfitt, M. F.; Own, C. S.; Szilagyi, Z. S.; Oxley, M. P.; Pantelides, S. T.; Pennycook, S. J. Atom-By-Atom Structural and Chemical Analysis by Annular Dark-Field Electron Microscopy. *Nature* **2010**, *464*, 571.

(43) Brenner, D. W. Empirical Potential for Hydrocarbons for Use in Simulating the Chemical Vapor Deposition of Diamond Films. *Phys. Rev. B: Condens. Matter Mater. Phys.* **1990**, *42*, 9458.

(44) O'Connor, T. C.; Andzelm, J.; Robbins, M. O. AIREBO-M: A Reactive Model for Hydrocarbons at Extreme Pressures. *J. Chem. Phys.* **2015**, *142*, 024903.

(45) Plimpton, S. Fast Parallel Algorithms for Short-Range Molecular Dynamics. *J. Comput. Phys.* **1995**, *117*, 1−19.

(46) Plimpton, S. J.; Thompson, A. P. Computational Aspects of Many-Body Potentials. *MRS Bull.* **2012**, *37*, 513−521.

97

SUPPLEMENTARY MATERIAL FOR:

Atomic-Scale Deformations at the Interface of a Mixed-Dimensional van der Waals Heterostructure

Kimmo Mustonen,[*,†] Aqeel Hussain,[‡] Christoph Hofer,[†] Mohammad R.A. Monazam,[†] Rasim Mirzayev,[†] Kenan Elibol,[†] Patrik Laiho,[‡] Clemens Mangler,[†] Hua Jiang,[‡] Toma Susi,[†] Esko I. Kauppinen,[‡] Jani Kotakoski,[†] and Jannik C. Meyer[*,†]

[†]*University of Vienna, Faculty of Physics, 1090 Vienna, Austria*

[‡]*Aalto University School of Science, Department of Applied Physics, P.O. Box 15100, FI-00076 Aalto, Finland*

E-mail: kimmo.mustonen@univie.ac.at; jannik.meyer@univie.ac.at

1. Non-cleaned heterostructures

Surface contamination originating from the CVD process, transfer and environment are a major concern for two-dimensional materials.[1,2] Despite our intrinsically clean synthesis process[3,4] and deposition[5] of single-walled carbon nanotubes (SWCNTs), the heterostructures fabricated on commercial CVD graphene were covered by contaminating material. Figure S1 shows how the samples typically appear prior to the high-power laser annealing.[6] In this particular case, the clean graphene spots, visible as dark contrast, are roughly 5–20 nm in size. While this is often enough for observation of 2D materials in their pristine state, it hinders the structural determination of SWCNTs and conceals the topographic features around them.
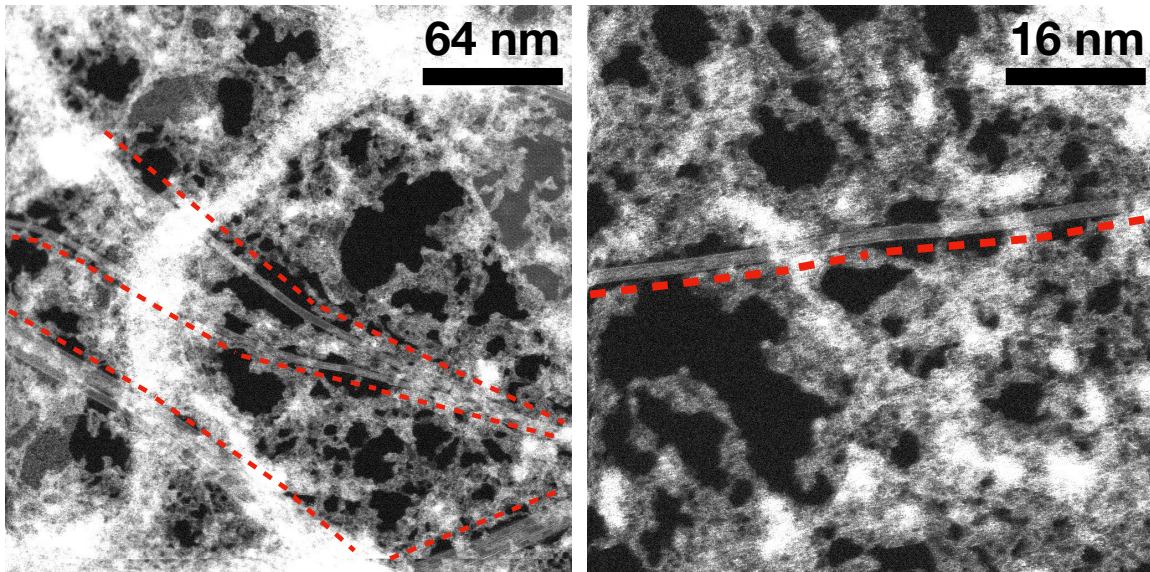
Figure 1: As-fabricated example of dry-deposited[5] single-walled carbon nanotubes[3,4] on commercial monolayer graphene from Graphenea Inc. The dark contrast in these images is clean graphene. To guide the readers' eye, the positions of carbon nanotubes are highlighted with red dashed lines.

2. Chiral index assignment for graphene-suspended carbon nanotubes

The assignment of chiral indices, (n, m), of a SWCNT by using *e.g.* transmission electron microscopy (TEM) in diffraction mode has many implementations.[7–13] A crude approximation is given by measurement of the diameter in real-space, and the chiral angle θ_{chiral} in reciprocal space through the use of electron diffraction.[13] All modern implementations, however, rely completely on the structural representation of a SWCNT in the reciprocal space, retrieving the structure based on the relative positions of the characteristic diffraction peaks.[10,12,14]

Here, instead of using electron diffraction, we calculate Fourier transforms (FTs) of real-space images thus converting them into reciprocal space. We first analyze the (n, m) of the SWCNT in manuscript Figure 1d and then test the robustness of our method to radial deformations. A real-space image of the tube is reproduced in Figure S2a and its FT in Figure S2b. The chiral indices are related to the structure of a tube in 3D reciprocal space, described by a set of Bessel functions.[9] These functions, when intersected by the Ewald's sphere, are represented by a number of layer lines that encode the structure of the tube. It has been independently shown that the layer line spacings are directly related to the chiral indices (n, m),[10] and so are the (squared) Bessel functions dominating the intensities along each layer line.[11,12] Figures S2c and S2d plot the intensity profiles along the layer lines L_1 and L_2. By measuring the relative distance of the first and second maxima we can determine the order of the Bessel function along the line by calculating $J_n(x) = X_2 / X_1$, yielding the chiral indices as tabulated in the original publication by Liu *et al.*[11] We can similarly use the layer line spacing, d_i, to calculate (n, m), for which the related intensity profiles are plotted in Figures S2e and S2f. The d_i is defined as a distance of each layer line from the equatorial line L_0, related to n and m through a set of geometric equations.[10] This method, however, is calibrated by the period of oscillation along the equatorial line, δ, proportional to the wall

3

separation of the tube only, rendering it susceptible to radial aberrations.
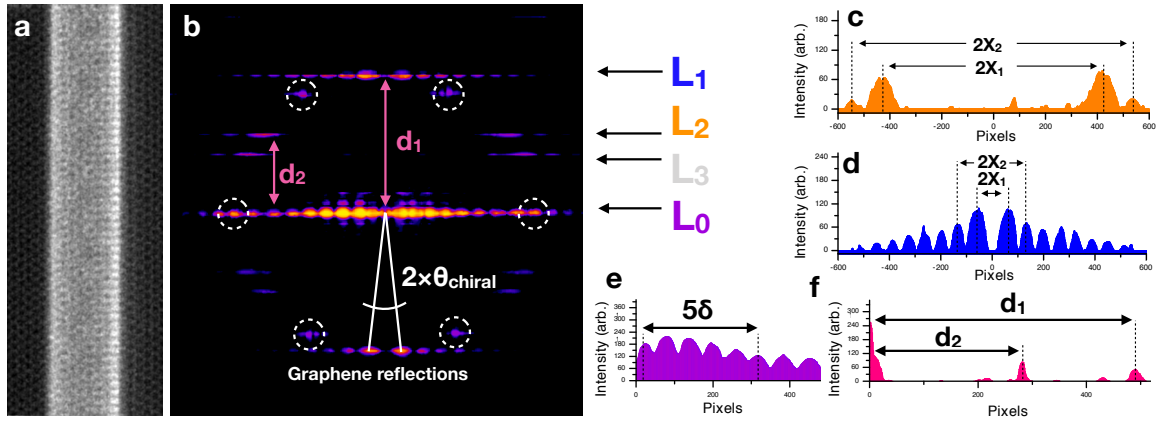
Figure 2: (a) Real-space image of the tube shown in manuscript Figure 1d and its Fourier transform in (b). The L_i and d_i mark the positions of layer lines and their distance from L_0. The intensity profiles along the layer lines L_1 and L_2 are shown in (c-d) and along the the equatorial line L_0 in (e). The intensity profile perpendicular to equatorial line is plotted in (f).

4

A calculation of X_2 / X_1 along L_2 yields 1.244 ± 0.005 and along L_1 2.202 ± 0.005 (uncertainties from peak positions). These values match best to $n = 20$ and $m = 2$, with a second best match of $n = 21$ and $m = 2$. Similarly, if we determine the structure using the d_i, we get $n = 20.39 \pm 0.1$ and $m = 1.95 \pm 0.1$.

To evaluate the robustness of the methods against radial deformations,[14] we determined the (n, m) for tubes simulated with an elliptical shape. Figures S3a-c show FTs of simulated $(20, 2)$ tubes radially compressed respectively by 0%, 3% and 6%. Starting with the circular case, we get X_2 / $X_1 = 1.246 \pm 0.001$ along L_2 and 2.177 ± 0.001 along L_1, matching almost perfectly to $n = 20$ and $m = 2$. Similarly, the layer line spacing yields $n = 20.00 \pm 0.01$ and $m = 2.01 \pm 0.01$.

For 3% and 6% compressed tubes we likewise acquire X_2 / $X_1 = 1.243 \pm 0.001$ and 1.243 ± 0.001 along L_2, and X_2 / $X_1 = 2.209 \pm 0.001$ and 2.182 ± 0.001 along L_1, respectively. The best structural match in both cases is $(20, 2)$ and the second best $(21, 2)$. From layer line spacing we get $n = 20.32 \pm 0.01$ and $m = 1.97 \pm 0.01$ for 3% compressed and $n = 20.52 \pm 0.01$ and $m = 1.94 \pm 0.01$ for 6% compressed tube. It thus appears the layer line spacing is, as expected, somewhat sensitive to radial deformations. Nonetheless, at high confidence our example tube is indeed a $(20, 2)$ with only a small amount of eccentricity. For unclear cases of (n, m), however, it may become necessary to run extensive simulations to assign the correct structure. As an example of that, Figure S4 compares the experimental FT to the nearest matching indices showing that $(20, 2)$ is closer than $(21, 2)$. For comparison, we also show a FT of $(20, 3)$, having a similar diameter but distinct structure in the reciprocal space.
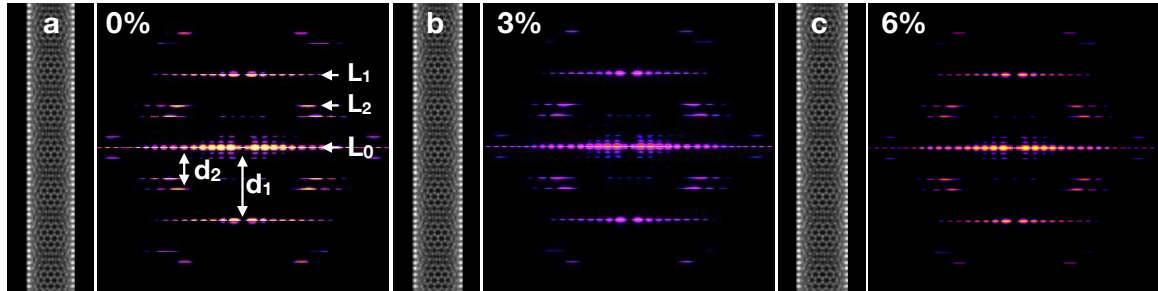
Figure 3: (a) A real-space image of a circular $(20, 2)$ tube and its Fourier transform. (b-c) 3% and 6% radially compressed $(20, 2)$ tubes with their corresponding Fourier transforms.
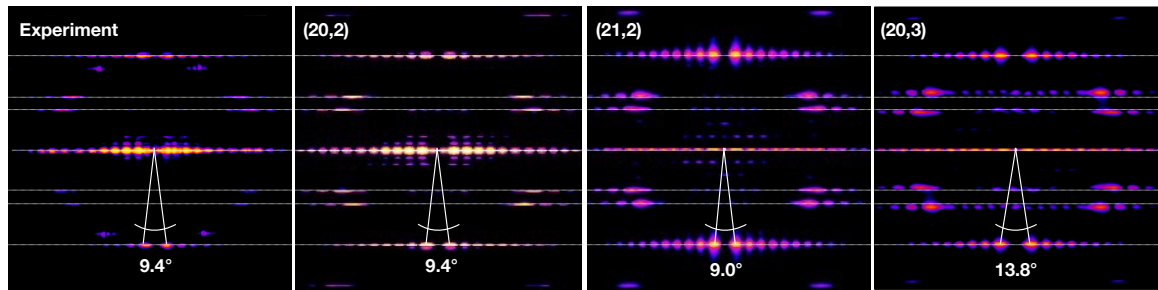
Figure 4: Comparison of the FT acquired from experiment to the closest matching chiral indices of $(20, 2)$ and $(21, 2)$. $(20, 3)$ is shown for comparison.

3. Adsorption energy and carbon nanotube eccentricity

The adsorption energy of a $(13, 3)$ SWCNT on graphene was calculated by compressing a pristine graphene supercell by 0.0-0.8% to introduce negative strain. The width of the graphene area in the cell was the same as in the main manuscript, $\sim$64 nm.

Here, we have normalized the adsorption energy and cell size by those of the non-compressed simulation cell. These normalized values are plotted in Figure S5, showing that when graphene is able to fold around the tube due to the negative strain, the nanotube shows larger deformation as measured by its eccentricity.

6
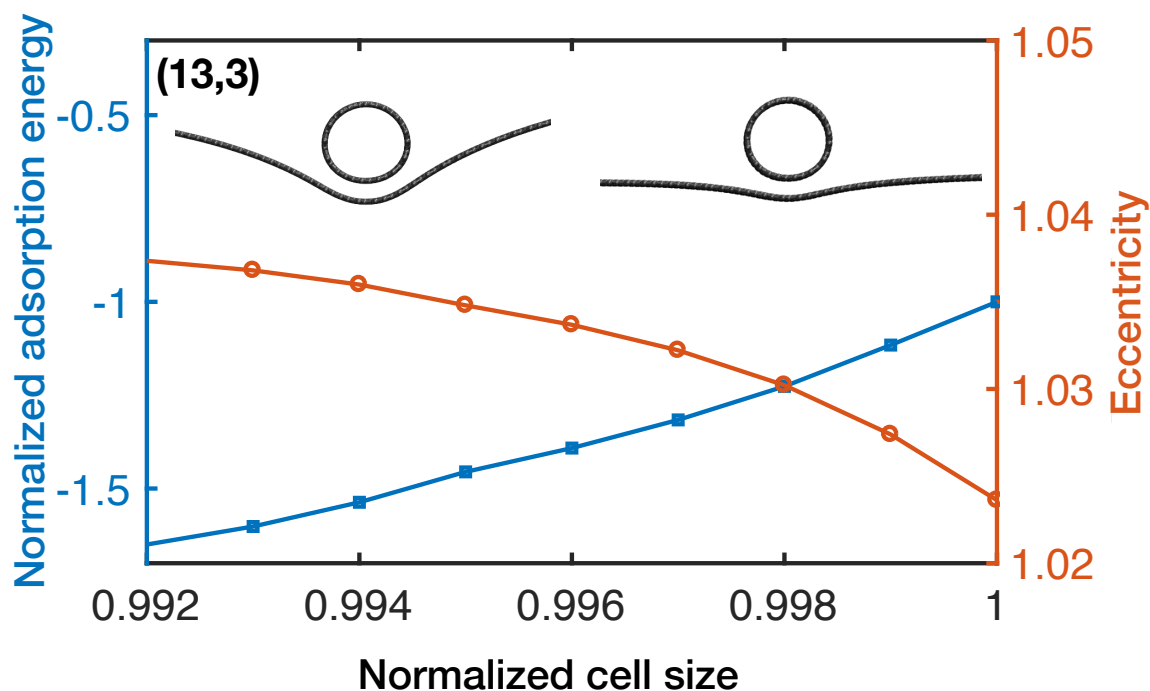
Figure 5: Normalized adsorption energy and eccentricity of a (13, 3) SWCNT on graphene as a function of normalized simulation cell size. Atomistic models of the extremes are shown as insets.

References

1. Haigh, S.; Gholinia, A.; Jalil, R.; Romani, S.; Britnell, L.; Elias, D.; Novoselov, K.; Ponomarenko, L.; Geim, A.; Gorbachev, R. Cross-Sectional Imaging of Individual Layers and Buried Interfaces of Graphene-Based Heterostructures and Superlattices. *Nat. Mater.* **2012**, *11*, 764.

2. Rooney, A. P.; Kozikov, A.; Rudenko, A. N.; Prestat, E.; Hamer, M. J.; Withers, F.; Cao, Y.; Novoselov, K. S.; Katsnelson, M. I.; Gorbachev, R.; Haigh, S. J. Observing Imperfection in Atomic Interfaces for van der Waals Heterostructures. *Nano Lett.* **2017**, *17*, 5222–5228.

3. Mustonen, K.; Laiho, P.; Kaskela, A.; Zhu, Z.; Reynaud, O.; Houbenov, N.; Tian, Y.; Susi, T.; Jiang, H.; Nasibulin, A. G.; Kauppinen, E. I. Gas Phase Synthesis of Non-

7

Bundled, Small Diameter Single-Walled Carbon Nanotubes With Near-Armchair Chiralities. *Appl. Phys. Lett.* **2015**, *107*, 013106.

4. Hussain, A.; Liao, Y.; Zhang, Q.; Ding, E.-X.; Laiho, P.; Ahmad, S.; Wei, N.; Tian, Y.; Jiang, H.; Kauppinen, E. I. Floating Catalyst CVD Synthesis of Single Walled Carbon Nanotubes from Ethylene for High Performance Transparent Electrodes. *Nanoscale* **2018**, *10*, 9752–9759.

5. Laiho, P.; Mustonen, K.; Ohno, Y.; Maruyama, S.; Kauppinen, E. I. Dry and Direct Deposition of Aerosol Synthesized Single-Walled Carbon Nanotubes by Thermophoresis. *ACS Appl. Mater. Interfaces* **2017**, *9*, 20738–20747.

6. Tripathi, M.; Mittelberger, A.; Mustonen, K.; Mangler, C.; Kotakoski, J.; Meyer, J. C.; Susi, T. Cleaning Graphene: Comparing Heat Treatments in Air and in Vacuum. *Phys. Status Solidi RRL* **2017**, *11*, 1700124.

7. Bernaerts, D.; Zettl, A.; Chopra, N. G.; Thess, A.; Smalley, R. Electron Diffraction Study of Single-Wall Carbon Nanotubes. *Solid State Commun.* **1998**, *105*, 145–149.

8. Colomer, J.-F.; Henrard, L.; Launois, P.; Van Tendeloo, G.; Lucas, A.; Lambin, P. Interpretation of Electron Diffraction from Carbon Nanotube Bundles Presenting Precise Helicity. *Phys. Rev. B* **2004**, *70*, 075408.

9. Meyer, J. C.; Paillet, M.; Duesberg, G. S.; Roth, S. Electron Diffraction Analysis of Individual Single-Walled Carbon Nanotubes. *Ultramicroscopy* **2006**, *106*, 176–190.

10. Jiang, H.; Nasibulin, A. G.; Brown, D. P.; Kauppinen, E. I. Unambiguous Atomic Structural Determination of Single-Walled Carbon Nanotubes by Electron Diffraction. *Carbon* **2007**, *45*, 662–667.

11. Liu, Z.; Qin, L.-C. A Direct Method to Determine the Chiral Indices of Carbon Nanotubes. *Chem. Phys. Lett.* **2005**, *408*, 75–79.

8

12. Jiang, H.; Brown, D. P.; Nasibulin, A. G.; Kauppinen, E. I. Robust Bessel-Function-Based Method for Determination of the (n, m) Indices of Single-Walled Carbon Nanotubes by Electron Diffraction. *Phys. Rev. B* **2006**, *74*, 035427.

13. Lambin, P.; Lucas, A. Quantitative Theory of Diffraction by Carbon Nanotubes. *Phys. Rev. B* **1997**, *56*, 3571.

14. Liu, Z.; Qin, L.-C. Electron Diffraction from Elliptical Nanotubes. *Chem. Phys. Lett.* **2005**, *406*, 106–110.

5

Summary

This cumulative thesis demonstrates 3D analysis using a tilted specimen when investigating 2D materials by STEM. Most importantly, the 3D structure can be extracted using only two images from different tilt angles of the atomically resolved object-of-interest. Paper 1 and chapter 3 discuss the novel method in detail and use this approach to reveal interesting out-of-plane deformations in graphene grain boundaries. Characteristics of the grain boundaries are shown to clearly depend on the misorientation angle of the two grains. The second paper uses the method to directly visualize the out-of-plane buckling of Si substitutions in graphene. Also investigated were more complex but still stable configurations like the silicon trimer (three silicon atoms incorporated in a defect in graphene) and the silicon tetramer (four silicon atoms incorporated in a defect in graphene) which builds a pyramid-like structure. The resulting structures agree excellently with the calculated relaxed models. In addition, in-situ dynamics have been observed that were only possible to measure when the sample is tilted. This is because a Si atom sticking out of the graphene plane results in a visible broken symmetry of the configuration when the sample is tilted. In particular, reversible flips of the Si substitution to the opposite side of the graphene plane have been observed. In contrast, only a single irreversible flip has been observed for the Si tetramer due to the impact of the electron beam. In a subsequent wrote by C. Su et al. (5th paper in the publication list), it is demonstrated that some events – in particular a Stone-Wales Transfer – can be only triggered from an electron hitting the neighboring carbon atom at a certain angle.

Paper 4 shows also deformations of graphene induced by Van-der-Waals forces of other structures, in this case of a carbon nanotube.

Paper 3 presented in this thesis shows an example for using the Z-contrast based medium-angle annular dark field STEM technique for characterizing atomic configurations. Here, we showed for the first time different configurations of oxygen in defect-rich graphene (graphene oxide) and compared their bonding preferences with the configuration of nitrogen dopants. This work is motivated by the relatively unknown structure characteristics of oxygen configurations in graphene oxide. Most of the data confirms the textbook concept of these elements: While nitrogen binds to carbon via two or three bonds, oxygen mostly binds to two carbon atoms. As an exception, graphitic oxygen binding to three carbon neighbors has also been observed, which is a configuration that is usually difficult to stabilize in extended compounds.

This work opens a new way towards a detailed study of the complete morphology of atomically-

thin materials, as demonstrated for graphene-based structures. As an outlook, this method should be capable of reconstructing other 2D materials such as hBN or any heteroatom impurity in these materials. In the case of transition metal dichalcogenides, where the unit cell is usually three atomic layer thick, the method should be directly applicable to reconstruct the isolated metal atom which is visible on one of the sublattices. In addition, the method could be generalized to use more than two projections for the complete reconstruction of few-layer materials. Also in this case, much fewer projections than what is required for a full tomographic series would be needed to elucidate the 3D structure. Here, a suited balance of assumptions to be put into the model (e.g. presence of certain elements) and the number of projections would have to be developed.

Contributions to scientific events

Participation in international conferences:

Date & Venue	Conference	Type	Title of contribution
02-06 May 2016 Lille (France)	Spring Meeting of the European Materials Research Society	Poster	Correlation between Raman Spectroscopy and Transmission Electron Microscopy
13.-16. February 2017 Levi (Finland)	Towards Reality in Nanoscale Materials IX	Oral	Isotope analysis in the Transmission Electron Microscope
7.-11. March 2017 Bad Mitterndorf (Austria)	Nion Swift Workshop III	-	-
12.-14. December 2017 Ulm (Germany)	3rd SALVE Symposium	-	-
5.-10. February 2018 Obergurgl (Austria)	Graphene Winter School	Poster	Revealing the 3D structure of graphene defects
17.-24. March 2018 Kirchberg (Austria)	International Winterschool on Electronic Properties of Novel Materials	Poster	Revealing the 3D structure of graphene defects
9.-13. July 2018 Trieste (Italy)	Conference on Physics of Defects in Solids: Quantum Mechanics Meets Topology	Oral	Revealing the 3D structure of graphene defects
14.-17. October 2018 Hamburg (Germany)	International Workshop on Advanced and In-situ Microscopies of Functional Nanomaterials and Devices	Poster	Revealing the 3D structure of graphene defects
27.-31. May 2019 Nice (France)	Spring Meeting of the European Materials Research Society	Oral	Revealing the 3D structure of graphene defects and electron-beam induced out-of plane dynamics
26. June 2019 Tübingen (Germany)	Netzwerk für Elektronenmikroskopie Tübingen – Symposium	Oral	Revealing the 3D structure of defects in 2D materials
1.-5. September 2019 Berlin (Germany)	Microscopy Conference	Oral	Revealing the 3D structure of graphene defects and electron-beam induced out-of plane dynamics

Table .1: **List of participated scientific conferences and workshops during the PhD project.**

Bibliography

[1] ScienceWatch. Konstantin Novoselov Interview - Special Topic of Graphene, 2009.

[2] P. R. Wallace. The Band Theory of Graphite. *Physical Review*, 71(9):622–634, may 1947.

[3] J. C. Slonczewski and P. R. Weiss. Band Structure of Graphite. *Physical Review*, 109(2):272–279, jan 1958.

[4] N. D. Mermin. Crystalline Order in Two Dimensions. *Physical Review*, 176(1):250–254, dec 1968.

[5] L.D. Landau. Zur Theorie der Phasenumwandlungen II. *Phys. Z. Sowjetunion*, 11:26–35, 1937.

[6] R. Peierls. Quelques propriétés typiques des corps solides. *Annales de l'institut Henri Poincaré*, 5(3):177–222, 1935.

[7] K. S. Novoselov, A. K. Geim, S. V. Morozov, D. Jiang, Y. Zhang, S. V. Dubonos, I. V. Grigorieva, and A. A. Firsov. Electric Field Effect in Atomically Thin Carbon Films. *Science*, 306(5696):666–669, oct 2004.

[8] The Royal Swedish Academy of Sciences. The 2010 Nobel Prize in Physics. `https://www.nobelprize.org/prizes/physics/2010/press-release/`, 2010.

[9] Jannik C. Meyer, A. K. Geim, M. I. Katsnelson, K. S. Novoselov, T. J. Booth, and S. Roth. The structure of suspended graphene sheets. *Nature*, 446(7131):60–63, mar 2007.

[10] K. S. Novoselov, A. K. Geim, S. V. Morozov, D. Jiang, M. I. Katsnelson, I. V. Grigorieva, S. V. Dubonos, and A. A. Firsov. Two-dimensional gas of massless Dirac fermions in graphene. *Nature*, 438(7065):197–200, nov 2005.

[11] K.I. Bolotin, K.J. Sikes, Z. Jiang, M. Klima, G. Fudenberg, J. Hone, P. Kim, and H.L. Stormer. Ultrahigh electron mobility in suspended graphene. *Solid State Communications*, 146(9-10):351–355, jun 2008.

[12] R. R. Nair, P. Blake, A. N. Grigorenko, K. S. Novoselov, T. J. Booth, T. Stauber, N. M. R. Peres, and A. K. Geim. Fine Structure Constant Defines Visual Transparency of Graphene. *Science*, 320(5881):1308–1308, jun 2008.

[13] Changgu Lee, Xiaoding Wei, Jeffrey W Kysar, and James Hone. Measurement of the elastic properties and intrinsic strength of monolayer graphene. *Science*, 321(5887):385–8, jul 2008.

[14] A. K. Geim and K. S. Novoselov. The rise of graphene. *Nature Materials*, 6(3):183–191, mar 2007.

[15] Frank Schwierz. Graphene transistors. *Nature Nanotechnology*, 5(7):487–496, jul 2010.

[16] Rinaldo Raccichini, Alberto Varzi, Stefano Passerini, and Bruno Scrosati. The role of graphene for electrochemical energy storage. *Nature Materials*, 14(3):271–279, mar 2015.

[17] Zongyou Yin, Jixin Zhu, Qiyuan He, Xiehong Cao, Chaoliang Tan, Hongyu Chen, Qingyu Yan, and Hua Zhang. Graphene-Based Materials for Solar Cell Applications. *Advanced Energy Materials*, 4(1):1300574, jan 2014.

[18] Andreas Mittelberger, Christian Kramberger, and Jannik C. Meyer. Insights into radiation damage from atomic resolution scanning transmission electron microscopy imaging of mono-layer CuPcCl16 films on graphene. *Scientific Reports*, 8(1):4813, dec 2018.

[19] Rasim Mirzayev, Kimmo Mustonen, Mohammad R. A. Monazam, Andreas Mittelberger, Timothy J. Pennycook, Clemens Mangler, Toma Susi, Jani Kotakoski, and Jannik C. Meyer. Buckyball sandwiches. *Science Advances*, 3(6):e1700176, jun 2017.

[20] A. K. Geim and I. V. Grigorieva. Van der Waals heterostructures. *Nature*, 499(7459):419–425, jul 2013.

[21] K S Novoselov, D Jiang, F Schedin, T J Booth, V V Khotkevich, S V Morozov, and A K Geim. Two-dimensional atomic crystals. *Proceedings of the National Academy of Sciences of the United States of America*, 102(30):10451–3, jul 2005.

[22] Rubén Mas-Ballesté, Cristina Gómez-Navarro, Julio Gómez-Herrero, and Félix Zamora. 2D materials: to graphene and beyond. *Nanoscale*, 3(1):20–30, jan 2011.

[23] I. L. Aleiner, D. E. Kharzeev, and A. M. Tsvelik. Spontaneous symmetry breaking in graphene subjected to an in-plane magnetic field. *Physical Review B*, 76(19):195415, nov 2007.

[24] H. W. Kroto, J. R. Heath, S. C. O'Brien, R. F. Curl, and R. E. Smalley. C60: Buckminster-fullerene. *Nature*, 318(6042):162–163, nov 1985.

[25] Sami Malola, Hannu Häkkinen, and Pekka Koskinen. Structural, chemical, and dynamical trends in graphene grain boundaries. *Physical Review B*, 81(16):165447, apr 2010.

[26] Oleg V. Yazyev and Steven G. Louie. Topological defects in graphene: Dislocations and grain boundaries. *Physical Review B - Condensed Matter and Materials Physics*, 81(19):1–7, 2010.

[27] Jamie H. Warner, Ye Fan, Alex W. Robertson, Kuang He, Euijoon Yoon, and Gun Do Lee. Rippling Graphene at the Nanoscale through Dislocation Addition. *Nano Letters*, 13(10):4937–4944, oct 2013.

[28] Florian Banhart, Jani Kotakoski, and Arkady V. Krasheninnikov. Structural Defects in Graphene. *ACS Nano*, 5(1):26–41, jan 2011.

[29] J Kotakoski, A V Krasheninnikov, U Kaiser, and J C Meyer. From Point Defects in Graphene to Two-Dimensional Amorphous Carbon. *Physical Review Letters*, 106(10):105505, 2011.

[30] Jani Kotakoski, Clemens Mangler, and Jannik C. Meyer. Imaging atomic-level random walk of a point defect in graphene. *Nature Communications*, 5:3991, may 2014.

[31] Toma Susi, Demie Kepaptsoglou, Yung-Chang Lin, Quentin M Ramasse, Jannik C Meyer, Kazu Suenaga, and Jani Kotakoski. Towards atomically precise manipulation of 2D nanostructures in the electron microscope. *2D Materials*, 4(4):042004, sep 2017.

[32] Mukesh Tripathi, Andreas Mittelberger, Nicholas A. Pike, Clemens Mangler, Jannik C. Meyer, Matthieu J. Verstraete, Jani Kotakoski, and Toma Susi. Electron-Beam Manipulation of Silicon Dopants in Graphene. *Nano Letters*, 18:5319–5323, jul 2018.

[33] Ondrej Dyck, Songkil Kim, Elisa Jimenez-Izal, Anastassia N Alexandrova, Sergei V Kalinin, and Stephen Jesse. Building Structures Atom-by-Atom via Electron Beam Manipulation. *Small*, 14(38):1801771, 2018.

[34] Quentin M. Ramasse, Che R. Seabourne, Despoina-Maria Kepaptsoglou, Recep Zan, Ursel Bangert, and Andrew J. Scott. Probing the Bonding and Electronic Structure of Single Atom Dopants in Graphene with Electron Energy Loss Spectroscopy. *Nano Letters*, 13(10):4989–4995, oct 2013.

[35] Wu Zhou, Myron D. Kapetanakis, Micah P. Prange, Sokrates T. Pantelides, Stephen J. Pennycook, and Juan-Carlos Idrobo. Direct Determination of the Chemical Bonding of Individual Impurities in Graphene. *Physical Review Letters*, 109(20):206803, nov 2012.

[36] Toma Susi, Trevor P Hardcastle, Hans Hofsäss, Andreas Mittelberger, Timothy J Pennycook, Clemens Mangler, Rik Drummond-Brydson, Andrew J Scott, Jannik C Meyer, and Jani Kotakoski. Single-atom spectroscopy of phosphorus dopants implanted into graphene. *2D Materials*, 4(2):021013, feb 2017.

[37] Mukesh Tripathi, Alexander Markevich, Roman Böttger, Stefan Facsko, Elena Besley, Jani Kotakoski, and Toma Susi. Implanting Germanium into Graphene. *ACS Nano*, 12(5):4641–4647, may 2018.

[38] Xuesong Li, Carl W. Magnuson, Archana Venugopal, Jinho An, Ji Won Suk, Boyang Han, Mark Borysiak, Weiwei Cai, Aruna Velamakanni, Yanwu Zhu, Lianfeng Fu, Eric M. Vogel, Edgar Voelkl, Luigi Colombo, and Rodney S. Ruoff. Graphene Films with Large Domain Size by a Two-Step Chemical Vapor Deposition Process. *Nano Letters*, 10(11):4328–4334, nov 2010.

[39] Oleg V. Yazyev and Steven G. Louie. Electronic transport in polycrystalline graphene. *Nature Materials*, 9(10):806–809, oct 2010.

[40] Jie Xu, Guowen Yuan, Qi Zhu, Jiangwei Wang, Shan Tang, and Libo Gao. Enhancing the Strength of Graphene by a Denser Grain Boundary. *ACS Nano*, 12(5):4529–4535, may 2018.

[41] Simon Kurasch, Jani Kotakoski, Ossi Lehtinen, Viera Skákalová, Jurgen Smet, Carl E Krill, Arkady V Krasheninnikov, and Ute Kaiser. Atom-by-Atom Observation of Grain Boundary Migration in Graphene. *Nano Letters*, 12(6):3168–3173, jun 2012.

[42] Jannik C. Meyer, Franz Eder, Simon Kurasch, Viera Skakalova, Jani Kotakoski, Hye Jin Park, Siegmar Roth, Andrey Chuvilin, Sören Eyhusen, Gerd Benner, Arkady V. Krasheninnikov, and Ute Kaiser. Accurate measurement of electron beam induced displacement cross sections for single-layer graphene. *Physical Review Letters*, 108(19):196102, 2012.

[43] Toma Susi, Christoph Hofer, Giacomo Argentero, Gregor T Leuthner, Timothy J Pennycook, Clemens Mangler, Jannik C Meyer, and Jani Kotakoski. Isotope analysis in the transmission electron microscope. *Nature Communications*, 7:13040, 2016.

[44] E. Ruska. Über ein magnetisches Objektiv für das Elektronenmikroskop. *Zeitschrift für Physik*, 89(1-2):90–128, jan 1934.

[45] The Royal Swedish Academy of Sciences. The Nobel Prize in Physics 1986. `https://www.nobelprize.org/prizes/physics/1986/summary/`, 1986.

[46] Manfred von Ardenne. Das Elektronen-Rastermikroskop. *Zeitschrift für Physik*, 109(9-10):553–572, sep 1938.

[47] A. V. Crewe. Scanning Electron Microscopes: Is High Resolution Possible? *Science*, 154(3750):729–738, nov 1966.

[48] A. V. Crewe, J. Wall, and L. M. Welter. A High Resolution Scanning Transmission Electron Microscope. *Journal of Applied Physics*, 39(13):5861–5868, dec 1968.

[49] A V Crewe and J Wall. A scanning microscope with 5 Å resolution. *Journal of Molecular Biology*, 48(3):375–393, 1970.

[50] A V Crewe, J Wall, and J Langmore. Visibility of single atoms. *Science (New York, N.Y.)*, 168(3937):1338–1340, jun 1970.

[51] O Scherzer. Über einige Fehler von Elektronenlinsen. *Zeitschrift für Physik*, 101(9-10):593–603, sep 1936.

[52] P. W. Hawkes. The Geometrical Aberrations of General Electron Optical Systems I. The Conditions Imposed by Symmetry. *Philosophical Transactions of the Royal Society A: Mathematical, Physical and Engineering Sciences*, 257(1086):479–522, jun 1965.

[53] Max Haider, Harald Rose, Stephan Uhlemann, Eugen Schwan, Bernd Kabius, and Knut Urban. A spherical-aberration-corrected 200 kV transmission electron microscope. *Ultramicroscopy*, 75(1):53–60, oct 1998.

[54] O.L. Krivanek, N. Dellby, and A.R. Lupini. Towards sub-Å electron beams. *Ultramicroscopy*, 78(1-4):1–11, jun 1999.

[55] Martin Linck, Peter Hartel, Stephan Uhlemann, Frank Kahl, Heiko Müller, Joachim Zach, Max. Haider, Marcel Niestadt, Maarten Bischoff, Johannes Biskupek, Zhongbo Lee, Tibor Lehnert, Felix Börrnert, Harald Rose, and Ute Kaiser. Chromatic Aberration Correction for Atomic Resolution TEM Imaging from 20 to 80 kV. *Physical Review Letters*, 117(7):076101, aug 2016.

[56] Ondrej L Krivanek, Tracy C Lovejoy, Niklas Dellby, and R W Carpenter. Monochromated STEM with a 30 meV-wide, atom-sized electron probe. *Microscopy*, 62(1):3–21, feb 2013.

[57] Ondrej L Krivanek, Tracy C Lovejoy, Niklas Dellby, Toshihiro Aoki, R W Carpenter, Peter Rez, Emmanuel Soignard, Jiangtao Zhu, Philip E Batson, Maureen J Lagos, Ray F Egerton, and Peter A Crozier. Vibrational spectroscopy in the electron microscope. *Nature*, 514(7521):209–212, 2014.

[58] Ondrej L. Krivanek, Matthew F. Chisholm, Valeria Nicolosi, Timothy J. Pennycook, George J. Corbin, Niklas Dellby, Matthew F. Murfitt, Christopher S. Own, Zoltan S. Szilagyi, Mark P. Oxley, Sokrates T. Pantelides, and Stephen J. Pennycook. Atom-by-atom structural and chemical analysis by annular dark-field electron microscopy. *Nature*, 464(7288):571–574, mar 2010.

[59] Earl J. Kirkland. *Advanced computing in electron microscopy*. Springer US, New York, 2 edition, 2010.

[60] Christoph Koch. *Determination of core structure periodicity and point defect density along dislocations*. PhD thesis, Arizona State University, 2002.

[61] A. C. Ferrari, J. C. Meyer, V. Scardaci, C. Casiraghi, M. Lazzeri, F. Mauri, S. Piscanec, D. Jiang, K. S. Novoselov, S. Roth, and A. K. Geim. Raman Spectrum of Graphene and Graphene Layers. *Physical Review Letters*, 97(18):187401, oct 2006.

[62] Andrea C. Ferrari and Denis M. Basko. Raman spectroscopy as a versatile tool for studying the properties of graphene. *Nature Nanotechnology*, 8(4):235–246, apr 2013.

[63] Yi Zhang, Luyao Zhang, and Chongwu Zhou. Review of Chemical Vapor Deposition of Graphene and Related Applications. *Accounts of Chemical Research*, 46(10):2329–2339, oct 2013.

[64] D. J. De Rosier and A. Klug. Reconstruction of Three Dimensional Structures from Electron Micrographs. *Nature*, 217(5124):130–134, jan 1968.

[65] Peter Ercius, Osama Alaidi, Matthew J. Rames, and Gang Ren. Electron Tomography: A Three-Dimensional Analytic Tool for Hard and Soft Materials Research. *Advanced Materials*, 27(38):5638–5663, oct 2015.

[66] M C Scott, Chien-Chun Chen, Matthew Mecklenburg, Chun Zhu, Rui Xu, Peter Ercius, Ulrich Dahmen, B C Regan, and Jianwei Miao. Electron tomography at 2.4-ångström resolution. *Nature*, 483, 2012.

[67] J. Miao, P. Ercius, and S. J. L. Billinge. Atomic electron tomography: 3D structures without crystals. *Science*, 353(6306):aaf2157, sep 2016.

[68] Dirk Van Dyck, Joerg R Jinschek, and Fu-Rong Chen. 'Big Bang' tomography as a new route to atomic-resolution electron tomography. *Nature*, 486(7402):243–246, 2012.

[69] Sandra Van Aert, Kees J. Batenburg, Marta D. Rossell, Rolf Erni, and Gustaaf Van Tendeloo. Three-dimensional atomic imaging of crystalline nanoparticles. *Nature*, 470(7334):374–377, feb 2011.

[70] Liu-Gu Chen, Jamie Warner, Angus I. Kirkland, Fu-Rong Chen, and Dirk Van Dyck. Snapshot 3D Electron Imaging of Structural Dynamics. *Scientific Reports*, 7(1):10839, dec 2017.

[71] Shigeyuki Morishita, Ryosuke Senga, Yung-Chang Lin, Ryuichi Kato, Hidetaka Sawada, and Kazutomo Suenaga. Depth sensitive imaging of graphene with an atomic resolution microscope. *Applied Physics Letters*, 113(23):233101, dec 2018.

[72] O.L. Krivanek, G.J. Corbin, N. Dellby, B.F. Elston, R.J. Keyse, M.F. Murfitt, C.S. Own, Z.S. Szilagyi, and J.W. Woodruff. An electron microscope for the aberration-corrected era. *Ultramicroscopy*, 108(3):179–195, feb 2008.

[73] Caroline A Schneider, Wayne S Rasband, and Kevin W Eliceiri. NIH Image to ImageJ: 25 years of image analysis. *Nature Methods*, 9(7):671–675, jul 2012.

[74] Christoph Hofer, Christian Kramberger, and Jannik C. Meyer. 3D reconstruction of two atomically resolved STEM images. `https://github.com/christophhofer40/3D-reconstruction`, 2019. Github.

Appendix

A Complete workflow for the 3D reconstruction from multiple atomically resolved STEM images

The algorithm presented in chapter 3 has been developed over the last years. There are obviously several parameters which have to be fine tuned in order to obtain reliable results. This appendix chapter is dedicated to a rather technical description of all data processing steps needed for the successful reconstruction. It is intended to be detailed enough so that the reader (assuming he/she has all the necessary software correctly installed) can reproduce the results. The software is a set of ImageJ [73] plugins which can be downloaded from github [74]. It also includes a data set which is used in chapter 3. The computation can be performed by any standard computer.The reconstruction involves the following steps:

1. Data preprocessing

2. Extraction of the 2D models

3. Assignment of the same atoms

4. Fine tuning of the 2D models

5. 3D reconstruction

A.1 Data preprocessing

Before starting the task of reconstruction, the data has to be preprocessed in order to not confuse the algorithm. First, the images have to be high-pass filtered in order to reduce low-frequency variations arising from the electron beam tail. This can be done with the existing ImageJ functions. First, the image stack has to be opened (assuming all images have the same field of view) by ImageJ. A duplicate of the image stack has then to be processed by a Gaussian filter with a relatively high Gaussian radius (ca. 1 nm so that only the low frequency modulations are present; the lattice should disappear). The raw image stack is then mathematically divided by the filtered images (*Process > Image Calculator ...*). Optionally, the resulting image can then be further processed by Gaussian smoothing to reduce pixel-to-pixel variations. In order to reduce the computational time, the pixel size of the image can be reduced. The test images, for example, are down-sampled to $6.4\,\text{pixel}/\text{Å}$ (*Image > Adjust > Size ...*). This results in an image size of 512×512 pixels (using a power of 2 for faster computation times is recommended). Then, the contamination has to be masked out by creating a selection of the "undesired" region manually and setting the pixel values to "NaN" (*Process > Math > Set ...*). Finally, the processed image should be saved in TIFF-format to an arbitrary working directory and is ready for the algorithm.

A.2 Extraction of the 2D models

With the processed images open, the plugin "*Smart_Atomizer.java*" can be started which opens a Graphical User Interface (GUI). Fig. 1 shows the GUI with the default settings. The panel *raw image (GRAY32)* should highlight the name of the experimental image stack. The first step is to set up appropriate atom parameters by checking *interactive atom*, where another GUI opens after clicking *OK*. The new GUI shows several parameters: *radius* is the size of the window which is used for convolution in real space, *FWHM* is the width of the atom and *solid diameter* defines the minimum allowed distance between atoms. All units here are in pixels. After confirming these parameters, several windows are popping up: "*atom.tif*", "*model.tif*" (zero image with non-zero pixel values which correspond to atomic positions), "*sim.tif*" (simulation obtained by a convolution of the model with "*atom.tif*") and "diff.tif" ("sim.tif" minus input image). "model.tif" is the image stack which carries the information about the 2D models and is taken as input for the further processes. The default values in the GUI are adjusted for the test data, meaning that the correct extraction of the 2D models can be generated using these values. It takes approx. 5 iterations of generating and fine tuning atoms (ca. 5 min). This task has to be done for both views (the algorithm only processes the view corresponding to the front slice of the experimental image). The success of the algorithm is easily confirmed visually by comparing the experimental image to the established network using "*show topology overlay*". However, if there are clearly visible model errors after convergence, several parameters can be adjusted depending on the problem: If there are clearly too few atoms, reduce the solid diameter and/or decrease the relative peak weight threshold and vice-versa. If the signal-to-noise ratio is too poor for the correct assignment, there are two tricks in order to fulfill the task. Firstly, one can set or delete atoms manually by modifying the image stack "model.tif", where the algorithm reads the atomic model from. It can help to set up the correct number of atoms to their approximate positions and then use a small value of *solid diameter* and a few iterations of *fine tune atoms*. Secondly, there is the option "*analyze & fix topology*", which corrects the topology using assumptions about the sp^2-configuration of the underlying data. For example, it deletes atoms in the model which have only two neighbors or corrects the presence of two neighboring pentagons. For the completion, all the parameters are explained in listing 1.

118

```
raw image (GRAY32)      name of image stack used as input
full stack              proccesses full stack
cycles                  number of iterations
max threads             maximum number of threads
atom                    name of image used for convolution
solid diameter          minimum distance between two atoms
guessed atom FWHM       FWHM of point spread function
interactive atom        changes atom parameters
enforce solid diameter  deletes all atoms within the solid diameter
model                   name of image stack of the delta lattice
reset model             sets model to zero
homogenize intensities  sets all delta values in model to average value,
                            weighted by the intensity mixing factor
intensity mixing
    factor              weight for equalizing the intensities
fixed intensities       uses only average intensity for the
                            delta intensity
generate atoms          places atoms quasi-randomly
and keep all atoms      forces to keep all atoms
relative peak
    weight threshold    uses only intensities in certain region
grand trials            number of iterations of genearating atoms
analyze and
    fix topology        corrects suspisious configurations
                            in the topology
show topology overlay   shows overlay of bonds, rings and their
                            connections
fine tune atoms         shifts atoms by the amount
                            given by the wobble radius
wobble radius           wobbles atoms within this radius
cycles per atom         iterations per atom during fine tuning
optimize FWHM           matched width of atoms based on the error
    function
auto scale intensities  adjusts atomic intensity
                            based on the error function
simulated               name of image stack of the simulation
deviations              name of image stack of the difference image
init mesh from xyz      initialize the atomic network from a .xyz file
read signature
    from disk           reads the identical atoms from a .sig file
join meshes             correlates the topologies
write signature
    to disk             saves the signature of the topology in
                            a .sig file
write topology to disk  saves the topology (atoms, bonds, rings)
                            in a .top file
```

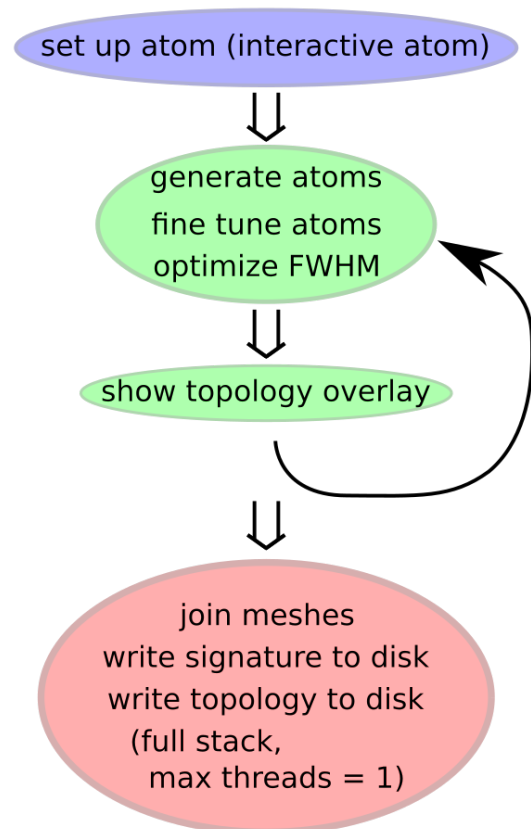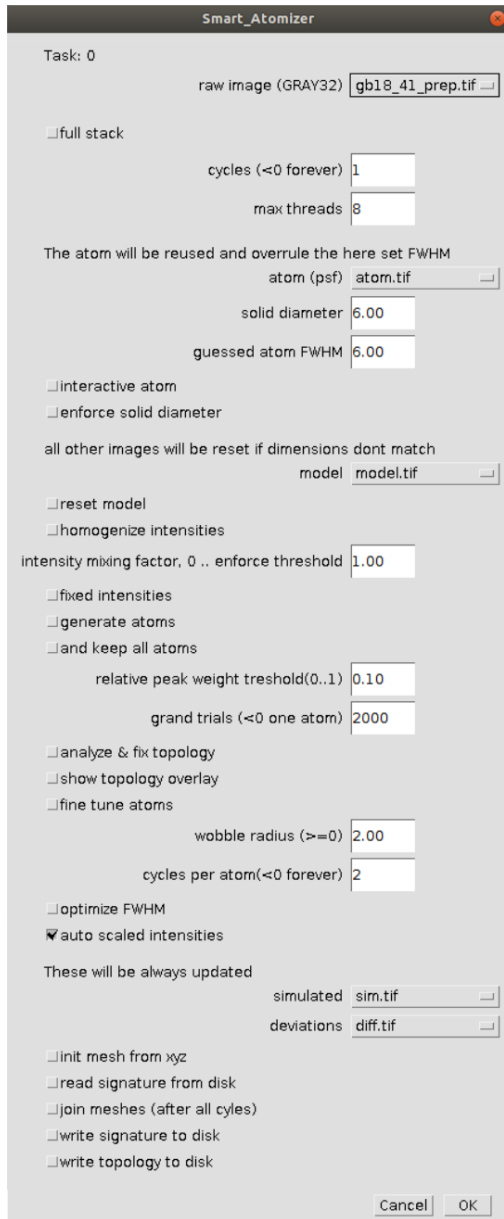Listing 1: Parameters of GUI in Fig. 1.

Figure 1: GUI when loading *Smart_Atomizer.java* (left) and recommended order of tasks (right).

A.3 Assignment of the same atom

When the 2D models of each view are identified correctly, the correct correlation of the models includes three check boxes in the GUI which have to be checked: "*join meshes*", "*write signature to disk*" and "*write topology to disk*". The algorithm assumes the presence of non-hexagonal rings. After clicking *OK*, it asks for confirmation if the chosen starting atoms are identical, which should be the case if the sequence of defects is irregular. For a circular closed GB, for example, the user has to confirm when the algorithm asks if the suggested atoms are identical. The algorithm creates two files in the working directory, having the same name as the initial image but endings with "*.sig*" and "*.top*", respectively. The latter contains the information about the topology, e.g. atoms, bonds and rings. It also initializes the 3D model based on all of the 2D models. Listing 2 shows a small part of the file.

```
MASTER  1237           # shows how many atoms are in the initialized 3D
    model
ATOM    0   2   246.0   260.0   0.0 6        # keyword id    viewcounts
    x   y   z   element
ATOM    1   2   254.0   266.0   0.0 6
.
.
.


VIEW    0   # keyword   viewnumber
#view of slice:1 in NAME.tif

TRANSLATION 0.0 0.0 0.0
# keyword   x-translation   y-translation   z-translation (will be
    calculated)
SKEWMATRIX  1.0 0.0 0.0 1.0
# keyword   matrix elements for distortion (can be matched)
QUATERNION  0.0     0.0
# keyword   inclination angle (use microscopy metadata!)    azimuthal
    angle (can be matched)

ATOM    935 145.0   35.0    # keyword id    x   y
ATOM    858 201.0   35.0
.
.
.
```

Listing 2: Example for the text in *NAME.top*

A.4 Fine tuning of the 2D models

Section A.2 was primarily written to extract the 2D models without the focus on high precision. The next piece of software fine tunes the atomic model based on a more quantitative approach: Here, the "atom" also takes aberrations into account and therefore it is from now on referred to as electron probe. It also allows sub-pixel accuracy for the atomic positions. For this task, the plugin "*TwoDReconstruction.java*" has to be executed, which opens another GUI (Fig. 2). "*Reset model*" has to be used first to initialize the corresponding images. It also initializes the beam using the

parameters (e.g. aberrations, FOV, Gaussian blur) from a file called "*beamparameters.txt*". It takes default parameters if there is no file. The file contains several keywords and the corresponding values separated by tabs. An example for the file is given in the listing 3.

```
VIEW:    0 # number of view
Aberrations:     -0.3998013   -0.01281184 0.16177532   12.400177
    -13.0498085  24.028996    -31.067255
# Aberrations:  C10 C12a     C12b     C21a     C21b     C23a     C23b
Sigma:  1.5427575
# Sigma:     Gaussian radius in pixels
FieldOfView:     8.0
# FieldOfView:  FOV in nm
VIEW:    1
Aberrations:     -1.25065     0.46148407   -0.2955373   21.837414
    -1.5990982   10.735797    1.975914
Sigma:  1.4375322
FieldOfView:     8.0
```

Listing 3: Example for the code in *beamparameters.txt*

It has to be mentioned that this program homogenizes the atomic intensities of the same elements (default value is 6 for carbon). If there are other elements than carbon, the corresponding element number can be set in the top file (using tab as delimiter). The program allows to fine tune the atomic positions (*fine tune*) and adjust the parameters of the electron probe (*match aberrations*, *match Gaussian blur*, *match FOV*). It creates an adjusted duplicate of the topology file, but the original file can be overwritten by using the checkbox "*save topology file*". All the parameters are listed in listing 4.

```
raw image (GRAY32)        name of image stack used as input
reset model               reads the .top file and beamparameters.txt
                              and resets the initialization
init from imagetitle
    "model.tif"           initializes from "model.tif"
fine tune atoms           optimizes atomic positions
number of iterations      number of iterations of fine tuning
match Gaussian blur       matches the radius of the Gaussian blur
match aberrations         matches the aberration coefficients
match fov                 matches the field of view
adjust atomic
    intensities           matches the atomic intensities
mean stepsize             mean of normal-distributed step size
total rounds              number of iterations
slice to optimize         slice which is processed
```

Listing 4: Parameters of GUI in Fig. 2 (left).

A.5 3D reconstruction

The final task is the actual reconstruction. Before starting the program, one has to ensure that the tilt angles are correctly set in the topology file (cf. listing 2). For this task, open the topology file and search for the word "*VIEW*", and adjust the values right of the keyword "*QUATERNION*".
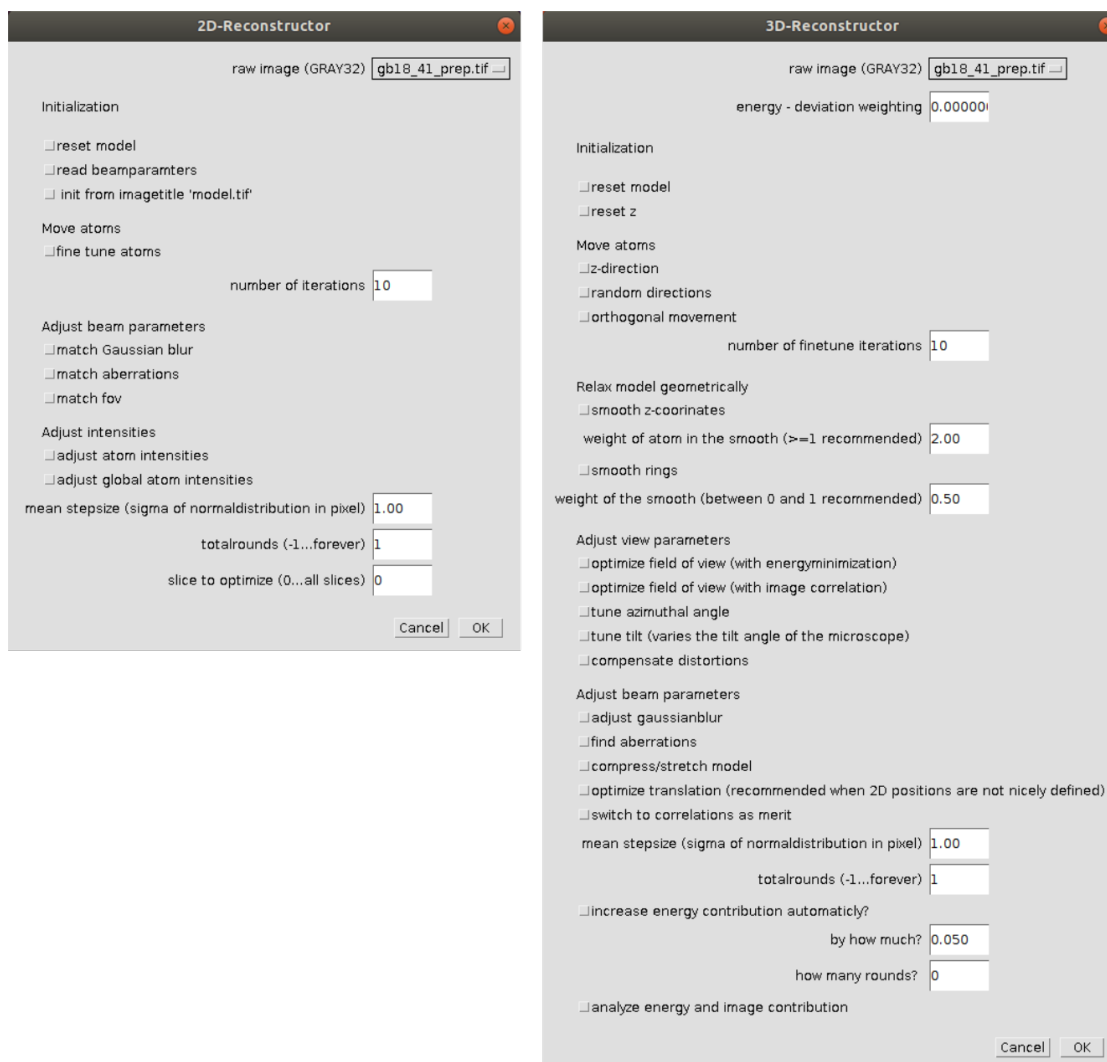
Figure 2: GUI when loading *TwoD-finetune.java* (left) and *Reconstructor.java* (right).

The first value corresponds to the inclination angle and the second value corresponds to the azimuth angle, which can be adjusted as part of the optimization process. Then the plugin "*Reconstructor.java*" can be loaded, which opens a similar GUI as in the previous section. All the parameters are listed in listing 5. "*Reset model*" is again obligatory to initialize the images using the information from the topology file (which has to be again the same name as the image stack). The initialization of the electron probe is again based on the file "*beamparameters.txt*", which basically takes the optimized parameters of the previous step. Therefore, it is usually not necessary to change these parameters in the course of the 3D optimization. Before moving the atoms (in *z-direction* or in *random directions*), it is recommended to adjust the view parameters like azimuth angle ("*adjust azimuth angle*"), the scaling ("*adjust scale*") and eventually adjust distortions "*adjust distortions*"). When moving the atoms (in the beginning *z-direction* is recommended), "*z-smoothing*" and "*ring-smoothing*" before adjusting the view parameters again turns out to provide a reliable reconstruction. The checkbox "*use correlation as merit*" uses the image deviation instead of the projected positions as merit (cf. eq. 3.2) instead of the observed positions in the 2D models (cf. eq. 3.1). The program saves the new model in a duplicated *.top* file and in *.xyz* format.

```
raw image (GRAY32)       name of image stack used as input
reset model              reads the .top file and beamparameters.txt
                             and resets the initialization
reset z                  sets z to zero for all atoms in the 3D model
z-direction              optimizes atomic positions shifting the atoms
                             parallel to the viewing direction
random directions        optimizes atomic positions using
                             random directions
orthogonal movement      optimizes atomic positions shifting the atoms
                             orthoogonal to the viewing direction
smooth z-coordinates     smoothes the z-coordinates of each atom
                             based on the neighbors
smooth rings             smoothes the structure based on the rings
match fov                matches the field of view based on
                             the energy of the model or the image
                                 correlation
tune azimuthal angle     matches the azimuthal angle
tune inclination angle   matches the inclination angle
compensate distortions   matches the skewmatrix
match Gaussian blur      matches the radius of the Gaussian blur
match aberrations        matches the aberration coefficients
scale model              matches the scale of the models in each view
optimize translation     optimizes translation coefficients
switch to correlation
    as merit             uses image correlation for optimization
mean stepsize            mean of normal-distributed step size
total rounds             number of iterations
increase energy
    contribution aut.    increases the energy contribution
                             after a certain amount of iterations
analyze energy and
    image contribution   shifts a certain atom and tracks
                             the change in energy and image error
```

Listing 5: Parameters of GUI in Fig. 2 (right).